FORSCHUNGSZENTRUM JÜLICH GmbH

Institut für Festkörperforschung

Flow in Czochralski Crystal Growth Melts

M. Mihelcic H. Wenzl K. Wingerath

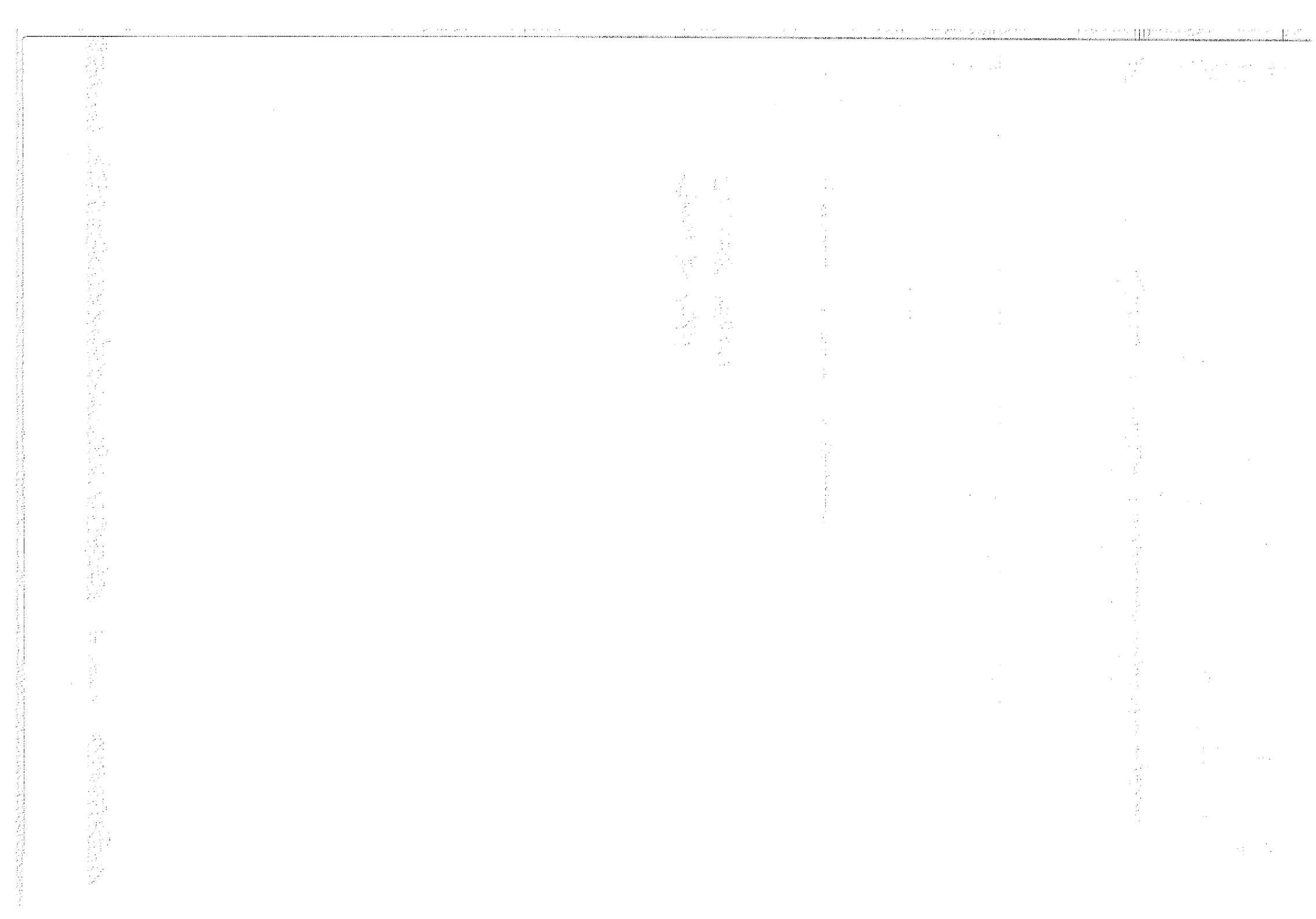

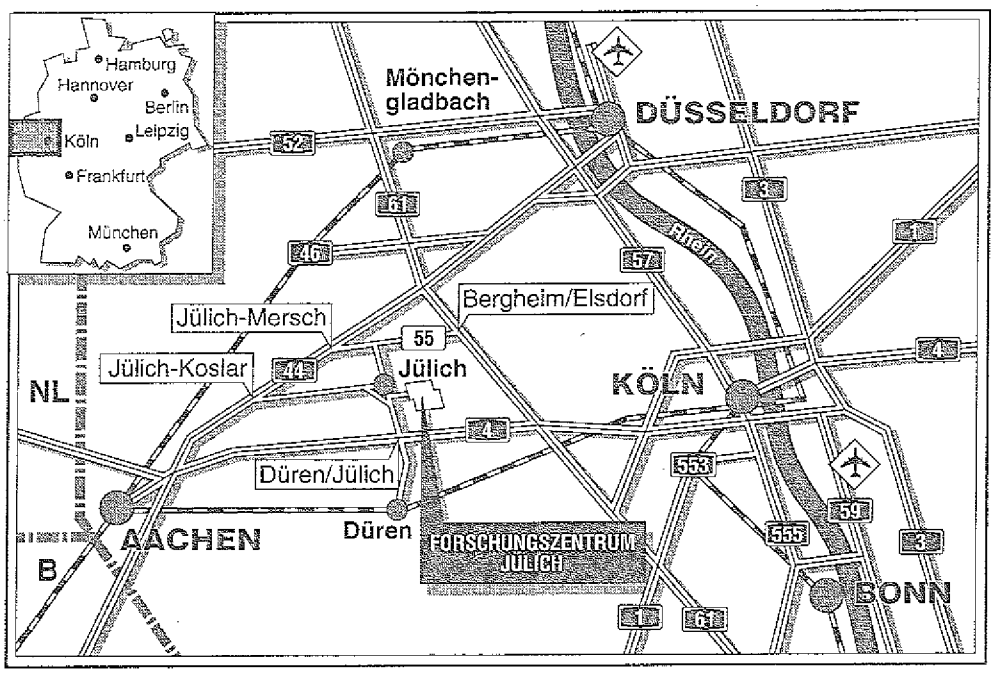

Berichte des Forschungszentrums Jülich ; 2697
ISSN 0366-0885
Institut für Festkörperforschung Jül-2697

Zu beziehen durch: Forschungszentrum Jülich GmbH · Zentralbibliothek
Postfach 1913 · D-5170 Jülich · Bundesrepublik Deutschland
Telefon: 02461/61-6102 · Telefax: 02461/61-6103 · Telex: 833556-70 kfa d

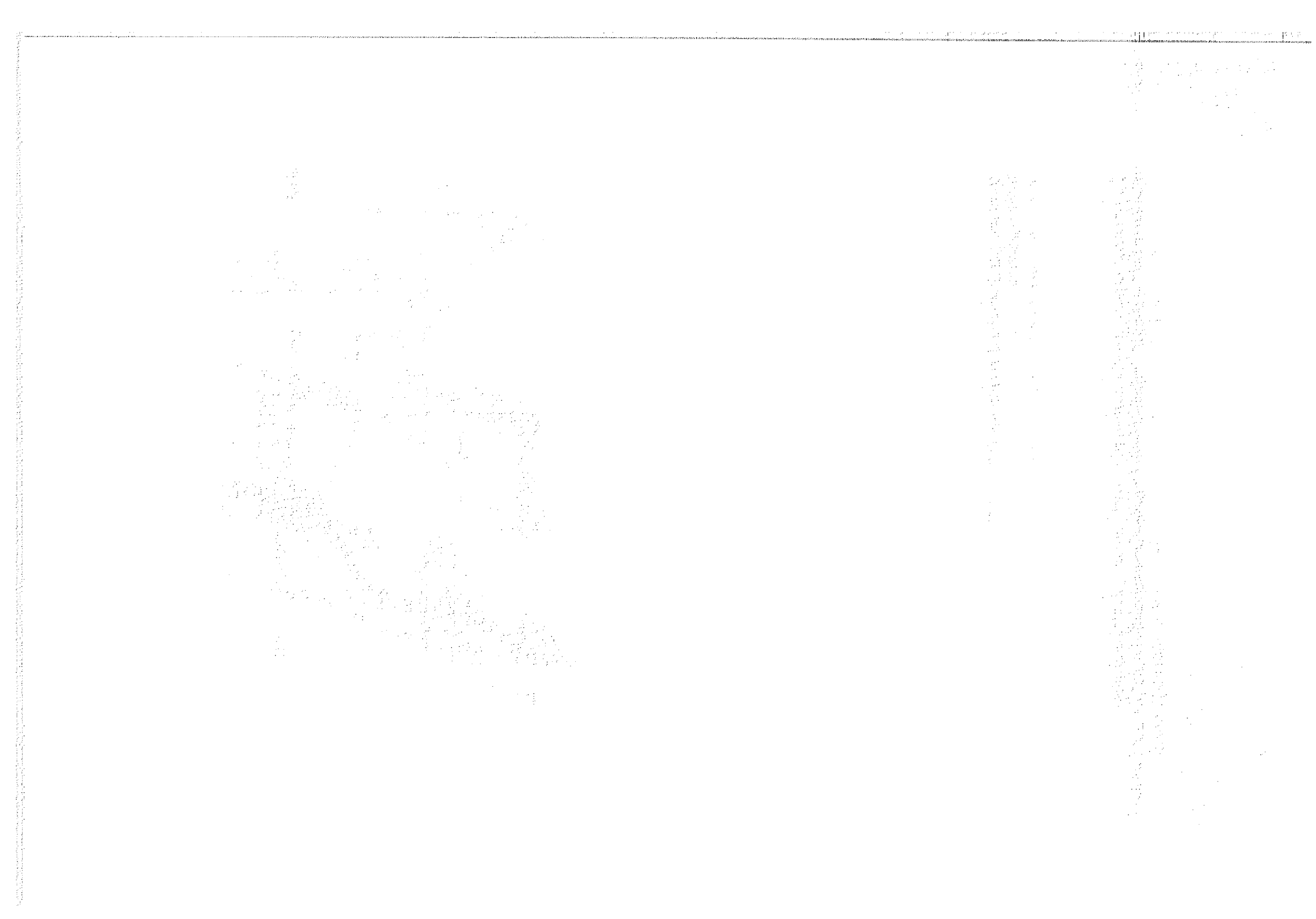

Flow in Czochralski Crystal Growth Melts

M. Mihelcic H. Wenzl K. Wingerath

Content

0.Abstract

It is a well-known fact that in the Czochralski crystal growth ,as well as in all other crystal growth processes from the liquid phase,the flow in the melt has a strong influence on the chemical and physical properties of the growing crystal.

Unlike some other techniques the Czochralski crystal growth technique,with the view to its dynamics,represents a rotating system,which is rich in many flow phenomena not existing in non-rotating systems.For this reason,some notion of the theory of rotating fluids will be necessary for better understanding of fluid dynamics in the Czochralski crystal growth.

This report consists of two parts.In the first part, elements of the theory of rotating fluids are given.It covers,among others,such topics as Taylor-Proudman theorem and its consequences on the fluid flow;Ekman boundary layer;forced oscillations in a rotating fluid which might influence the crystal growth in those cases in which both,the crystal and the crucible,are rotated and the solid-liquid interface is inclined to the rotation axis.

In particular, the stability of the flow is of great importance.Many observations during the crystal growth have shown that flow transitions,as the consequence of the flow instability, produce a change of the shape or diameter of the solid-liquid interface.

In the second part numerical simulations are presented. We start with the definition of the mathematical model and boundary conditions and present our numerical method.

At this point,the problem of choosing the proper model of Cz-crystal growth must be stressed.Even relatively simple questions such as,what kind of flow and temperature fields do really exist in the bulk,can be properly answered only in a three-dimensional mathematical model.

Strong experimental evidence indicates that the flow and temperature field in a real Cz-crystal growth are **asymmetric and transient(oscillating)**and even independent of the scale of experimental set-up. This is not surprising if one recalls for instance,the order of magnitude of Grashof number,Reynolds number etc.,as well as the material constants of metallic melts in a real crystal growth.

An axisymmetrical model can be used,for instance, when the flow and temperature field in boundary layers(e.g.Ekman boundary layers) are concerned,though the influence of asymmetry in the bulk on the boundary layer remains unsettled.

Numerical simulations are performed for (a) axisymmetrical-and (b) three-dimensional

models.In the axisymmetrical model, Cochran flow and forced oscillations in a rotating fluid are simulated on a fine mesh.In the Cochran flow simulation, the difference between the analytical (infinite disk) and numerical (Czochralski geometry) solution are pointed out. Moreover,the simulations of forced oscillations show an excellent agreement with experimental results.

In the three-dimensional model, baroclinic instability, instability of the buoyancy driven convection,and the influence of external magnetic fields on the flow are simulated.

The buoyancy driven convection is of particular importance,since it is highly unstable for all nearly real growth conditions.It was found out that the critical Grashof number is approximately 10^6,which is four orders of magnitude smaller than that for a large(industrial) Czochralski set-up.

Simulations of external magnetic fields show the influence of a stationary transverse- and a vertical magnetic field on the flow and temperature distribution in the model.We first force the flow and temperature field to be asymmetric due to an asymmetric temperature boundary condition at the crucible wall and then study the influence of applied magnetic fields.It is found that the vertical magnetic field decreases the thermal asymmetry much better than the transverse magnetic field.

Some preliminary results of the influence of rotating transverse magnetic field are also given.

I. ELEMENTS OF THE THEORY OF ROTATING FLUIDS.

1.Introduction.

In all crystal growth processes from the liquid phase, convection of the melt strongly influences the chemical and physical properties of the growing crystal.In the Czochralski crystal pulling process /1/ as well as in the solution growth process with accelerated crucible rotation (ACRT) /2,3,4/ there exist two different kinds of convection: thermal convection driven by density variations which are induced by inhomogeneous temperature or concentration distributions,and forced convection due to crystal and crucible rotation.To a certain extent there is also an influence of the thermocapillary convection due to a nonuniform surface tension distribution at the free–surface.Also a superimposed magnetic field (vertical or transverse) will strongly influence the flow pattern.In spite of the complexity of such a system,a discussion of some basic phenomena of rotating fluids will be sufficient to understand the main types of fluid motion in the system.

The theory of rotating fluids deals with a large number of fluid phenomena.It extends from numerous small–scale flows which one can perform in the laboratory to the large–scale circulations in the atmosphere and oceans.In spite of this variety of motions,there is,however,the basic structure in common,which is the object we deal with in the next sections.

2.Equations of Motion of an Incompressible Boussinesq Fluid.

In this section we consider the behavior of an incompressible Boussinesq fluid in the given laboratory system.The concept of "incompressibility"means that the flow velocity $|\vec{u}|$ in the system is small in comparison with the speed of sound in the fluid,i.e.the Mach number $U/a << 1$,where a is the speed of sound in the fluid and U is the characteristic flow velocity.The Boussinesq approximation for a given fluid is valid if the substantial or total derivative term $|D\vec{u}/Dt|$ is small in comparison with the gravity $|\vec{g}|$ and if the density variation ϱ_1 is small in comparison with the mean density $\bar{\varrho}$ in $\varrho = \bar{\varrho} + \varrho_1$. Therefore,the density variation ϱ_1 will be retained only in the buoyancy term $\vec{g} \cdot \varrho_1/\bar{\varrho}$. Besides,it is also convenient to describe the motion of the fluid with reference to an appropriate rotating coordinate system at least in cases in which theoretical considerations are important.

From the point of view of an observer fixed in the coordinate system rotating with angular velocity $\vec{\Omega}$ relative to an inertial frame,the equations of **continuity** and **momentum** of

a fluid with uniform kinematic viscosity ν are /5/

$$\nabla \cdot \vec{u} = 0, \tag{1}$$

$$\partial \vec{u}/\partial t + (2\vec{\Omega} + \vec{\zeta}) \times \vec{u} = -\nabla(P + \frac{1}{2}\vec{u} \cdot \vec{u}) + \vec{g}^* \varrho_1/\bar{\varrho} + \nu \nabla^2 \vec{u}. \tag{2}$$

In these equations $\vec{u}$ is the **Eulerian** flow velocity vector **relative** to the rotating system, $\vec{\zeta} = \nabla \times \vec{u}$ is the corresponding **vorticity** vector, $-2\vec{\Omega} \times \vec{u}$ the **Coriolis** force,t denotes time,$\vec{g}^*$ is the combined effect of **gravitational** and **centrifugal** acceleration, and $P = p/\bar{\varrho} + gz - \frac{1}{2}(\vec{\Omega} \times \vec{r}) \cdot (\vec{\Omega} \times \vec{r})$ is the **normalized or reduced** pressure.In the case of no internal mass sources the density variation ϱ_1 satisfies the following equation

$$\partial \varrho_1/\partial t + (\vec{u} \cdot \nabla)\varrho_1 = \sigma \nabla^2 \varrho_1, \tag{3}$$

where σ denotes the **diffusion** coefficient.If $\sigma << 1$ then (3) becomes $D\varrho_1/Dt = 0$, where $D/Dt = \partial/\partial t + (\vec{u} \cdot \nabla)$ is the substantial derivative.This means that the density variation ϱ_1 is a conservative quantity following the motion of a fluid volume element.Such conservative variables play an important role,for instance,in dynamic meteorology.

By scalar multiplication of eq.(2) with the velocity vector $\vec{u}$ we get

$$\frac{\partial}{\partial t}(\frac{1}{2}\vec{u} \cdot \vec{u}) = -\nu \vec{\zeta} \cdot \vec{\zeta} + \vec{u} \cdot \vec{g}^* \varrho_1/\bar{\varrho} - \nabla \cdot [\frac{1}{2}\vec{u}(\vec{u} \cdot \vec{u}) + \vec{u}P + \nu(\vec{\zeta} \times \vec{u})], \tag{4}$$

where the second term on the left hand side of eq.(2) is omitted in eq.(4) because it represents a force acting at the right angle to the velocity $\vec{u}$, and consequently it does not perform any work. The integral of l.h.s. of eq.(4) over a given control volume represents the **rate of change of total kinetic energy**. The term $-\nu\vec{\zeta} \cdot \vec{\zeta}$ which is negative represents viscous dissipation and the term $\vec{u} \cdot \vec{g}^* \varrho_1/\bar{\varrho}$ is the rate at which the buoyancy force converts the potential energy of gravity ,acting on the density field,into kinetic energy.In the case of thermally-driven flow the latter term is essentially positive when integrated over the whole system (see Hide/5/).The divergence term in eq.(4) represents the mechanical contribution to the kinetic energy.In the case of mechanically- driven flows this term must be positive when integrated over the whole system /5/.

If we take curl of eq.(2) we get the **vorticity** equation

$$\partial \vec{\zeta}/\partial t + (\vec{u} \cdot \nabla)\vec{\zeta} - [(2\vec{\Omega} + \vec{\zeta}) \cdot \nabla]\vec{u} = -\vec{g}^* \times \nabla(\varrho_1/\bar{\varrho}) + \nu \nabla^2 \vec{\zeta}. \tag{5}$$

We see from this equation that the solution $\vec{u} = 0$ of this equation which represents the state of rigid rotation (or hydrostatic equilibrium) is possible only if $\vec{g}^* \times \nabla(\varrho_1/\bar{\varrho}) = 0$,that

is if there is no density variation ϱ_1 on the horizontal surfaces.This condition is **generally not fulfilled** in the Czochralski system since there exist strong horizontal temperature gradients at the crucible wall.The above condition for hydrostatic equilibrium is referred to as **Jeffreys'theorem.**

If for some region in the flow the relative acceleration term $\partial\vec{u}/\partial t + \vec{\zeta} \times \vec{u} + \nabla(\frac{1}{2}\vec{u} \cdot \vec{u})$ in eq.(2) as well as the viscous term $\nu\nabla^2\vec{u}$ are small in comparison with the Coriolis term $2\vec{\Omega} \times \vec{u}$,eq.(2) reduces to

$$2\vec{\Omega} \times \vec{u} = -\nabla P + \vec{g}^* \varrho_1/\bar{\varrho}. \tag{6}$$

Equation (6) desribes the so–called **geostrophic** flow regime. In spite of the extraordinary attractiveness of the geostrophic approximation in describing various properties which the slow, steady flow in a rapidly rotating fluid must possess almost everywhere,we have to realise the fact that this equation is mathematically degenerated.It is of lower order than the momentum equation (2) and,consequently,cannot supply solutions under admissible initial– and boundary conditions.Thus,one has to expect highly non–geostrophic flow regimes occuring not only at the boundaries of the system but also locally in the main body of the flow.We discuss the geostrophic flow in section 3.1.

3.Homogeneous Fluids.

We consider in this section a rotating viscous incompressible fluid whose density ϱ and viscosity μ are constant and uniformly distributed. In addition to the geostrophic state of the flow and its consequences we are especially interested in the coupling between the regions in which the geostrophic flow is dominant,and the viscous boundary layers on the bounding surfaces in the system,within which the tangential velocity is adjusted to its proper wall value by viscosity.However,the viscous layers are not exclusively attached to the bounding surfaces ,but may occur in the interior regions of the flow to smooth away any effect that tends to produce sharp or discontinuous velocity profiles.The structure of such boundary layers depends on the balance of forces which are dominant in the layer.In rotating fluid problems boundary layers of various thicknesses $\sim E^{1/2}$, $\sim E^{1/3}$,$\sim E^{1/4}$,where E is the **Ekman** number ,were found /6,7/.

3.1 Ekman and Rossby Numbers.Geostrophic Flow.

For an incompressible viscous fluid with constant material properties ($\varrho_1 = 0$,$\mu = const.$)

equations (1) and (2) can be read

$$\nabla \cdot \vec{u} = 0, \tag{7}$$

$$\partial \vec{u}/\partial t + (\vec{u} \cdot \nabla)\vec{u} + 2\vec{\Omega} \times \vec{u} = -\nabla P + \nu \nabla^2 \vec{u}, \tag{8}$$

where P is now $P = p/\varrho + gz - \frac{1}{2}(\vec{\Omega} \times \vec{r}) \cdot (\vec{\Omega} \times \vec{r})/5/$. Introducing the reduced pressure P we eliminate the centrifugal– and gravitational force from eq.(8).This is allowed since the centrifugal (gravitational) force is balanced by the radial (vertical) pressure gradient which is always present independently of the existeance of any flow relative to the rotating frame.However,there are limitations to the above simplifications namely that,(a) when the pressure appears explicitly in the boundary condition (e.g. in the case that free–surface or moving boundaries are present),and (b) when the density ϱ is not constant and consequently cannot be taken inside the nabla operator.In the latter case,the variations of the centrifugal– and/or the gravitational force due to variations of the density can change or drive the flow,/8/.

In order to get a dimensionless form of eqs.(7),(8) let L,Ω^{-1}, and U be the typical length,time,and relative velocity of a particular flow.Then we put $\vec{r} = L\vec{r}^*, t = \Omega^{-1}t^*, \vec{u} = U\vec{u}^*, \vec{\Omega} = \Omega\vec{k}, P = \Omega U L P^*$ and get from eqs.(7),(8) (dropping the superscript *)

$$\nabla \cdot \vec{u} = 0, \tag{9}$$

$$\partial \vec{u}/\partial t + Ro(\vec{u} \cdot \nabla)\vec{u} + 2\vec{k} \times \vec{u} = -\nabla P + E\nabla^2 \vec{u}, \tag{10}$$

where $\vec{k}$ denotes the unit vector in the $\vec{\Omega}$– direction.In eq.(10) two important dimensionless parameters appear namely,the **Ekman number**

$$E = \nu/\Omega L^2, \tag{11}$$

and the **Rossby number**

$$Ro = U/\Omega L. \tag{12}$$

Expressions (11),(12) can be transformed in

$$E = \frac{\nu U/L^2}{\Omega U} \sim \frac{viscous\ force}{Coriolis\ force}, \tag{11a}$$

and

$$Ro = \frac{U^2/L}{\Omega U} \sim \frac{inertia\ force}{Coriolis\ force}. \tag{12a}$$

Thus,the Ekman number measures the viscous force against the Coriolis force whereas the Rossby number provides an estimate of the **advective**(i.e.**convective**) acceleration $((\vec{u} \cdot \nabla)\vec{u})$ in comparison with the Coriolis force.The Ekman number is small in most practical cases e.g. $2 \cdot 10^{-5}$ for a crucible radius $R_c = 10cm$,a crucible rotation rate $\Omega_c = 15rpm$ and a kinematical viscosity $\nu = 0.003cm^2/s$ (typical for molten metals).For these melts the assumption $E << 1$ is valid.On the contrary the Rossby number is of the order 1 or less.

If we assume a steady flow with $E << 1$ and $Ro << 1$,then eqs.(9),(10) reduce to

$$\nabla \cdot \vec{u} = 0, \tag{13}$$

$$2\vec{k} \times \vec{u} = -\nabla P. \tag{14}$$

These two equations describe the geostrophic flow in the given system.Since the viscous term is not present in(14),the **no–slip** boundary condition cannot be satisfied in such systems.In the no–slip boundary condition the velocity vector is set $\vec{u} = 0$ at the solid boundaries.Thus,we must replace this condition by the **inviscid** boundary condition which only demands that the fluid cannot penetrate the rigid boundary, i.e. $\vec{u} \cdot \vec{n} = 0$,where $\vec{n}$ is the normal vector to the boundary.

In the real case however,we must expect the existence of thin boundary layers on the solid surfaces at which the large viscous forces$(E\nabla^2\vec{u})$ enable the flow in fulfilling the no–slip condition on these surfaces.

In spite of this remark the geostrophic flow is important .A striking property follows immediately from eq.(14).Since the Coriolis force is always perpendicular to the flow direction the pressure gradient must also be perpendicular to the same direction.This means that the pressure is constant along a streamline in contrast to the flow in a non–rotating system where the pressure variations occur along a streamline(e.g.Bernoulli equation).This result is of great convenience in the cases where the geostrophic approximation is valid(e.g. **weather maps**).

3.2 Taylor–Proudman Theorem.

If we apply the curl operator to eq.(14)we get

$$(\vec{k} \cdot \nabla)\vec{u} = 0. \tag{15}$$

The direct consequence of this result is

$$\partial\vec{u}/\partial\vec{z} = 0 \ or \ \vec{u} = \vec{u}(x,y), \tag{16}$$

which means that the geostrophic flow is independent of the coordinate parallel to the rotation axis.This is the famous **Taylor–Proudman** theorem.This theorem and its consequences illustrate that rotating fluids possess some characteristic properties not found in non–rotating fluids.One of these is the formation of the **Taylor column**.Given a cylindrical container and a small solid object which is fixed to the bottom of the filled container.Besides,let the entire system be in the state of the solid–body roation.If we now change slightly the rotation rate of the container there will be a fluid flow relative to the obstacle.The fluid is deflected at the obstacle but since the flow must be two–dimensional according to eq.(16),the same flow pattern will be repeated at all horizontal levels (if $\vec{k}$ is assumed vertical upward).In this way a vertical column of fluid is formed parallel to the rotation axis with the property that it deflects the flow as if it were of solid material/6,8/.This is the transverse Taylor column.The same transverse column exists in Czochralski system if the angular velocities of the crystal and crucible are different,(Fig.1).

Another type of column is the longitudinal Taylor–column,which is formed when an obstacle(e.g. a sphere) moves along parallel to the rotation axis.For more details see **Greenspan /6/** and **Tritton /8/**.

Also a consequence of the Taylor–Proudman theorem is the flow over "topography".Given the flow confined to the domain $t_1(x,y) \leq z \leq t_2(x,y)$.Eq.(16) implies

$$\vec{u} \equiv (u(x,y), v(x,y), w(x,y)). \tag{17}$$

This together with the inviscid boundary condition $\vec{u}\cdot\vec{n} = 0$ gives

$$(\vec{i}u + \vec{j}v + \vec{k}w)\cdot(\vec{i}\frac{\partial t_1}{\partial x} + \vec{j}\frac{\partial t_1}{\partial y} - \vec{k}) = 0 \ for \ z = t_1, \tag{18}$$

$$(\vec{i}u + \vec{j}v + \vec{k}w)\cdot(\vec{i}\frac{\partial t_2}{\partial x} + \vec{j}\frac{\partial t_2}{\partial y} - \vec{k}) = 0 \ for \ z = t_2. \tag{19}$$

Because of eq.(17) the velocity vector $\vec{u}$ has the same value on both boundaries t_1,t_2.If we now perform the scalar multiplication in eqs.(18),(19) and subtract eq.(18) from eq.(19) we get

$$u(x,y)\frac{\partial(t_2 - t_1)}{\partial x} + v(x,y)\frac{\partial(t_2 - t_1)}{\partial y} = 0, \tag{20}$$

which has the solution (for u,v arbitrary)

$$t_2(x,y) - t_1(x,y) = const. \tag{21}$$

Eq.(21) implies that the flow must be parallel to lines of constant depth.It is also clear that if there are vertical boundaries which cut the height contours then no geostrophic flow is possible,/18/.A Czochralski crucible with curved bottom is probably more restrictive referring to the geostrophic flow regime than a crucible with a flat bottom.

Even if the geostrophic approximation is not a good approximation of the flow,the tendency to fulfill the Taylor–Proudman theorem is present in the motion of a rotating fluid.As an example,we consider the effect of rotation on the convection cell in a horizontal fluid layer heated from below.If the layer is rotating around a vertical axis, a larger temperature difference across it is needed to initiate cellular convection than in the non–rotating case,essentially because of the strong tendency of the flow to two–dimensionality as the consequence of the Taylor–Proudman theorem.When convection is established,the velocity vectors are nearly horizontal,and the fluid is rising and descending along helical streamlines with a small angle between the unit tangent vector and the horizontal plane, instead of performing a meridional motion as in the non–rotating case.The tendency for the small vertical component of the velocity vector to remain constant with height leads to the creation of **narrow but long convective cells** contrary to approximately **square cells** in the non–rotating case/9/.

3.3 Failure of the Geostrophic Flow.Ekman Boundary Layer.

As shown in sec.3.1 the geostrophic approximation demands the vanishing of the viscous term,the non–linear advective term,and the local acceleration term in comparison with the Coriolis term in eq.(10).We now study some examples of the flow in a rotating fluid in which these terms are not negligible but are of the same order as the Coriolis term,at least in the region of interest.

Ekman boundary layers connect the interior region of the flow,where the geostrophic regime is dominant,to horizontal boundaries where conditions like a horizontal stress,or no–slip boundary condition are prescribed.

Following **Moore /7/** we assume that there is a geostrophic flow

$$\vec{u} \equiv (u(x,y), v(x,y), w(x,y)), \tag{22}$$

above a rigid horizontal plane at $z = 0$.Clearly,the geostrophic solution does not satisfy the no-slip condition on the plane $z = 0$.If the plane $z = 0$ is fixed to the rotating frame then this condition reads

$$u = v = w = 0 \qquad on \qquad z = 0. \tag{23}$$

In this case we must retain the viscous term in eq.(10) so that we now get

$$2\vec{k} \times \vec{u} = -\nabla P + E\nabla^2 \vec{u}, \tag{24}$$

or in component form

$$-2v = -\frac{\partial P}{\partial x} + E\nabla^2 u, \tag{25}$$

$$2u = -\frac{\partial P}{\partial y} + E\nabla^2 v, \tag{26}$$

$$0 = -\frac{\partial P}{\partial z} + E\nabla^2 w. \tag{27}$$

The continuity equation $\nabla \cdot \vec{u} = 0$ gives

$$\frac{\partial u}{\partial x} + \frac{\partial v}{\partial y} + \frac{\partial w}{\partial z} = 0. \tag{28}$$

We choose the scaling so that $u, v, \partial/\partial x$ and $\partial/\partial y$ are all of order 1.It follows from eqs.(25) ,(26) that the pressure P is also of order 1. Because the Ekman number E is generally small,the derivative $\partial^2/\partial x^2$ must be large in order to guarantee the same order of the terms $E\nabla^2 u$ and $E\nabla^2 v$ with the Coriolis– and pressure gradient terms in eqs.(25),(26).Let the vertical length scale be δ ,then $\partial/\partial z \sim 1/\delta$ and from the balance of terms in eqs.(25),(26) we get $E/\delta^2 \sim 1$ or,

$$\delta \sim E^{1/2}, \tag{29}$$

which means that the viscous effects are confined to a thin region of thickness $E^{1/2}$.

From the equation of continuity for $\partial u/\partial x \sim 1, \partial v/\partial y \sim 1$ and $\partial/\partial z \sim \delta^{-1}$ we get $w \sim \delta$ and the viscous term in eq.(27) is $E\cdot(\partial^2 w/\partial z^2) \sim E\cdot(\delta/\delta^2) = E^{1/2}$. The integral of eq.(27) across the boundary layer gives for the pressure difference $\delta P = P_\delta - P_0 \sim E$.Therefore, we can introduce the geostrophic pressure $P_g(x, y)$ into eqs. (25),(26) and get

$$-2v = -\partial P_g/\partial x + E\partial^2 u/\partial z^2, \tag{30}$$

$$2u = -\partial P_g/\partial y + E\partial^2 v/\partial z^2, \tag{31}$$

and

$$\frac{\partial u}{\partial x} + \frac{\partial v}{\partial y} + \frac{\partial w}{\partial z} = 0. \tag{32}$$

Since P_g is the geostrophic pressure,the following equations are valid:

$$-2v_g = -\partial P_g/\partial x, \tag{33}$$

$$2u_g = -\partial P_g/\partial y. \tag{34}$$

After introducing relations (33),(34) into (30),(31) we get

$$-2(v - v_g) = E\partial^2 u/\partial z^2, \tag{35}$$

$$2(u - u_g) = E\partial^2 v/\partial z^2. \tag{36}$$

The appropriate boundary conditions are

$$u \rightarrow u_g \qquad and \qquad v \rightarrow v_g, \qquad as \qquad z/\delta \rightarrow \infty, \tag{37}$$

and

$$u = 0 \qquad and \qquad v = 0, \qquad on \qquad z = 0, \tag{38}$$

The solution of the equations (35),(36) together with the boundary conditions (37),(38) is

$$u = -v_g e^{-\lambda z} \sin \lambda z + u_g(1 - e^{-\lambda z} \cos \lambda z), \tag{39}$$

$$v = u_g e^{-\lambda z} \sin \lambda z + v_g(1 - e^{-\lambda z} \cos \lambda z), \tag{40}$$

where $\lambda = 1/\sqrt{E}$.Eqs.(39),(40) give the velocity distribution in the Ekman boundary layer.The thickness of this layer is $\delta \sim E^{1/2}$ which for $L = 1$ in (11) gives $\delta \sim (\nu/\Omega)^{1/2}$.

The next important point we are interested in is the influence of the Ekman layer on the geostrophic flow above it.We have to calculate the velocity component w by means of the continuity equation and relations (39),(40).It follows from eqs.(32),(39),and (40)

$$-\partial w/\partial z = (\partial u_g/\partial x + \partial v_g/\partial y)(1 - e^{-\lambda z} \cos \lambda z) - (\partial v_g/\partial x - \partial u_g/\partial y)e^{-\lambda z} \sin \lambda z. \tag{41}$$

The continuity equation in the geostrophic region is

$$(\partial u_g/\partial x + \partial v_g/\partial y) = 0. \tag{42}$$

The relations (41),(42) together with the boundary condition $w = 0$ at $z = 0$ give

$$w(x, y, z) = (\frac{\partial v_g}{\partial x} - \frac{\partial u_g}{\partial y}) \int_0^z e^{-\lambda \tilde{z}} \sin \lambda \tilde{z} d\tilde{z}. \tag{43}$$

The solution of this integral for $z \to \infty$ gives

$$w(x, y, z) = \frac{1}{2\lambda}(\frac{\partial v_g}{\partial x} - \frac{\partial u_g}{\partial y}) = \frac{1}{2}\sqrt{E}(\frac{\partial v_g}{\partial x} - \frac{\partial u_g}{\partial y}). \tag{44}$$

Since $(\partial v_g/\partial x - \partial u_g/\partial y) = \vec{k} \cdot (\nabla \times \vec{u}_g)$ we get from eq.(44)

$$w_g = \frac{1}{2}\sqrt{E}\zeta_g, \tag{45}$$

where ζ_g is the vertical component of the vorticity vector in the geostrophic flow.This so called "**Ekman condition**" clearly shows the influence of the Ekman boundary layer on the geostrophic flow region in touch with it.Moreover, if the boundary plate at $z = 0$ has velocity (u_p, v_p, w_p) then relation (45) becomes

$$w_g = w_p + \frac{1}{2}\sqrt{E}(\zeta_g - \zeta_p), \tag{46}$$

where ζ_p is independent of the position on the plate/7/.

We give also the solution for the Ekman boundary layer in which a horizontal plate at $z = 0$ moves in the x-direction with a constant speed U_0 and at the same time rotates with a constant angular velocity Ω round a vertical axis.The fluid is initially at rest.A steady state of the flow is approached in which most of the motion is restricted to a boundary layer of the finite thickness.The solution is(see/10/)

$$u = U_0 \cdot e^{-\lambda z} \cos(\lambda z), \tag{47}$$

$$v = U_0 \cdot e^{-\lambda z} \sin(\lambda z), \tag{48}$$

with the boundary conditions

$$u + iv = U_0, \tag{49}$$

$$u + iv \to 0 \quad for \quad z \to \infty, \quad (i \quad imaginary \quad unit), \tag{50}$$

and $\lambda = \sqrt{\Omega/2\nu}$.It is interesting to note that for $z = \pi\sqrt{2\nu/\Omega}$,the flow is reversed as the consequence of the plate's rotation,Fig.2.The thickness of the boundary layer is $\delta \sim \sqrt{2\nu/\Omega}$,which tends to infinity for $\Omega \to 0$.

Other kinds of viscous boundary layers have been studied which arise due to a different balance of forces than that present in the Ekman boundary layer.Consider a confined circular cylinder filled with a homogeneous fluid in the state of solid–body rotation with a prescribed angular velocity Ω_0. If we suddenly change the angular velocity to $\Omega_1 > \Omega_0$,the interior region of the fluid is initially undisturbed and the balance between the pressure gradient and centrifugal force persists.The fluid near the horizontal boundaries begins to spin faster due to the influence of the viscous stress.The centrifugal force in this layer is increased so it becomes larger than the pressure gradient with the consequence ,that the fluid moves radially outward.Because of the continuity the fluid from the interior region is sucked into the boundary layer with the result that secondary flow (flow in the vertical cross section) emerges.The sense of this flow is radially outward in the horizontal Ekman layers (at the bottom and the top of the cylinder),upward(downward) at the vertical walls and finally radially inward to the axis of rotation.This flow persists until the fluid and the cylinder reach the new state of the solid–body rotation with the new angular velocity Ω_1 (spin–up effect)/6,7,10/.For adapting the flow to the vertical walls in the time period between the two solid–body rotations with angular velocity Ω_0 and Ω_1,it was found,that a set of two vertical shear layers(**Stewartson boundary layers**) of thickness $\delta \sim E^{1/4}$ and $\delta \sim E^{1/3}$ exist in order to make this adapting possible,as a consequence of a balance between the Coriolis force,pressure gradient,and the radial momentum diffusion.A layer of thickness $\delta \sim E^{1/4}$ serves mainly for adjusting the azimuthal velocity of the interior flow to the value of this component at the wall.A second thinner layer of thickness $\delta \sim E^{1/3}$ serves for the transport of a vertical mass flux of the order $E^{1/2}$,and to fulfil the no–slip boundary condition for the vertical velocity component/6,11,13/.Viscous layers may also emerge in the interior region of the flow to prevent the existence of sharp or discontinuous velocity profiles /12,22/,(see also Fig.1).

3.4 Flow between two Parallel Horizontal Disks.

Although in this and in the next section we study the flow in a somewhat "unrealistic" system of two horizontal disks,nevertheless, some facts we learn about the flow,will also be relevant for the flow in the Czochralski system.

Consider two infinite coaxial horizontal disks which rotate with angular velocities $\Omega(1+\epsilon_l)$ and $\Omega(1+\epsilon_l)$ for $0 < \epsilon_l, \epsilon_t << 1$. l and t refer to lower–and upper disk,and H is the vertical distance between disks,respectively. Set $L = H$ and $U = \epsilon\Omega H$ where $\epsilon = (\epsilon_l + \epsilon_t)/2$,so

that the Rossby number $Ro = \epsilon$.The relative vorticity is $\zeta_{rl} = 2\epsilon_l/\epsilon$ on the lower disk and $\zeta_{ru} = 2\epsilon_t/\epsilon$ on the upper disk.The Ekman condition (46) for lower and upper disks leads to

$$w_g = \frac{1}{2}\sqrt{E}(\zeta_g - 2\epsilon_L/\epsilon), \tag{51}$$

$$w_g = -\frac{1}{2}\sqrt{E}(\zeta_g - 2\epsilon_T/\epsilon). \tag{52}$$

Eliminating w_g we get

$$\zeta_g = \epsilon_L/\epsilon + \epsilon_T/\epsilon. \tag{53}$$

This means that the flow between the disks rotates with the average of the relative angular velocities of both disks,whereas the relation

$$w_g = \frac{1}{2}\sqrt{E}(\frac{\epsilon_T}{\epsilon} - \frac{\epsilon_L}{\epsilon}), \tag{54}$$

states that the fluid flows to the disk with larger angular velocity.This is the so-called **"Ekman pumping"**/7/. This also implies a radially inward flow at the slower disk and radially outward flow at the faster one.

3.5 Linear Spin-up.

We consider the linear spin-up effect ($Ro << 1$) in a simple system of two coaxial infinite horizontal disks with a vertical distance H.**Greenspan and Howard**/13/ solved the linear spin-up problem for arbitrary axisymmetric containers.Two time-scales are important in this process namely,(a) the rotation period $T_r = 2\pi/\Omega$,and (b) the viscous diffusion time i.e.the time needed for the vorticity to diffuse viscously to the mid plane $T_d = H^2/4\nu$.It will be shown that the time needed to establish the solid-body rotation is $T \sim E^{-1/2}$ which is shorter than the viscous diffusion time which is $T_d \sim E^{-1}$.

We now consider the following situation(see Moore/7/): For $t < 0$ the system is in solid-body rotation with an angular velocity Ω,but at $t = 0$ both disks are switched to the new angular velocity $\Omega(1+\epsilon)$,where $0 < \epsilon << 1$.We introduce the scaling $L = H, U = \epsilon\Omega H$,and $T = 1/\Omega$ so that the Rossby number $Ro = U/L\Omega = \epsilon$.

The faster spinning disks cause the formation of two Ekman layers in a time of order 1.The radially outward flow will be established in the Ekman layers so that,due to continuity ,the fluid from the interior region will be sucked into the layers,Fig.3.The arising circulation violates the geostrophic flow regime in the interior region.If we introduce cylindrical

coordinates r, ϕ, z then the geostrophic equation (14) implies that the radial component will be $u = 0$ (axisymmetric case) which is in contradiction with our present situation.The only possibility to retain the radial component u with $(Ro, E) << 1$ is to introduce the local acceleration term $\partial v/\partial t$.The velocities in the Ekman layers are of order 1 so the radial flux is of order $E^{1/2}$.This implies $u \sim E^{1/2}$ outside the Ekman layers.From eq.(56) (below) follows that $\partial v/\partial t \sim E^{1/2}$ or $\partial/\partial t \sim E^{1/2}$ because $v \sim 1$.This makes it possible to discard the terms $\partial u/\partial t \sim E$ and $\partial w/\partial t \sim E$(for $w \sim E^{1/2}$),so we get together with the continuity equation

$$2v = \partial p/\partial r, \tag{55},$$

$$\partial v/\partial t + 2u = 0, \tag{56}$$

,

$$0 = \partial p/\partial z, \tag{57}$$

$$\frac{1}{r}\frac{\partial(ru)}{\partial r} + \frac{\partial w}{\partial z} = 0. \tag{58}$$

From the above equations we see that the basic geostrophic flow $(0, v, 0)$ (eqs.(55),(57)) is violated by a weak meridional secondary flow $(u, 0, w)$ (eqs.(56),(58)).The vanishing of this secondary flow occurs,as we shall realize,on the time scale $E^{-1/2}$.

From the Ekman conditions we get

$$w_g = \frac{1}{2} \cdot \sqrt{E}[\frac{1}{r}\frac{\partial(rv)}{\partial r} - 2], \qquad on \qquad z = 0, \tag{59}$$

$$w_g = -\frac{1}{2} \cdot \sqrt{E}[\frac{1}{r}\frac{\partial(rv)}{\partial r} - 2], \qquad on \qquad z = 1, \tag{60}$$

Inspection of eqs.(55),(56),and (57) gives $p = p(r, t)$, $v = v(r, t)$,and $u = u(r, t)$.The integration of(58) gives

$$w = -\frac{z}{r} \cdot \frac{\partial(ru)}{\partial r} + f(r, t), \tag{61}$$

where $f(r, t)$ follows from eq.(59) i.e.

$$f(r, t) = \frac{1}{2} \cdot \sqrt{E}[\frac{1}{r}\frac{\partial(rv)}{\partial r} - 2], \tag{62}$$

and from eqs.(60),(61) we get for $z = 1$

$$\frac{1}{r}\frac{\partial(ru)}{\partial r} = \sqrt{E}[\frac{1}{r}\frac{\partial(rv)}{\partial r} - 2]. \tag{63}$$

By separation of variables $u(r,t) = r \cdot U(t)$ and $v(r,t) = r \cdot V(t)$ we get from eq.(63)

$$U(t) = \sqrt{E}(V(t) - 1), \tag{64}$$

and from eq.(56)

$$\dot{V}(t) + 2U = 0. \tag{65}$$

Elimination of $U(t)$ from eq.(65),by means of eq.(64),leads to

$$\dot{V}(t) = -2\sqrt{E}(V(t) - 1). \tag{66}$$

The solution of this ordinary differential equation with $V(0) = 0$ (initial condition) is

$$V(t) = 1 - e^{-2\sqrt{E}t}, \tag{67}$$

or

$$v(r,t) = r[1 - e^{-2\sqrt{E}t}]. \tag{68}$$

Similarly we get for the radial component $u = u(r,t)$

$$u(r,t) = -r\sqrt{E}e^{-2\sqrt{E}t}. \tag{69}$$

Eqs.(68),(69) show that the fluid in the interior region of the system spins up to the solid –body rotation while the secondary flow vanishes.The needed time in both cases is of order $E^{1/2}$,which is shorter by a factor $\sqrt{E}$ than the viscous diffusion time.

3.6 Forced Oscillations in a Rotating Fluid.

Rotating fluids possess an intrinsic stability in the sense that if the fluid particle is displaced from its initial position it will return to its position in a way which is not possible in a non–rotating fluid.If a particle in a fluid which rotates with a constant angular velocity Ω is displaced from its initial position with a speed u in an arbitrary direction,perpendicular to the axis of rotation ,the Coriolis force on the particle is $2\Omega u$ perpendicular to its direction,/8/.Consequently,the particle moves on a circular path of radius r.The balance between the Coriolis– and centrifugal force gives

$$\frac{u^2}{r} = 2\Omega u, \tag{70}$$

so that the radius of the circular path is

$$r = \frac{u}{2\Omega}. \tag{71}$$

The time the particle needs for one circle is

$$t = \frac{2\pi r}{u} = \frac{\pi}{\Omega}, \tag{72}$$

which is independent of the speed u of the particle. From this surprising result one concludes that the particle returns to its initial position twice during every revolution of the fluid.The angular frequency $2\pi/t = 2\Omega$ is named the **inertial or Coriolis frequency**.It is the fundamental frequency for a homogeneous rotating fluid.Due to this constraining property the rotating fluid can support internal wave motion,called **inertial waves**,which are not possible in non–rotating fluids.The existence of these waves can be demonstrated,for example,with a small disk oscillating at a frequency β in the direction normal to its own surface in the cylindrical container filled with a homogeneous fluid and rotating with a constant angular velocity Ω. Besides,we assume that the disk's plane is perpendicular to the axis of rotation.

The problem of forced oscillations was first observed by **Görtler**/14/ and has since been studied by **Morgan**/15/,**Oser**/16/,/17/,**Reynolds**/18/,and in the case of a rotating spherical container by **Aldridge** and **Toomre**,/19/. We consider the system of equations (7),(8) for the case in which the non–linear advective term and the viscous term can be neglected

$$\nabla \cdot \vec{u} = 0, \tag{73a}$$

$$\partial\vec{u}/\partial t + 2\vec{\Omega} \times \vec{u} = -\nabla P, \tag{73b}$$

where eq.(73b) now relates the perturbation vector velocity $\vec{u}$ and the perturbation of the pressure P.We suppose that the relation

$$(u, v, w, P) = e^{i\beta t}(U, V, W, \tilde{P}), \tag{74}$$

is valid. Here β,in the time–dependent part of eq.(74),is the forcing frequency,and the variables $U = U(r, \phi, z)$,$V = V(r, \phi, z)$,$W = W(r, \phi, z)$,and $\tilde{P} = \tilde{P}(r, \phi, z)$ are given in the cylindrical coordinate system.If we now introduce relation (74) into eqs.(73a),(73b) we get,using elimination, in component form (axisymmetrical case)

$$\{\frac{\partial^2}{\partial r^2} + \frac{1}{r}\frac{\partial}{\partial r} - \frac{1}{r^2} + \frac{\beta^2 - 4\Omega^2}{\beta^2}\frac{\partial^2}{\partial z^2}\}(U; V) = 0, \tag{75}$$

$$\{\frac{\partial^2}{\partial r^2} + \frac{1}{r}\frac{\partial}{\partial r} + \frac{\beta^2 - 4\Omega^2}{\beta^2}\frac{\partial^2}{\partial z^2}\}(W; \tilde{P}) = 0, \tag{76}$$

Page 17 The character of the system of eqs.(75),(76) depends on the value of the forcing frequency β.Thus,for $\beta > 2\Omega$ the system is elliptic,for $\beta = 2\Omega$ parabolic and for $\beta < 2\Omega$ hyperbolic,respectively.In the hyperbolic case ($\beta < 2\Omega$) there exist real characteristic surfaces

$$z = r\sqrt{(4\Omega^2 - \beta^2)/\beta^2} + C. \tag{77}$$

The angle ϕ between a characteristic surface and a plane $z = const.$ is

$$\cos\phi = \frac{\beta}{2\Omega}. \tag{78}$$

For $\beta = 2\Omega$ the characteristic surfaces are horizontal, and beyond this limiting characteristic value,i.e.for $\beta > 2\Omega$,the characteristic surfaces disappear completely and the flow performs a potential motion. It is important to note that for $\beta = 0$ (no disturbance) we get the Taylor-Proudman column.

These surfaces are locations of discontinuities of the solution of eqs.(75),(76),which in the case of real fluids will be formed by means of internal viscous boundary layers.This was also experimentally found by **Oser/17/**.Moreover,it is interesting to remark that similar characteristic surfaces were found in a stratified fluid by **Görtler/20/**.This analogy between rotating fluids and stratified fluids originates from the control of the fluid behavior by respective constraints of rotation and stratification /21/.

For numerical simulations of forced oscillations in a rotating fluid see Sec.6.2.

4.Stability of the Rotating Flow.

The subject of hydrodynamic stability is certainly one of the central problems of fluid mechanics.It is concerned with seeking the answers to questions such as:(1) when and how a given laminar flow will break down,(2) how it will develop with the time,and (3) will there be a transition to turbulent flow.The application of the subject is very wide.It reaches across many scientific disciplines such as meteorology, oceanography,geophysics,etc.Also it found important areas of application in the Czochralski crystal growth process,such as stability of the solid–liquid interface,stability of the Ekman layer attached to it,stability of the buoyancy driven flow etc.According to **Ristorcelli and Lumley/68/** "... There are ten (at least) possible sources of instability arising from the interaction between various body forces and velocity gradients in the (Czochralski) melt flow...".

Generally,one may say that instability is caused through disturbance of the equilibrium of inertia,viscous and external forces in the fluid.The external forces we are interested in

are the **buoyancy force** in a Boussinesq fluid, the **surface tension**– and the **magneto fluid dynamic force**. Moreover,in a rotating fluid we regard Coriolis– and centrifugal force as external forces.For instance,in the **Bénard** problem between two horizontal planes heated from below(above some critical temperature difference between the planes)the stabilizing effects of viscosity and thermal conductivity are disturbed by the destabilizing buoyancy,so that thermal (free) convection emerges.A similar problem exists in the case of **Couette flow** of a homogeneous fluid between two coaxial cylinders.In this flow an overturning instability occurs due to the centrifugal force if the **circulation** around the inner cylinder is greater than the circulation around the outer cylinder.The surface tension force,which resists the increase of area of a free surface,as well as the magnetic force on an electrically conducting fluid (e.g.Si-melt),have a stabilizing influence on the flow.Also the viscous force stabilizes the flow through the dissipation of energy of existing disturbances.On the other hand the viscosity must diffuse momentum,a process which under certain circumstances may lead to instability,even if the same flow of an inviscid fluid may be stable,/23/.Thermal conductivity tends to smooth out temperature differences of a disturbance,which has also a stabilizing influence on the flow.There are many other factors which influence the stability of the flow,e.g.acceleration of the flow,boundaries, etc.

The onset of the instability is conveniently characterized by means of dimensionless numbers which generally give the ratio between the stabilizing–and destabilizing forces,e.g.the **Reynolds number** (inertia force/viscous force), the**Rayleigh number** (buoyancy force/ diffusive force),the **Prandtl number** (diffusion of momentum/ diffusion of heat),etc.

In the next section we consider the problem of **baroclinic instability** which plays an important role not only in dynamical meteorology but also in Czochralski crystal growth.

4.1 Flow due to an Impressed Horizontal Temperature Gradient in a Rotating Annulus.

To solve the problem of baroclinic instability in dynamical meteorology,one has to explain under which conditions the presence of a temperature field decreasing from equator to the North Pole (due to unequal heating),which in fact provides a reservoir of available potential energy,will be released by a large scale wave.We will discuss later how this is related to Czochralski melts.

A simple laboratory model for this complicated process is a fluid filled cylindrical annulus

with vertical surfaces at different but constant temperatures. An impressed radial temperature difference $T_1 - T_2 > 0$ (T_1,T_2 are the temperatures at the outer– and inner vertical wall,respectively) simulates the condition given along the meridian from equator to the north pole.The annulus rotates with a prescribed angular velocity Ω.Following **Hide** and **Mason** /24/ we know that in a system which is symmetrical with respect to the rotation axis and which does not rotate ($\Omega = 0$),the flow will be confined to meridional planes.The warmer fluid is rising at the warm wall and passing to the cold wall,whereas the cold fluid is sinking at the cold wall and passing to the warm wall, respectively.Thus,fluid elements exhibit an overturning motion in which the associated vorticity vector points to the azimuthal direction.On the contrary,if $\Omega \neq 0$ gyroscopic torques ($\sim \nabla \times (2\vec{\Omega} \times \vec{u})$ for a Boussinesq fluid) tend to prevent meridional motion. If $|\vec{\Omega}|$ is large enough then the Coriolis force will dominate the inertial and viscous forces at least in the main body of the fluid.In this case,taking the curl of eq.(6) we get

$$\nabla \times (2\vec{\Omega} \times \vec{u}) = -\vec{g}^* \times \nabla(\frac{\rho_1}{\bar{\rho}}). \tag{79}$$

From eq.(79) it is clear that the velocity vector $\vec{u}$ is mainly horizontal if it is also horizontal at the boundaries. Flows satisfying eq.(79) are inefficient to convert potential energy into kinetic energy and thus conventing the heat in directions perpendicular to the vector $\vec{\Omega}$.Sloping convection (or so-called **baroclinic waves**)will develop if the angular velocity $|\vec{\Omega}|$ is sufficiently large,in spite of the axial symmetry of the boundary conditions. In this case the flow will be non–axisymmetric,with ρ_1, P,and $\vec{u}$ depending on the azimuthal coordinate ϕ. Also,the trajectories of fluid particles will make a small angle to the horizontal.Moreover,from eq.(79) one can infer that the convective heat transfer should generally decrease with increasing $|\vec{\Omega}|$.These inferences were confirmed through experimental and theoretical studies by **Hide** and **Mason**/24/.

An interesting question is the problem of stability of such a flow.For a moderate angular velocity and for boundary conditions symmetrical about the rotation axis,a symmetrical laminar flow exists,which spirals around the rotation axis. If the rotation rate or temperature difference or both is increased the flow becomes unstable and non–axisymmetric. There are altogether four different flow regimes:(1)symmetrical flow, (2) steady waves,(3) vacillation,and (4) irregular (turbulent) flow. It has been experimentally shown that the wave patterns extend almost over the entire depth of the fluid/24/.The above four flow regimes are distinct and determined by the value of two parameters.These two parameters

are

$$F = \frac{4\Omega^2(R_1 - R_2)^5}{\nu^2 H} \quad , \quad \Theta = \frac{gH\delta\rho}{(R_1 - R_2)^2\bar{\rho}\Omega^2}, \tag{80}$$

where g is the gravitational acceleration, H a characteristic length(height of the annulus), R_1, R_2 the outer–and the inner radius of the annulus,and $\delta\rho = |\rho(T_1) - \rho(T_2)|$,respectively. **Fultz**/25/ has shown that if the different working fluids have the same kinematic viscosity and same Prandtl number then the parameters F, Θ determine a unique stability curve in the plane (F, Θ). However,the separation of different wave regimes within the area of instability is very dificult /25/.

It is interesting to note that a similar baroclinic instability (wave formation) was observed in the Czochralski system during crystal growth from oxide melts/26–29/.It was shown that small changes in the balance between the centrifugal force due to crystal rotation and buoyancy force due to density gradients have dramatic effects on the flow patterns and the crystal quality.In some cases,the instability interrupted the crystal growth /26/ or it resulted in interface break–down and dislocation formation /29/.

For the numerical simulation of the baroclinic instability in silicon melt see Sec.7.1.

II. NUMERICAL SIMULATIONS OF THE CZOCHRALSKI BULK FLOW.

5.Introduction

For more than 15 years numerical simulations have been undertaken to get quantitative information about the flow and the accompanying temperature distribution in the melt /30-43/.In spite of the fact that this work has given considerable insight into the basic properties of the flow ,it was not quite satisfactory as **Hurle** /44/ initially pointed out,for two main reasons:

(1) The Ekman layer at the solid-liquid interface is very thin (sec.3.3),so it was not possible to resolve it and compute the flow within it.

(2) Mathematical models for both stationary and time-dependent simulations have been limited to axisymmetric flows,with the consequence that non-axisymmetric flow transitions were not accessible to these simulations.

Some other simplifications of the mathematical model such as flat free surface without meniscus and planar solid-liquid interface,though important,remain to be considered in the next stage of improvement of these models. However,this problem was studied numerically by **Kobayashi** /37/,by **Derby** and **Brown** /47/ and recently by **Kopetsch** /46/,in the case of axisymmetric flow. **Lamprecht et al.** /45/ threw also some light on this point.

In order to meet the first two demands cited above we split the problem into two parts:

(1) In the first part we study the forced convection (**Cochran flow**) in an axisymmetric model but on a very fine discrete mesh with the aim to resolve the Ekman layer.

(2) In the second part we study the flow-and temperature field in a three-dimensional model under various external conditions.

The need for splitting the problem into two parts is the consequence of limited capacity of computer's memory and available CPU-time.

5.1 Notations and Parameters.

In this section we summarize the necessary symbols and notations we have used to describe

our model.

$\vec{r} \equiv (r, \phi, z)$ Position vector in a stationary **Eulerian** cylindrical coordinate system.

$\vec{u} \equiv (u, v, w)$ Flow velocity vector with u radial–,v azimuthal–,and w vertical velocity component

P Pressure

ρ Density

$p = P/\rho$ Ratio of pressure to density

T Temperature

$\bar{T}$ Temperature difference between melt temperature and the averaged temperature used in Boussinesq approximation

μ Dynamic viscosity

$\nu = \mu/\rho$ Kinematic viscosity

κ Thermal conductivity

c_p Specific heat(at constant pressure)

$\alpha = \kappa/\rho c_p$ Thermal diffusivity

$\vec{g} \equiv (0, 0, -g)$ Gravity acceleration vector

β Coefficient of volumetric expansion

R_s Crystal radius

R_c Crucible radius

Ω_s Angular velocity of crystal

Ω_c Angular velocity of crucible

H Melt depth

T_s Solid–liquid interface temperature

T_c Temperature at the crucible wall

$\delta T \equiv T_c - T_s$ Temperature difference between crucible wall and solid–liquid interface

γ Surface tension coefficient

Gr Grashof number

Pr Prandtl number

Pe Péclet number

E Ekman number

Ra Rayleigh number

Re Reynolds number

Ro Rossby number

$\delta r, \delta\phi, \delta z$ Discretization in the radial–,azimuthal–,and the vertical direction

δt Time step

$(\cdot)_r$ means $\partial(\cdot)/\partial r$ and similarly for other derivatives.

5.2 Mathematical Model and Boundary Conditions.

The general three–dimensional configuration of our model is given in Fig.4.It is an idealization of a real Czochralski crystal growth system,in which the free surface of the melt and solid–liquid interface are assumed to be flat and at constant level during the crystal pulling process.

The equations governing the time– dependent incompressible viscous flow (in a **stationary Eulerian**coordinate system) in the crucible including thermal effects by consideration of density changes in the buoyancy term are the **continuity equation**

$$\nabla \cdot \vec{u} = 0, \tag{81}$$

the **Navier–Stokes** equations with **Boussinesq** approximation,already given in numerically convenient form

$$(\vec{u})_t = -\nabla \cdot (\vec{u}\vec{u}) - \nabla p - \nu \nabla \times (\nabla \times \vec{u}) - \beta \bar{T} \vec{g}, \tag{82}$$

and the convectice **heat conduction** equation also given in numerically convenient form

$$(T)_t = -\nabla \cdot (\vec{u}T) + \alpha \nabla^2 T. \tag{83}$$

In a three–dimensional (Eulerian) cylindrical coordinate system,eqs.(81)–(83) read as follows:

$$\frac{1}{r}(ru)_r + \frac{1}{r}v_\phi + w_z = 0. \tag{84}$$

$$(u)_t = -\frac{1}{r}(ru^2)_r - \frac{1}{r}(uv)_\phi - (uw)_z + \frac{v^2}{r} - p_r - \nu[\frac{1}{r^2}(rv_\phi)_r - \frac{1}{r^2}u_{\phi\phi} - u_{zz} + w_{rz}]. \quad (85)$$

$$(v)_t = -\frac{1}{r}(ruv)_r - \frac{uv}{r} - \frac{1}{r}v_\phi^2 - (vw)_z - \frac{1}{r}p_\phi - \nu[\frac{1}{r}w_{\phi z} - v_{zz} - (\frac{1}{r}(rv)_r)_r + (\frac{1}{r}u_\phi)_r]. \quad (86)$$

$$(w)_t = -\frac{1}{r}(ruw)_r - \frac{1}{r}(vw)_\phi - w_z^2 - p_z - \nu[\frac{1}{r}(ru_z)_r - \frac{1}{r}(rw_r)_r - \frac{1}{r^2}w_{\phi\phi} + \frac{1}{r}v_{\phi z}] + \beta\bar{T}g. \quad (87)$$

$$(T)_t = -\frac{1}{r}(ruT)_r - \frac{1}{r}(vT)_\phi - (wT)_z + \alpha[\frac{1}{r}(rT_r)_r + \frac{1}{r^2}T_{\phi\phi} + T_{zz}]. \quad (88)$$

In order to complete the mathematical model we still need,in addition to eqs.(84)–(88),the appropriate initial and boundary conditions.For the three–dimensional model they are as follows:

The initial condition:

At time $t = 0$ we define the velocity components,the pressure,and the temperature inside the geometry.Generally we start with the condition:$u = v = w = p = T = 0$.

The velocity boundary conditions:

(1) For the radial– and vertical velocity components u and w we demand the **no–slip** boundary condition at all rigid boundaries and the **free–slip** boundary condition at the free surface.

Alternatively,if **thermocapillary convection** is to be included,then boundary conditions for the u–and v velocity component at the free–surface now read:

$$(u)_z = (1/\mu)(\gamma)_T(\vec{i}_r \cdot \nabla T), \quad (89a)$$

$$(v)_z = (1/\mu)(\gamma)_T(\vec{i}_\phi \cdot \nabla T), \quad (89b)$$

where γ denotes the surface tension coefficient and μ is the dynamic viscosity.

(2) The boundary conditions for the tangential component v at the rigid boundaries include the angular velocities Ω_c and Ω_s of the given crucible–and crystal rotation,respectively.At the free surface the free–slip condition is used.

Thermal boundary conditions:

The thermal boundary conditions include the constant temperature T_s (in the calculations we use $T_s = 0$) at the solid–liquid interface and generally a variable temperature distribution $T_c(\phi) - T_s$ along the perimeter of the crucible wall.

At the bottom of the crucible we demand that no heat loss occures,i.e.that the normal component of ∇T is equal to zero.

At the free surface the following temperature boundary condition must be fulfilled:

$$\kappa_l(\partial T/\partial z)_{z=H} + \epsilon\sigma(T^4 - T_w^4) = 0, \tag{90}$$

where κ_l is the thermal conductivity, ϵ the emissivity coefficient, σ the**Stefan–Boltzmann constant**,and T_w the temperature of enclosure of the system.

The boundary conditions at the **vertical symmetry axis** of the geometrical configuration (crucible axis) are more difficult numerically than the other conditions,so they will be described separately.

(1) It is clear (mathematically) that the radial velocity component u at the axis should be zero,for otherwise,more than one u–component at the same point will be defined.This is easily seen in fig.5.

(2)The appropriate boundary conditions for the components v,w and the temperature T, which are not placed at the axis (**staggered grid**), at the vertical cross–section $\phi = \phi_j$ should be defined by means of the same variables at the vertical cross–section $\phi = \phi_j + 180^0$ and vice versa.For example,the boundary values of the temperature T at the vertical cross–sections $\phi = \phi_j$ and $\phi = \phi_j + 180^0$ are: $T(1, \phi_j, k) = T(2, \phi_j + 180^0, k)$ and $T(1, \phi_j + 180^0, k) = T(2, \phi_j, k)$.The same is valid for the other variables.

5.3 Numerical Method.

To turn eqs.(84)–(88) into a practical scheme for computation,they are expressed in finite difference form on a three–dimensional cylindrical mesh,Fig.5. The numerical method we use in our calculations is a variant of the famous **Marker and Cell Method (MAC)**/61/, for the solution of the flow problems for an incompressible fluid.It is an explicit finite–difference method using forward differences for the first order derivatives in time and central differences for the spatial derivatives. Consequently,the method is characterized by a truncation error of $O(\delta t)$ in time and of $O(h^2)$ in space, where h denotes the largest spatial dimension of the computational cell.For the convective heat equation,however, we prefer to use the **DuFort–Frankel** discretization scheme in order to avoid rather severe stability restrictions due to the relatively large thermal diffusivity coefficient of metallic melts.

The region in which the computations are to be performed is divided into a set of small cells having edge length δr,$r\delta\phi$ and δz. In each cell the velocity components are located at the cell faces,while pressure and temperature values are at the cell center (staggered grid),Fig.5. Cells are labelled with a set of indices (i, j, k) which determine the coordinates of the cell center.

A time-dependent solution of the system (84)-(88) is performed in three stages.In the first stage we simply advance the velocity components from the previous state at time $t = t_m$ to the new state $t = t_m + \delta t$ thus, in this stage all calculations are performed explicitly. However,this procedure does not lead to a velocity field with zero divergence,that is,mass will not be conserved. The reason is that at this stage of computation the proper pressure value per cell is not yet known. Thus,in the second stage, we have to correct the velocity components in each cell in such a way that the zero divergence condition will be fulfilled. This is done by determining the appropriate pressure in each cell which then leads to the proper corrections of the velocity components.

Since the correction of velocity components in one cell will change the velocity components in neighboring cells, the calculations in this stage must be performed iteratively, until all cells have reached a zero divergence.This technique was first developed by **Chorin** /62/.We found that this technique is much faster than the original MAC technique. Moreover,it seems to be better suited for the vector- and parallel processing computers.For more details on this technique see **Hirt and Cook** /63/.

In the third stage of computation we calculate the new temperature field.Here,because of the coupling of eqs. (84)-(87) and (88), iterations are generally necessary for the calculation of the velocity components u,v,w and the temperature T. However,in the case of a large thermal diffusivity coefficient α as well as the small time step δt such iterations are not needed.

6.Numerical Results:Axisymmetrical Model.

6.1 Flow due to a Rotating Disk in the Czochralski Geometry.

Here,we study numerically the forced convective flow due to crystal rotation in the Czochralski geometry but without the influence of the buoyancy or free convective flow in the system.This will be compared with the analytical results by **von Karman**/64/ and **Cochran** /65/.

The governing equations of our model are essentially the same as those given for the three–dimensional flow (eqs.(84)–(87)).Assuming rotational symmetry of the flow field all ϕ–derivatives will be equal zero.Also the buoyancy term $\beta\bar{T}g$ in eq.(87) is equal zero, because of the absence of a non–homogeneous temperature field in the system(isothermal flow).The initial and boundary conditions from Sec.5.2 are also valid in this case. The only difference is in the conditions for the components w and v at the vertical axis.These conditions are now $\partial w/\partial r = 0$ and $\partial v/\partial r = 0$, for the assumed symmetry of the flow.

The analytical solution due to von Karman is valid for an infinite disk which rotates with a constant angular velocity Ω_s.The solution is given in the form

$$u = r\Omega_s F(\zeta); v = r\Omega_s G(\zeta); w = \sqrt{\nu\Omega_s} H(\zeta); p = \rho\nu\Omega_s P(\zeta), \tag{91}$$

where

$$\zeta = z\sqrt{\Omega_s/\nu}, \tag{92}$$

is the reduced axial distance from the disk.It is interesting to note that ,for an infinite disk, the important vertical velocity component w is not dependent on the radial distance r from the axis,eq.(91).

The functions $F(\zeta), G(\zeta), and\ H(\zeta)$ are plotted in Figs.6a–6c and Figs.7a–7c together with the numerical results ($functions\ \hat{F}, \hat{G}, and\ \hat{H}$). The numerical results were obtained for a Czochralski geometry with $R_c = 3cm, R_s = 1.2cm, H = 4cm$,and a working fluid with the kinematical viscosity $\nu = 0.0033cm^2/s$ of molten silicon.In this case we used a very fine discretization with 202×268 cells with $\delta r = \delta z = 0.015cm$, corresponding to about 5 cells in the boundary layer at the disk.

Two different cases with $\Omega_s = 10rpm$ (Figs.6a–6c) and $\Omega_s = 50rpm$ (Figs.7a–7c) are simulated,whereby the numerical results are given for the functions $\hat{F}, \hat{G}, and\ \hat{H}$ at three vertical profiles for $r = 0.02cm, r = 0.58cm$ and $r = 1.19cm$,respectively. The functions $\hat{F}, \hat{G}, and \hat{H}$ were obtained from the expressions

$$\hat{F}(r,\zeta) = \frac{u(r,\zeta)}{r\Omega_s}; \hat{G}(r,\zeta) = \frac{v(r,\zeta)}{r\Omega_s}; \hat{H}(r,\zeta) = \frac{w(r,\zeta)}{\sqrt{\nu\Omega_s}}, \tag{93}$$

where u,v and w are the numerically calculated velocity components.From the comparison of the series of Figs. 6a–6c ($\Omega_s = 10rpm$)and Figs.7a–7c($\Omega_s = 50rpm$) one clearly infers that:

(1)Contrary to the analytical solution,the important axial component w is **not independent** of the position on the disk in the Czochralski model. Consequently, one can expect a non-uniformity of the multicomponent crystals since the effective segregation coefficient depends on the flow pattern.Besides,the axial component w grows slowlier than $\sqrt{\Omega_s}$ as can be seen from Figs.6a–6c and Figs.7a–7c,respectively.

(2) There is also a difference between the analytical and numerical solutions of the functions G *and* $\hat{G}$ and F *and* $\hat{F}$, respectively.The numerically calculated function $\hat{G}$ (circles)changes faster than the analytically calculated function G for smaller values of ζ,but contrary to the function G,the function $\hat{G}$ tends to zero slowlier for larger values of ζ.This tendency is independent of the disk's rotation rate.A similar relation exists between the functions F *and* $\hat{F}$ but only for a smaller rotation rate.In the case of higher rotation rates the function $\hat{F}$ tends faster to zero for larger values of ζ than the analytical solution F.

As the above discussion shows,there is a considerable difference between the flow field in the vicinity of a rotating disk in the Czochralski geometry and that in the vicinity of an infinite rotating disk.An important consequence is,that the vertical velocity component w,which is important for the transport of material just outside the boundary layer at the growth interface,depends on the radial position.

6.2 Forced Oscillations in a Rotating Fluid.

A rotating fluid can under certain conditions support inertial waves as was discussed in section 3.6.Here,we numerically simulate this kind of flow field in a rotating fluid of the same kinematical viscosity as molten silicon. The Czochralski geometry is given with $R_c = 5cm$, $R_s = 1cm$ and $H = 10cm$. The angular velocity of the crucible is $\Omega_c = 40rpm$. The discretization of the mathematicl model is in this case $\delta r = \delta z = 0.05cm$ and the governing equations are identical with those in sec.5.2.The numerical simulations were performed under the following conditions:

(1)The crucible was rotated with angular velocity $\Omega_c = 40rpm$ for $1600s$ of physical time until a steady- state rotating flow field was reached.

(2)Because the vertical oscillations of the disk,which in this case is at the top of the free surface(Figs.8a–8d), are difficult to simulate numerically,the rotating flow field was instead disturbed by an oscillating vertical velocity component of the amplitude $A = 0.5cm/s$.

(3)The forced frequency β of this oscillation was chosen so that the relation

$$\frac{\beta}{2\Omega_c} = 0.75, \tag{94}$$

is valid,where Ω_c is now in Rad/s.The relation (93) define an angle θ between the characteristic surfaces and the plane $z = H$ of $\theta = 41.4°$(see (78) in sec.3.6).

Figs.8a–8d show the streamlines of the flow field at $t = 2061.25s$ of physical time and for one period of oscillation of the vertical velocity component w.The characteristic lines in the vertical cross–section through the system at $\phi = 0°$ can clearly be seen in spite of the damping effect of the viscosity.The computational angle $\hat{\theta}$ is in this case $41.6°$ which is in excellent agreement with the theoretical value of θ.

An additional effect shows up in Figs.8a–8d. If one compares Fig.8a and Fig.8c which are apart half a disturbance period in time,one finds that the corresponding vortices change their sense of rotation (full–and broken lines).The same is valid for Fig.8b and Fig.8d.In our opinion this interesting phenomenon has not been reported in the literature so far.However,this problem deserves a more detailed study than it is given here.

These phenomena could also have an important implication on the Czochralski crystal growth, especially in those cases, in which both the crystal and crucible are rotated and the solid–liquid interface is inclined to the rotation axis of the crystal.

7.Numerical Results:Three–Dimensional Model.

7.1 Baroclinic Instability.

A three–dimensional model of the Czochralski crystal growth system is used here with $R_c = 3.15cm, R_s = 1.2cm, H = 4cm$ and the molten silicon as the working fluid.The governing equations of the mathematical model are identical with those given in sec.5.2 (eqs.(84) –(88)).We also use the same boundary conditions as given in sec.5.2. The only exception is the thermal boundary condition at the crucible wall which is now at the constant temperature T_c.The model is discretized by $\delta r = \delta z = 0.07cm$ and $\delta\phi = 3°$.

Two dimensionless parameters F and Θ define a unique stability curve in the (F, Θ) plane(sec.4.1)

$$F = \frac{4\Omega_s^2(R_c - R_s)^5}{H\nu^2}; \Theta = \frac{gH\beta\delta T}{\Omega_s^2(R_c - R_s)^2}. \tag{95}$$

We start the simulation for $F = 1.3 \cdot 10^8 (\Omega_s = 80rpm)$ and vary the parameter Θ through a change of the temperature at the crucible wall.

1.Case:$F = 1.3 \cdot 10^8$ and $\Theta = 0.032(\delta T = 15^0)$.

Figs.9a and 9b show the projection of the flow and the corresponding temperature field at the horizontal plane $z = 3.965cm$,i.e.$0.035cm$ below the free surface of the model, and for $t = 225s$ of physical time. Both,the flow field and the corresponding temperature field are perfectly symmetric for the given F and Θ parameters.

2.Case:$F = 1.3 \cdot 10^8$ and $\Theta = 0.053(\delta T = 25^0)$.

Figs.10a–10f show the projection of the flow and the corresponding temperature field for $t = 288.5s$ of physical time,at three horizontal planes ,i.e. $z = 3.965cm$, $z = 1.920cm$,and $z = 0.035cm$,respectively.Both,the flow field and the corresponding temperature field are clearly asymmetric at all three horizontal planes,in agreement with experimental results, see Sec.4.1. For $z = 3.965cm$ the flow field clearly shows two protuberances,whereas the coresponding temperature field is elongated in the direction of those protuberances.A similar behavior of the flow and the temperature field can be seen at other other planes (Figs.10c–10f).The protuberances and temperature field are slowly rotating in the direction of the disk's rotation with an angular velocity of approximately $1.3rpm$.It is interesting to note that,in spite of rotational symmetry of the boundary conditions,the

instability is initiated only through the limited precision in the computation of the pressure field ($\epsilon \leq 10^{-5}$).

Unfortunately,the study of this interesting phenomenon demands a vast amount of computer time so that we were not able to scan the stability curve in more detai.However, in our opinion it is for the first time that the baroclinic instability has been observed (numerically) in Si–melts.

7.2 Instability of the Buoyancy driven Convection.

The Czochralski crystal growth process is mainly transport controlled because the high temperatures present in the system readily generate high temperature gradients which are responsible for both convective and conductive heat transport /44/. Since for large Grashof numbers($Gr = g\beta L^3 \Delta T/\nu^2$,$L$ is the characteristic length of the system) the Peclet number will be of order $Gr^{1/2}Pr$ (Pr denotes the Prandtl number,$Pr = \nu/\alpha$,which for the Si–melt is of order $3 \cdot 10^{-2}$),it is to be expected that,except in the boundary layer,the temperature distribution in the bulk will be determined largely by convection.For this reason it is important to find out the conditions for which the buoyancy driven convection will be unstable,i.e.it will change from an axisymmetrical flow mode to an asymmetrical one (in Tables 1a,1b:o $\equiv$ *symmetrical flow* and • $\equiv$ *asymmetrical flow*).

In order to initiate instability in the numerical experiment we superimposed a small temperature disturbance $\delta T = 10^{-7} \cos\phi(C^o)$ ($\phi \equiv$ *azimuthal coordinate*)over the given constant temperature T_c at the crucible wall.

In the present study,36 related cases were simulated with material parameters of Si–melts. 27 experiments were performed in which,for a given crucible radius $R_c = 3cm$,the crystal radius R_s ,melt depth H,and temperature difference ΔT were successively varied(Table 1a).Also, for given $R_c = 6cm$ and $H = 4cm$ 9 experiments were performed,in which ΔT and R_s were varied (Table 1b).

Table 1a

R_c=3cm	H=2cm			H=4cm			H=6cm		
$R_s(cm)$	δT=5K	δT=10K	δT=15K	δT=5K	δT=10K	δT=15K	δT=5K	δT=10K	δT=15K
1.0	o	o	o	o	o	o	o	•	•
1.5	o	o	o	o	o	•	•	•	•
2.0	o	o	•	o	•	•	•	•	•

Table 1b

R_c=6cm	H=4cm		
$R_s(cm)$	δT=5K	δT=10K	δT=15K
2.0	o	o	o
3.0	⊛	⊛	⊛
4.0	⊛	⊛	⊛

The governing equations and the boundary conditions of the mathematical model are identical with those given in sec.5.2 (eqs.(84)-(88)).The only difference is the thermal boundary condition at the crucible wall which is now

$$T_c(\phi) = T_c + 10^{-7}\cos(\phi). \tag{96}$$

Discretization parameters are:$\delta r = \delta z = 0.15cm$, $\delta\phi = 4°$ and $\delta t = 0.0015s$.

7.2.1 Numerical Results.

Tables 1a,1b show 36 simulated cases in which for the given radii of the crucible($R_c = 3cm$ and $R_c = 6cm$) the geometrical parameters R_s, H and the temperature difference δT between the crucible wall and the solid–liquid interface are successively varied. At the same time no rotations of the crucible and crystal were present in the system.It is evident that the small temperature disturbance ,which was superimposed over the constant temperature T_c at the crucible wall,initiates the instability of the flow.**Moreover,the numerical results clearly show that the instability of the buoyancy driven flow is possible even in the presence of small temperature differences ,depending on the geometrical parameters R_c, R_s and H ,respectively.**Therefore,it is interesting to find out,if possible, the critical Grashof number at which the flow transition takes place.We are aware of the fact,that in a real Czochralski crystal growth not only the Grashof number,but also the other relevant parameters could play an important role in the flow transition.Thus,one must be careful when making a statement, e.g.,that a flow transition takes place at a definite Grashof number/69/.

If there is such a definite critical number in our simulated cases,then the characteristic length L must be a function of all three geometrical parameters,i.e.$L = f(R_c, R_s, H)$. One

possibility to estimate the characteristic length L is to use the following relation /70/:

$$L_i \approx u_i^2/g\alpha\Delta T, i \;=\; 1,\cdots,36, \tag{97}$$

for $Gr \gg 1$.In our case we choose $u_i = |\vec{u}_{max}|_i$,i.e. the norm of the maximum velocity vector $\vec{u}_i$ we find out in each simulation,respectively.

Now we make the following assumption for the characteristic length L:

$$L_m^3 = A_{ijk}(R_c)_m^i(R_s)_m^j H_m^k, m \;=\; 1,\cdots,36, \tag{98}$$

where the right–hand side of eq.(98) is a homogeneous polynomial of third degree $(i+j+k=3)$.It follows from the least–squares approximation in (98) ,that the combinations $(R_c^2R_s),(R_cR_s^2),(R_s^2H)$,and (R_sH^2) have the 4 largest coefficients A_{ijk} in the polynomial and,thereby,have more influence on the characteristic length L than the other combinations.Finally,the computed Grashof numbers are given in Tables 2a,2b.

Table 2a

R_c=3cm	H=2cm			H=4cm			H=6cm		
$R_s(cm)$	δT=5K	δT=10K	δT=15K	δT=5K	δT=10K	δT=15K	δT=5K	δT=10K	δT=15K
1.0	0.22×10^5	0.44×10^5	0.66×10^5	0.29×10^6	0.59×10^6	0.88×10^6	1.10×10^6	2.21×10^6	3.31×10^6
1.5	0.12×10^6	0.25×10^6	0.37×10^6	0.63×10^6	$\overline{1.25\times10^6}$	1.88×10^6	3.57×10^6	7.14×10^6	1.07×10^7
2.0	0.39×10^6	0.78×10^6	1.18×10^6	0.76×10^6	1.52×10^6	2.28×10^6	4.62×10^6	9.24×10^6	1.39×10^7

Table 2b

R_c=6cm	H=4cm		
$R_s(cm)$	δT=5K	δT=10K	δT=15K
2.0	0.47×10^6	0.93×10^6	$\overline{1.40\times10^6}$
3.0	1.19×10^6	2.38×10^6	3.57×10^6
4.0	3.86×10^6	7.72×10^6	1.16×10^7

Comparison of Tables 1a,1b with Tables 2a,2b shows,that the critical Grashof number is approximately $Gr_c \approx 1.2\times10^6$ which is in excellent agreement with the result of **Bottaro** and **Zebib**/67/$(Ra = 10^4)$.

However,two overlined results in Tables 2a,2b are in disagreement with the critical Grashof number.One possible reason for this could be that 600s of simulation (real time) was too

short in order to reach the flow transition (instability).Anyway,both Grashof numbers are close to the critical Grashof number.

Next,we shall discuss some characteristic plots of the unstable convective flow in the model.Fig.11a shows the projection of the velocity vectors on the horizontal plane $0.075cm$ beneath the the free surface,for the case $R_c = 3cm$, $R_s = 1.5cm$, $H = 6cm$, $\delta T = 5K$,at time $t = 290s$ of real time.The flow is quite asymmetric and shows two well defined vortices.These vortices are not stationary but change continuously their position and form, depending on time.Also,a strong well is present at the position $r = 2cm$ and $\phi = 0°$ .Fig.11b shows the corresponding isotherms which are strongly influenced by the flow.Figs.11c and 11e show the projection of the velocity vectors on two vertical cross–sections($\phi = 2°$ and $\phi = 90°$) through the model.It is astonishing,how differently the velocity distribution in these two vertical planes behaves. In the plane $\phi = 2°$ it is quite asymmetric while in the plane $\phi = 90°$ it is almost symmetric.The corresponding isotherms are shown in Fig. 11d and Fig.11f.

Figs.12a and 12b show the temperature distribution along the circles $r = 0.9cm$, $0° \leq \phi \leq 360°$, $0.075cm$ beneath the solid–liquid interface,for $t = 200s$(the flow is symmetric) and $t = 450s$ (the flow is asymmetric).

Finally,Fig.13 shows the time-dependence of the temperature T at two points on two nearly perpendicular vertical planes,for $\phi = 2°$ and $\phi = 90°$,and for $r = 0.9cm$, $0.075cm$ below the solid–liquid interface.In the time interval $0s - 200s$ the temperature is constant at both points, whereas for $t \geq 200s$ (flow is unstable) the temperature increases and shows irregular oscillations.

From our numerical results it is clear that the buoyancy driven convection is highly unstable for all nearly real growing conditions,(see also /68/).Consequently,an asymmetric and oscillating temperature distribution is to be expected in real Czochralski crystal growth ,which then might have some undesirable consequences for the growing crystal.This situation will also not change in the case of moderate crystal and/or crucible rotation which one usually uses in practice.Even higher rotation rates of the crucible can, indeed,help to symmetrize the flow and the temperature field,but they are not able to prevent the temperature oscillations /42/.Moreover,**our simulations have shown that crystal rotation rates up to $30rpm$ (crucible at rest) are not sufficient to symmetrize the flow and the temperature field,not even in the vicinity of the solid–liquid interface.**

The possible remedy for this situation could be in using strong magnetic fields which are able to maintain the symmetry of the flow and temperature distribution/59/.

It is also important to stress that the instability of the buoyancy driven convection has recently been confirmed experimentally by direct observation in the Czochralski growth of a Si–crystal/73/.

7.3 The Application of External Magnetic Fields in the Czochralski Crystal Growth.

In this section we consider the application of a magnetic field in Czochralski crystal growth of an electrically conducting melt(Si–melt in our case) which recently has become a well–known technique for improving crystal quality/48/–/52/. It has been found experimentally that a magnetic field can stabilize or even suppress the convection in the melt which, together with the decrease of thermal asymmetry in the vicinity of the growth interface reduces the growth of striations. Application of a magnetic field provides a means of controlling the oxygen concentration in silicon crystals /48/,/49/.

Magnetic fields with different orientations have been used so far in the experiments:axial–/50/,/51/,stationary transverse–/52/,/74/,rotating transverse–/48/,/49/ and configured magnetic field /75/.

The numerical simulation in this field began with the pioneering work by **Langlois and Walker** /53/,followed by **Langlois and Lee** /54/,Lee,**Langlois and Kim**/55/, **Oreper and Szekely** /56/,/57/,**Mihelcic and Wingerath**/58/, /59/,and **Organ** /60/.However,in all these cases except for /58/, the mathematical model was either rotationally symmetric or two dimensional.

The aim of our investigation is to show the quantitative difference between the influence of a stationary transverse– and vertical magnetic field on the flow and temperature distribution in a three–dimensional mathematical model of the Czochralski crystal growth from a Si–melt.The flow and temperature are forced to be asymmetric through the asymmetric temperature boundary condition at the crucible wall.

This investigation is motivated by the growing interest in the application of externally imposed magnetic fields of different orientation as well as by the unsettled question which field could probably be the best for the application in Czochralski crystal growth.

7.3.1 Mathematical Model and Boundary Conditions.

Besides the general considerations given in the previous section about the externally applied magnetic fields,some additional demands on the mathematical model and boundary conditions exist.

The equations governing the time–dependent incompressible viscous flow in the crucible

including electrodynamic effects are the continuity equation

$$\nabla \cdot \vec{u} = 0. \tag{99}$$

and the Navier–Stokes equations with Boussinesq approximation and **Lorentz** force

$$(\vec{u})_t = -\nabla \cdot (\vec{u}\vec{u}) - \nabla p - \nu \nabla \times (\nabla \times \vec{u}) - \beta \bar{T} \vec{g} + \rho^{-1} \vec{j} \times \vec{B}, \tag{100}$$

where the last term on the r.h.s. is the Lorentz force term,with ρ the melt density, $\vec{j}$ the current density,and $\vec{B}$ the vector of the magnetic field.We need also the convective heat equation (without **Joule** heating).

$$(T)_t = -\nabla \cdot (\vec{u}T) + \alpha \nabla^2 T, \tag{101}$$

which is identical with eq.(83)in Sec.5.2.

The next equation we need is **Ohm's** law

$$\vec{j} = \sigma(\vec{E} + \vec{u} \times \vec{B}), \tag{102}$$

where σ is the coefficient of electrical conductivity and $\vec{E}$ the vector of the electrical field. In the case of a constant external magnetic field $\vec{B}_0$ ($\partial \vec{B}_0 / \partial t = 0$) and small magnetic **Reynolds** number $R_m = 4\pi\bar{\mu}\sigma LV$,where L and V denote the scale of length and velocity and $\bar{\mu}$ is the magnetic permeability,equation (102) reduces to

$$\vec{j} = \sigma(\nabla \Phi + \vec{u} \times \vec{B}_0), \tag{103}$$

where Φ denotes the electrical potential.Moreover,the total magnetic field $\vec{B}$ in the melt is equal(in this approximation) to the external magnetic field $\vec{B}_0$.

The unknown potential Φ can be found from the condition

$$\nabla \cdot \vec{j} = 0. \tag{104}$$

Equations (99)–(101),(103) and (104) are the governing equations of the mathematical model.

The Lorentz force term in (100) is obviously different for transverse–and vertical magnetic fields,respectively.It reads for:

(a) Transverse magnetic field $\vec{B}_0 = B_0(\vec{i}_r \cos\phi - \vec{i}_\phi \sin\phi)$,

$$F_r = -(\sigma B_0/\rho) \cdot ((\Phi)_z \sin\phi + B_0 \cdot (u \sin^2\phi + (v/2) \cdot \sin 2\phi)), \tag{105}$$

$$F_\phi = -(\sigma B_0/\rho) \cdot ((\Phi)_z \cos\phi + B_0 \cdot ((u/2) \sin 2\phi + v \cdot \cos^2\phi)), \tag{106}$$

$$F_z = (\sigma B_0/\rho) \cdot ((\Phi)_r \sin\phi + (1/r) \cdot (\Phi)_\phi \cos\phi - B_0 w), \tag{107}$$

and for:

(b) Vertical magnetic field $\vec{B}_0 = B_0 \cdot \vec{i}_z$

$$F_r = (\sigma B_0/\rho) \cdot ((1/r) \cdot (\Phi)_\phi + B_0 \cdot u), \tag{108}$$

$$F_\phi = (\sigma B_0/\rho) \cdot ((\Phi)_r - B_0 \cdot v), \tag{109}$$

$$F_z = 0. \tag{110}$$

The mathematical model as defined previously will be completed if one defines the appropriate initial-and boundary conditions.The initial and boundary conditions for the radial u-, tangential v-and vertical velocity component w,as well as for the temperature T are the same as noted in Sec.5.2,where we now include the thermocapillary convection,Eqs.(89a),(89b). The asymmetric temperature boundary condition at the crucible wall is in this case

$$T_c(\phi) = T_s + 15^\circ + 1^\circ \cdot \cos\phi. \tag{111}$$

This boundary condition produces the asymmetry of the flow and the temperature distribution in the melt.It is then interesting to find out which of the simulated magnetic fields better reduces this asymmetry at least in the vicinity of the solid-liquid interface.Finally,for the boundary condition of the current density $\vec{j}$,we assume that all boundaries in the model are electrically insulating(see also /60/).

7.3.2 Numerical Results.

The numerical simulations based on the mathematical model given in the previous section were performed with the geometrical and material (Si–melt) parameters given in Table 3.

Table 3

Crucible radius $R_c = 3.15cm$

Crystal radius $R_s = 1.20cm$

Melt depth $H = 3.60cm$

Crystal rotation rate $\Omega_s = 30rpm$

Crucible rotation rate $\Omega_c = 0rpm$

Solid–liquid interface temperature $T_s = 1693K$

Melt density $\rho = 2.33g/cm^3$

Kinematic viscosity $\nu = 0.0033cm^2/s$

Volumetric expansion coefficient $\beta = 0.000141/K$

Thermal diffusivity $\alpha = 0.125cm^2/s$

Electrical conductivity $\sigma = 0.0000125s/cm^2$ (in emu system)

Surface tension coefficient γ,$(\gamma)_T = -0.43dyn/(cm \cdot K)$

Dynamic viscosity $\mu = 0.01dyn\ s/cm^2$

Magnetic permeability $\bar{\mu} = 1$ (in emu system)

Discretization

$\delta r = 0.12cm$

$\delta z = 0.12cm$

$\delta\phi = 3^o$

Time step $\delta t \in [0.0001, 0.001]$

Here,our goal is to show which of the two applied magnetic fields,transverse or vertical,reduces better the asymmetry of the flow and temperature distribution in the vicinity of the growth interface.Because the crucible rotation brings temperature oscillations into the system /66/,we avoid to rotate the crucible. Instead,only the crystal rotation with $30rpm$, together with the buoyancy –and thermocapillary convection are present in the system,respectively.Also,in all simulated cases the flow and temperature field are plotted at the horizontal plane through the model,$0.06cm$ below the free surface.

Figs.14a,14b show the projection of the resultant flow and temperature distribution after $125s$ of real time and with no magnetic field applied. Both,the flow and temperature field are clearly asymmetric as a consequence of the asymmetric temperature boundary condition at the crucible wall.Also, the flow is clearly dominated by thermal convections.Typical for three-dimensional flow are wells and sinks of the flow at the horizontal plane slightly below the free surface.The maximum velocity is about $2.1cm/s$.

This state of the system serves as initial state for all subsequent simulated cases.In the next run we apply at time $t > 125s$ a transverse magnetic field of $B_0 = 1000G$. The direction of the field is from $\phi = 180°$ to $\phi = 0°$.Figs.15a,15b show the resultant flow and temperature distribution at $t = 300s$.The field clearly exerts a variable damping of the velocity vectors depending on the direction of these vectors.The consequence is that the magnetic field forces the flow parallel to the directon of the field.Also,the intensity of the maximum velocity vector is only moderately damped ($v_{max} = 1.2cm/s$).

For this reason it seems to us that,at least from the aspect of decreasing the thermal asymmetry,the transverse magnetic field is not advantageous for Czochralski crystal growth.This can also be verified in Fig.15b,where the isotherms especially in the vicinity of the growth interface are considerably squeezed perpendicular to the direction of the magnetic field.This striking effect will only slightly be changed if the applied field is stronger.Figs.16a,16b show the flow- and temperature fields influenced by a transverse magnetic field of $B_0 = 2000G$ at $t = 455s$. The field was switched on at $t = 305s$.The maximum velocity vector is again only weakly damped so that $v_{max} = 0.79cm/s$.

Next we apply a vertical magnetic field with $B_0 = 1000G$ at $t > 125s$ (given initial state).The important property of this field can be seen in Figs.17a,17b,namely,the field damps the velocity vectors independent of the directions of these vectors. Besides,the viscous boundary layer at the growth interface becomes apparently "thicker"so that the tangential component of the crystal rotation can clearly be seen.Also,damping of the velocity vectors is now higher,i.e.$v_{max} = 0.6cm/s$,than in the case of a transverse magnetic field.Also,the corresponding isotherms in Fig.17b are now quite symmetric.Figs.18a,18b show the influence of the vertical magnetic field of $B_0 = 2000G$ at $t = 480s$,which was switched on at $t = 305s$.The intensity of maximum velocity vectors is now only $0.16cm/s$.

A more detailed analysis of the influence of magnetic fields on the asymmetric temperature field in the vicinity of the growth interface is given in Figs.19a-19e.Here,the temperature is plotted on two circles round the vertical axis for radial distances $r = 0.42cm$(solid

line) and $r = 0.78cm$ (dashed line) at the horizontal plane $0.6mm$ below the free surface.Fig.19a shows the temperature asymmetry in the case that no magnetic field is applied.Figs.19d,19e show the influence of the vertical magnetic fields of 1000G and 2000G,respectively.In this case the maximum temperature difference over the two lines is smaller than $0.2K$. On the contrary in the case of transverse magnetic fields (Figs.19b, 19c) this difference is $1.5K$ for the $1000G$ field and $0.9K$ for the $2000G$ field,respectively. These plots clearly show that the vertical magnetic fields smooth out the thermal asymmetry much better than the transverse fields.

Finally,Fig.20a shows the time dependence of the temperature in the time interval $0s \leq t \leq 480s$, at two points ,namely point(A) $r = 0.42cm, \phi = 90°, H - z = 0.06cm$ (solid line) and point(B) $r = 0.78cm, \phi = 90°, H - z = 0.06cm$ (dashed line). For $0s \leq t \leq 125s$ there is no influence of a magnetic field so that the temperature is oscillating in this interval.For $125s \leq t \leq 305s$ a vertical magnetic field with $B_0 = 1000G$ is switched on,with the consequence that the oscillations are damped out and the temperature difference between the two points becomes smaller.For $t \geq 305s$ a new vertical magnetic field with $B_0 = 2000G$ was applied.We see that the temperature difference between the two points farther decreases.

Fig.20b shows the same for the transverse magnetic fields.

A comment on the temperature oscillations shown in Figs.20a,20b is necessary here,since the existence of oscillations may be surprising in such a small-scale geometry.The time step we used in our simulations is from the interval $10^{-4}s \leq t \leq 10^{-3}s$ which guarantees not only the stability of the numerical method but also small changes in the velocity–,pressure–and temperature variables between two consecutive time-steps.In all our numerical experiments these changes remain of the same sign for very long sequences of consecutive time–steps.For this reason we are confirmed,that these oscillations are of physical nature in spite of a relatively small size geometry.

Oscillations of the temperature field are not surprising if one recalls both,the material properties of silicon(such as low kinematic viscosity and relatively large volumetric expansion– and thermal diffusivity coefficient) and the asymmetric temperature boundary condition at the crucible wall with an average temperature difference to the solid–liquid interface of $15K$.This leads to a very complicated flow pattern,which is dominated by asymmetric thermal convections.Near the solid–liquid interface the rotating flow due to crystal rotation interferes with these convections so that in this region we have the most

intensive oscillations in the system.

Besides,one should not overlook that at the free surface the flow rotates with the disk in an strongly asymmetrical temperature field which also contributes to the temperature oscillations.Finally, we stress the fact that such temperature oscillations for instance have been experimentally recorded in an Czochralski set up of the identical size and under similar conditions/66/.

Preliminary results on rotating transverse fields are shown in Figs.21a,21b.These figures show the time–dependence of the temperature in the time–interval $120s \leq t \leq 168s$ for two points (A):$r = 0.4cm, \phi = 90°, H - z = 0.06cm$(solid line) and (B):$r = 0.8cm, \phi = 90°, H - z = 0.06cm$ (dashed line) affected by the rotating transverse fields of $1000G$ and $2000G$,respectively. In Fig.21a the magnetic field of $1000G$ rotates with $20rpm$,whereas in Fig. 21b the magnetic field of $2000G$ rotates with $10rpm$.Both figures clearly show that in the case of the stronger magnetic field with smaller rotation rate the temperature oscillations are larger (Fig.21b) than in the case of the weaker magnetic field and larger rotation rate(Fig.21a). In both cases the temperature is plotted every second.

8.Conclusions

The crystal growth melts we have analysed so far are typical for metallic melts,alloys,and semiconductors like Ge,GaAs or Si, respectively .They are characterized by a relatively low kinematical viscosity, high thermal diffusivity and high volumetric expansion coefficient(Table 3). Thus,these melts are low Prandtl number–and high Grashof number fluids, which are predestinate to be unstable.We have,so far, demonstrated numerically some of these instabilities(see also /68/).However, our present results are still restricted to the study of flow and temperature fields which is only one aspect of Czochralski crystal growth.

The incorporation of material transport and segregation processes would require choosing at least a binary system with noncongruent crystallization,to fix a corresponding phase diagram and to add a material transport equation to the mathematical model. Although,formally,material– and heat transport equations are almost identical,the incorporation of the former equation leads to some difficulties in the definition of appropriate boundary conditions ,and more important, the solid–liquid interface cannot be assumed to constitute an isothermal boundary surface any longer.These questions will be analysed in the near future.

9. Optimizing Czochralski Crystal Growth.

In Czochralski crystal growth a planar solid–liquid interface with strongly axisymmetrical thermal–and concentration fields with small radial gradients and an appropriately shaped meniscus are required to generate high quality crystals.

With rotational symmetry established in the system, one can fully utilize the advantages of intensive crystal rotation which then generates the necessary forced convection for controling of mass transfer at the solid–liquid interface, and provides effective stirring of the melt to guarantee complete mixing of all crystal components.Without rotational symmetry crystal rotation will induce the growth of compositional striations parallel to the growth interface.

Very often rotational symmetry is tried to be reached by crucible rotation.Since a rotating fluid is subject to the constraints of the Taylor–Proudman theorem (Sec.3.2),this leads to nonuniform mixing in the melt due to cell formation.

Homogenizing of the melt by alternating acceleration and deceleration of rotational motion leads to undesirable growth transients and concomitant compositional striations.

With thermal convections alone it is difficult to control the homogeneity of heat– and mass transfer in time at the solid– liquid interface.Since the thermal convections in Czochralski crystal growth are generally very intensive and oscillating,the application of a magnetic field is desirable to damp the velocity vectors and to smooth out the oscillations.On the other hand,if convections(forced and thermal) would come to rest completely,due to the influence of an excessively strong magnetic field,undesirable changes in the morphological stability of the planar growth interface may be the consequence.Thus,the optimum conditions for Czochralski crystal growth can be established by:

(1)controlling and maintaining rotational thermal symmetry,

(2)applying axial magnetic fields of about $0.5 Tesla$,

(3) rotating the crystal with about $60 rpm$ to generate a strong forced convection at the solid–liquid interface.

Acknowledgement

The digital simulations have been performed on CRAY X–MP/22 and CRAY X–MP/416 of the Zentralinstitut für Angewandte Mathematik.

We thank Prof.F.Hossfeld for his excellent support.

Especially,we thank Dr.K.Mika for his interest in this work,valuable suggestions and for thorough reading of the manuscript.

References

/1/ J.C.Brice:The Growth of Crystals from Liquids,North–Holland, Amsterdam,1973.

/2/ H.J.Scheell:J.Crystal Growth 13/14(1972),p.560.

/3/ H.J.Scheell;E.O.Schulz–Dubois:J.Crystal Growth 8(1971),p.304.

/4/ E.O.Schulz–Dubois:J.Crystal Growth 12(1972),p.81.

/5/ R.Hide:Dynamics of Rotating Fluids,in:Rotating Fluids in Geophysics, Eds.P.H.Roberts;A.M.Soward,Academic Press,1978,p.1.

/6/ H.P.Greenspan:The Theory of Rotating Fluids,Cambridge University Press,1968.

/7/ D.W.Moore:Homogeneous Fluids in Rotation,in:Rotating Fluids in Geophysics, Eds.P.H.Roberts;A.M.Soward,Academic Press,1978,p.29.

/8/ D.J.Tritton:Physical Fluid Dynamics,Van Nostrand,1980.

/9/ S.Chandrasekhar:Hydrodynamic and Hydromagnetic Stability, Oxford University Press,1961.

/10/ L.N.Howard:Trans.of the ASME,J.Appl.Mech.30(1963),p.481.

/11/ E.R.Benton;A.Clark Jr.:Ann.Rev.Fluid Mech.6(1974),p. 257.

/12/ R.Hide;C.W.Titman:J.Fluid Mech.29(1967),p.39.

/13/ H.P.Greenspan;L.N.Howard:J.Fluid Mech. 17(1963),p.385.

/14/ H.Görtler:ZAMM 24(1944),p.210.

/15/ G.W.Morgan:Proc.Roy.Soc.A206(1951),p.108.

/16/ H.Oser:Arch.Rat.Mech.Anal.1(1957),p.81.

/17/ H.Oser:ZAMM 38(1958),p.386.

/18/ A.Reynolds:ZAMP 13(1962),p.460 and p.561.

/19/ K.D.Aldridge;A.Toomre:J.Fluid Mech.37(1969),p.307.

/20/ H.Görtler:ZAMM 23(1943),p.65.

/21/ G.Veronis:Ann.Rev.Fluid Mech. 2(1970),p.37.

/22/ D.J.Baker:J.Fluid Mech. 29(1967),p.165.

/23/ P.G.Drazin;W.H.Reid:Hydrodynamic Stability,Cambridge University Press,1981.

/24/ R.Hide;P.J.Mason;Adv.Physics 24(1975),p.47.

/25/ D.Fultz in:IUTAM Symp.on Rotat.Fluid Systems,La Jolla(1966),p.296

/26/ J.C.Brice;T.M.Bruton;O.F.Hill;P.A.C.Whiffin:J.Crystal Growth 24/25(1974),p.429.

/27/ P.A.C.Whiffin;T.M.Bruton;J.C.Brice:J.Crystal Growth 32(1976),p.205.

/28/ A.D.W.Jones:J.Crystal Growth 61(1983),p.235.

/29/ C.D.Brandle:J.Crystal Growth 57(1982),p.65..

/30/ W.E.Langlois:Appl.Math.Model.1(1977),p.196..

/31/ W.E.Langlois:J.Crystal Growth 42(1977),p.386.

/32/ W.E.Langlois:J.Crystal Growth 46(1979),p.743.

/33/ W.E.Langlois:J.Crystal Growth 48(1980),p.25.

/34/ W.E.Langlois:Physico Chem.Hydrodyn.2(1981),p.245.

/35/ W.E.Langlois:J.Crystal Growth 56(1982),p.15.

/36/ W.E.Langlois:J.Crystal Growth 63(1983),p.67.

/37/ N.Kobayashi:J.Crystal Growth 52(1981),p.425.

/38/ N.Kobayashi:Comput.Meth.Appl.Mech.Eng.23(1980),p.21.

/39/ N.Kobayashi:Heat Transfer in Czochralski Crystal Growth,in:Preparation and Properties of Solid State Materials,Ed.W.R.Wilcox,6(1981),p.119. Marcel Dekker,N.Y./Basel.

/40/ M.Mihelcic;C.Schröck-Pauli;K.Wingerath;H.Wenzl;W.Uelhoff;A.van der Hart:J.Crystal Growth 53(1981),p.337.

/41/ M.Mihelcic;C.Schröck-Pauli;K.Wingerath;H.Wenzl;W.Uelhoff;A.van der Hart:J.Crystal Growth 57(1982),p.300.

/42/ M.Mihelcic;K.Wingerath;Chr.Pirron: J.Crystal Growth 69(1984),p.473.

/43/ M.J.Crochet;P.J.Wouters;F.T.Geyling;A.S.Jordan:J.Crystal Growth 65(1983), p.153.

/44/ D.T.J.Hurle:J.Crystal Growth 65(1983),p.124.

/45/ R.Lamprecht;D.Schwabe;A.Scharmann;E.Schultheiss:J.Crystal Growth 65 (1983),p.143.

/46/ H.Kopetsch:Physico Chem.Hydrodyn.11(1989),p.357.

/47/ J.J.Derby;R.A.Brown:J.Crystal Growth 74(1986),p.605.

/48/ K.Hoshikawa;H.Kohda;H.Hirata;H.Nakanishi:Japan.J.Appl.Phys.19(1980),p.L33.

/49/ K.Hoshikawa;H.Hirata;H.Nakanishi;K.Ikuta:Control of Oxygen Concentration in CZ Silicon Growth,in:Proc.4th Intern.Symp. on Silicon Materials,Science and Technology,Volume on Semiconductor Silicon,Eds.H.R. Huff;R.Kriegler;Y.Takeishi (Electrochemical Society,1981),p.101.

/50/ K.M.Kim;G.H.Schwuttke;P.Smetana:IBM Tech. Disclosure Bull. 24(1981), p.3376.

/51/ K.Hoshikawa:Japan J.Appl.Phys. 21(1982),p.L545.

/52/ A.F.Witt;C.J.Herman;H.C.Gatos:J.Mater.Sci.5(1970),p.822.

/53/ W.E.Langlois;J.S.Walker:Czochralski Crystal Growth in an Axial Magnetic Field,in:Proc.2nd Intern. Conf. on Boundary and Interior Layers–Computational and Asymptotic Methods,Dublin,1982,Ed.J.J.H. Miller,(Boole,Dublin,1982),p.299.

/54/ W.E.Langlois;Ki–Jun Lee:J.Crystal Growth 62(1983),p.481.

/55/ Ki–Jun Lee;W.E.Langlois;K.M.Kim:Phys.Chem.Hydrodyn.5(1984),p.135.

/56/ G.M.Oreper;J.Szekely:J.Crystal Growth 64(1983),p.505.

/57/ G.M.Oreper;J.Szekely:J.Crystal Growth 67(1984),p.405.

/58/ M.Mihelcic;K.Wingerath:J.Crystal Growth 71(1985),p.163.

/59/ M.Mihelcic;K.Wingerath:J.Crystal Growth 82(1987),p.318.

/60/ A.E.Organ:J.Crystal Growth 73(1985),p.571.

/61/ J.E.Welch;F.H.Harlow;J.P.Shannon;B.J.Daly:Los Alamos Report LA–3425,1966.

/62/ A.J.Chorin:Math.Computation 22(1968),p.745.

/63/ C.W.Hirt;J.L.Cook:J.Comp.Phys. 10(1972),p.324.

/64/ Th.v.Karman:ZAMM 1(1921),p.233.

/65/ W.G.Cochran:Proc.Cambr.Phil.Soc. 30(1934),p.365.

/66/ W.Uelhoff;A.Fatah;G.Hanke;A.van der Hart;J.Docter;H.Wenzl; M.Mihelcic;C.Schröck–Pauli:Oszillatorische Konvektion–Workshop, Battelle–Institut e.V.,Frankfurt a.M.,March 1983,Ed.D.Langbein

/67/ A.Bottaro;A.Zebib:J.Crystal Growth 97(1989),p.50.

/68/ J.R.Ristorcelli;J.L.Lumley:J.Crystal Growth 116(1992),p.447.

/69/ W.E.Langlois:Ann.Rev.Fluid Mech.17(1985),p.191.

/70/ S.M.Pimputkar;S.Ostrach:J.Crystal Growth 55(1981),p.614.

/71/ M.Mihelcic;K.Wingerath:J.Crystal Growth 97(1989),p.42.

/72/ C.D.Brandle:J.Crystal Growth 57(1982),p.65.

/73/ K.Kakimoto;M.Eguchi;H.Watanabe;T.Hibiya:J.Crystal Growth 88(1988),p.365.

/74/ T.Suzuki;N.Isawa;Y.Okubo;K.Hoshi:CZ Silicon Crystal grown in a Transverse Magnetic Field,in:Proc.4th Intern.Symp.on Silicon Materials,Science and Technology,Volume on Semiconductor Silicon,Eds.H.R. Huff;R.Kriegler;Y.Takeishi (Electrochemical Society,1981),p.90.

/75/ N.Riley:J.Crystal Growth 97(1989),p.76.

Figure Captions

Fig.1: Transverse Taylor column (Taylor–Proudman cell) at $t \sim 190s$ in the CZ–Model in which the crucible rotates with constant angular velocity $\Omega_c = 15rpm$ and the disk is stationary, (Fig.1 top-left). Remaining figures show oscillations of the column due to periodically accelerating–and decelerating rotation of the crucible.It is interesting to note that changing of the crucible rotation rate in a given time period is not sufficient to eliminate the column from the melt.The plots are performed by means of a large number of massless particles or markers; their coordinates are computed after each time–step of simulation.

Fig.2: Relative velocities in the Ekman boundary layer on a plate which rotates with the angular velocity $\Omega_s = 30rpm$ and at the same time moves in the x–direction with a constant speed U_0. Note that at $z = \pi\sqrt{2\nu/\Omega_s}$ the flow is reversed $(U/U_0 < 0)$ as the consequence of the plate's rotation.

Fig.3: Flow between rotating coaxial infinite disks.

Fig.4: Geometry of the CZ–Mathematical Model.

Fig.5: (See Fig.5)

Fig.6a: Cochran flow. Comparison of analytical solution of Cochran flow by von Karman (functions F, G, H) with the numerical solution $(\hat{F}, \hat{G}, \hat{H})$.The geometry of the CZ–Model is:$R_s = 1.2cm$,$R_c = 3cm$ and $H = 4cm$.Disk rotates with $\Omega_s = 10rpm$.The solutions are compared at the vertical profile $r = 0.02cm$.

Fig.6b: Cochran flow. $\Omega_s = 10rpm$,$r = 0.58cm$.See Fig.6a.

Fig.6c: Cochran flow. $\Omega_s = 10rpm$,$r = 1.19cm$.See Fig.6a.

Fig.7a: Cochran flow. $\Omega_s = 50rpm$,$r = 0.02cm$.See Fig.6a.

Fig.7b: Cochran flow. $\Omega_s = 50rpm$,$r = 0.58cm$.See Fig.6a.

Fig.7c: Cochran flow. $\Omega_s = 50rpm$,$r = 1.19cm$.See Fig.6a.

Fig.8a: Forced oscillations. Streamlines of the flow due to forced oscillations of the disk in CZ–Model .Geometry of the model is given by:$R_c = 5cm$, $R_s = 1cm$ and $H = 10cm$.Angular velocity of the crucible is $\Omega_c = 40rpm$ and the amplitude of the disk's oscillation is $A = 0.5cm/s$.Figs.8a–8d show the state of the system for one period of oscillations at $t = (2061 + n/4)s$,$n = 1, 2, 3, 4$, respectively.Note the change in the sense of vortices'rotation in Figs.8a,8c and Figs.8b,8d.

Fig.8b: Forced oscillations. See Fig.8a.

Fig.8c: Forced oscillations. See Fig.8a.

Fig.8d: Forced oscillations. See Fig.8a.

Fig.9a: Baroclinic instability.Projection of the flow field on the horizontal plane $0.035cm$ below the free surface of the CZ–Model,at $t \sim 225s$.Note that for given parameters $F = 1.3 \cdot 10^8, \Theta = 0.032(\delta T_c = 15°)$ the flow and the corresponding temperature field (Fig.9b) are perfectly symmetric.Geometry of CZ–Model is given by:$R_c = 3.15cm$, $R_s = 1.2cm$ and $H = 4cm$.Crystal rotates with $\Omega_s = 80rpm$.

Fig.9b: Baroclinic instability. To Fig.9a corresponding temperature field.

Fig.10a: Baroclinic instability.Projection of the flow field on the horizontal plane $z = 3.965cm$ through the CZ–Model at $t = 288.5s$. Note that for the new parameter $\Theta = 0.053(\delta T_c = 25°)$ (F unchanged) the flow and the corresponding temperature field (Fig.10b) are now completely asymmetric.

Fig.10b:

Fig.10c: Baroclinic instability.Projection of the flow field on the horizontal plane $z = 1.920cm$ through the CZ–Model.

Fig.10d: Baroclinic instability.To Fig.10c corresponding temperature field.

Fig.10e: Baroclinic instability.Projection of the flow field on the horizontal plane $z = 0.035cm$ through the CZ–Model.

Fig.10f: Baroclinic instability.To Fig.10e corresponding temperature field.

Fig.11a Instability of the buoyancy driven convection.Projection of the flow field on the horizontal plane $0.075cm$ below the free surface,at $t = 290s$.Geometry of the CZ–Model is given by: $R_c = 3cm, R_s = 1.5cm, H = 6cm$.Temperature difference $\delta T = 5K$.

Fig.11b: Instability of the buoyancy driven convection. To Fig.11a corresponding temperature field.

Fig.11c Instability of the buoyancy driven convection.Projection of the flow field on the vertical plane $\phi = 2°$,at $t = 280s$.

Fig.11d: Instability of the buoyancy driven convection. To Fig.11c corresponding temperature field.

Fig.11e Instability of the buoyancy driven convection.Projection of the flow field on the vertical plane $\phi = 90°$,at $t = 280s$. Note that the flow is almost symmetric.

Fig.11f: Instability of the buoyancy driven convection. To Fig.11e corresponding temperature field.Note that the temperature field is almost symmetric.

Fig.12a: Instability of the buoyancy driven convection. Temperature distribution on the horizontal line $r = 0.9cm$,$0^\circ \leq \phi < 360^\circ$,0.075cm below the solid–liquid interface ,at $t = 200s$. The temperature distribution is still symmetric.

Fig.12b: Instability of the buoyancy driven convection. The same temperature distribution as in Fig.12a,but at time $t = 450s$. The temperature distribution is now asymmetric.

Fig.13: Instability of the buoyancy driven convection. Time–dependence of the temperature at two points on two vertical planes for $r = 0.9cm, \phi = 2^\circ$(solid line) and $r = 0.9cm, \phi = 90^\circ$ (dashed line). Both points are $0.075cm$ below the solid–liquid interface.Note an irregular temperature development for $t > 200s$.

Fig.14a: Magnetic field. Projection of the flow field on the horizontal plane $0.06cm$ below the free surface,with **no magnetic field applied**. The maximum velocity in the CZ–Model is about $2.1cm/s$.

Fig.14b: Magnetic field. To Fig.14a corresponding temperature field. The temperature field is asymmetric due to asymmetric temperature boundary condition at the crucible wall.

Fig.15a: Magnetic field. Influence of the **transverse magnetic field** of $B_0 = 1000G$ on the flow. Projection of the flow field on the horizontal plane $0.06cm$ below the free surface is shown.The direction of the magnetic field is from $\phi = 180^\circ$ to $\phi = 0^\circ$.The maximum velocity in CZ–Model is now $1.2cm/s$.

Fig.15b: Magnetic field. To Fig.15a corresponding temperature field.Note that isotherms are squeezed in the direction of the magnetic field even in the vicinity of the solid–liquid interface.

Fig.16a: Magnetic field. Influence of the **transverse magnetic field** of $B_0 = 2000G$ on the flow. Projection of the flow field on the horizontal plane $0.06cm$ below the free surface is shown.The direction of the magnetic field is from $\phi = 180^\circ$ to $\phi = 0^\circ$.The maximum velocity in CZ–Model is now $0.79cm/s$.

Fig.16b: Magnetic field. To Fig.16a corresponding temperature field.Note that isotherms are squeezed in the direction of the magnetic field even in the vicinity of the solid–liquid interface.

Fig.17a: Magnetic field. Influence of the **vertical magnetic field** of $B_0 = 1000G$ on the flow.

Projection of the flow field on the horizontal plane $0.06cm$ below the free surface is shown. The maximum velocity in CZ–Model is now $0.6cm/s$.

Fig.17b: Magnetic field. To Fig.17a corresponding temperature field.Note that isotherms are in this case almost symmetric at least in the vicinity of the solid–liquid interface.

Fig.18a: Magnetic field. Influence of the **vertical magnetic field** of $B_0 = 2000G$ on the flow. Projection of the flow field on the horizontal plane $0.06cm$ below the free surface is shown. The maximum velocity in CZ–Model is now $0.16cm/s$.

Fig.18b: Magnetic field. To Fig.18a corresponding temperature field.Note that isotherms are in this case almost symmetric at least in the vicinity of the solid–liquid interface.

Fig.19a: Magnetic field. Temperature distribution at two horizontal lines round the vertical axis of the model,$0.06cm$ below the free surface: for $r = 0.42cm$ (solid line) and $r = 0.78cm$ (dashed line).**No magnetic field is applied.**

Fig.19b: Magnetic field. Temperature distribution at the same lines as in Fig.19a under the influence of a **transverse magnetic field of** $B_0 = 1000G$.

Fig.19c: Magnetic field. Temperature distribution at the same lines as in Fig.19a under the influence of a **transverse magnetic field of** $B_0 = 2000G$.

Fig.19d: Magnetic field. Temperature distribution at the same lines as in Fig.19a under the influence of a **vertical magnetic field of** $B_0 = 1000G$. Note the almost constant temperature difference between two lines.

Fig.19e: Magnetic field. Temperature distribution at the same lines as in Fig.19a under the influence of a **vertical magnetic field of** $B_0 = 2000G$. Note the almost constant temperature difference between two lines.

Fig.20a: Magnetic field. Time–dependence of the temperature at two points:(a)$r = 0.42cm$ (solid–line),and (b) $r = 0.78cm$(dashed line), ($\phi = 90°$,$H - z = 0.06cm$ for both points). In time interval $0s \leq t \leq 125s$ no magnetic field is applied.For $125s < t \leq 305s$ a **vertical magnetic field of** $B_0 = 1000G$ is applied.For $305s < t \leq 480s$ **vertical magnetic field of** $B_0 = 2000G$ is applied.

Fig.20b: Magnetic field. Time–dependence of the temperature at two points:(a)$r = 0.42cm$ (solid–line),and (b) $r = 0.78cm$(dashed line), ($\phi = 90°$,$H - z = 0.06cm$ for both points). In time interval $0s \leq t \leq 125s$ no magnetic field is applied.For $125s < t \leq 305s$ a **transverse magnetic field of** $B_0 = 1000G$ is applied.For $305s < t \leq 480s$ **transverse magnetic field of** $B_0 = 2000G$ is applied.

Fig.21a: Rotating magnetic field. Time–dependence of the temperature at two points:(a)$r = 0.42cm$ (solid–line),and (b) $r = 0.78cm$(dashed line), ($\phi = 90°, H - z = 0.06cm$ for both points). In time interval $122s \leq t \leq 168s$ a **rotating transverse magnetic field of** $B_0 = 1000G$ is applied. The field rotates with **20rpm**.

Fig.21b: Rotating magnetic field. Time–dependence of the temperature at two points:(a)$r = 0.42cm$ (solid–line),and (b) $r = 0.78cm$(dashed line), ($\phi = 90°, H - z = 0.06cm$ for both points). In time interval $122s \leq t \leq 168s$ a **rotating transverse magnetic field of** $B_0 = 2000G$ is applied. The field rotates with **10rpm**.Note the more intensive temperature oscillations in this case.

Fig. 1

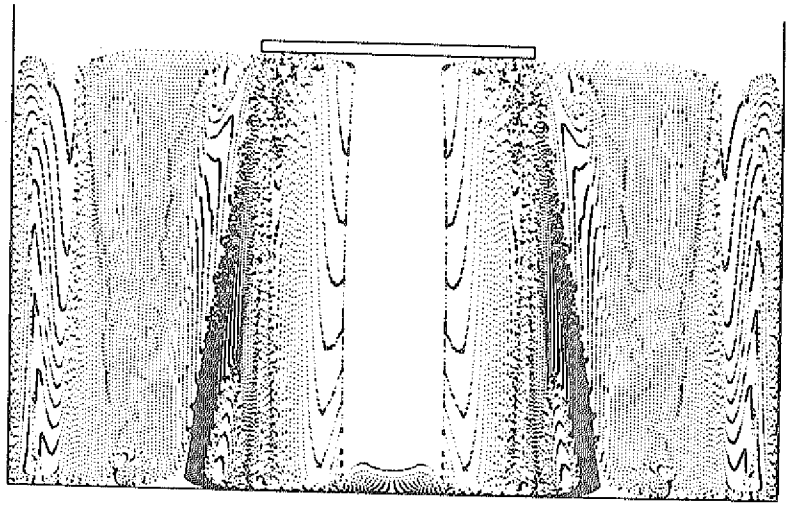

190.872

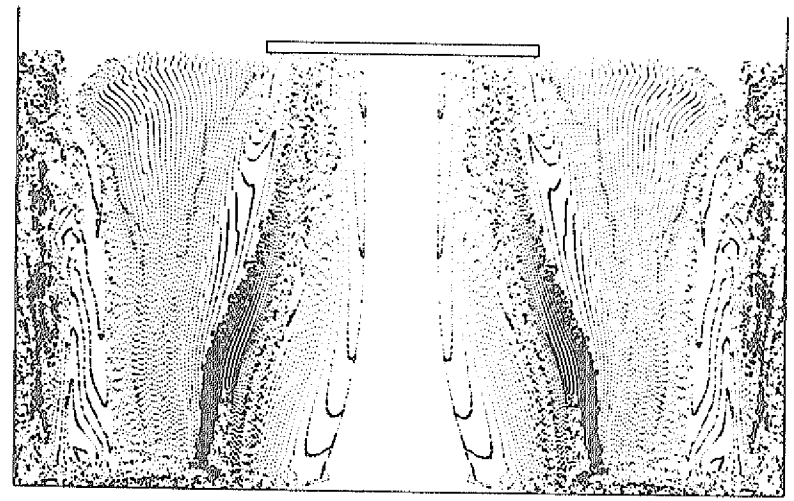

197.788

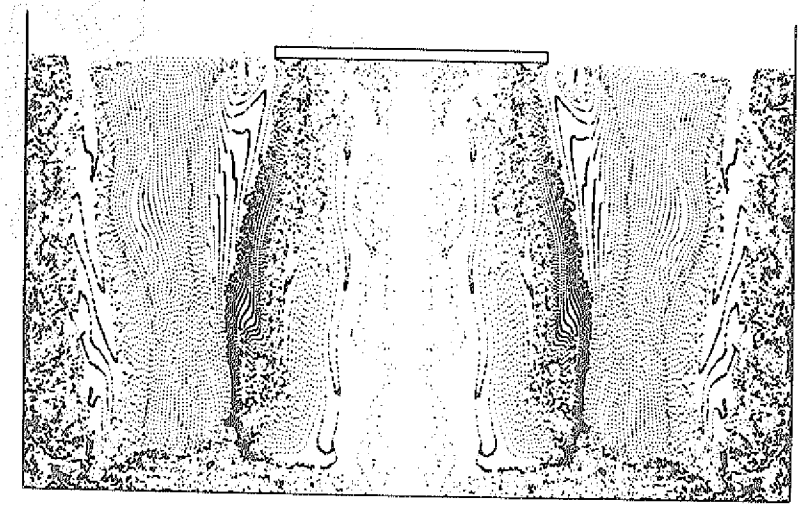

201.928

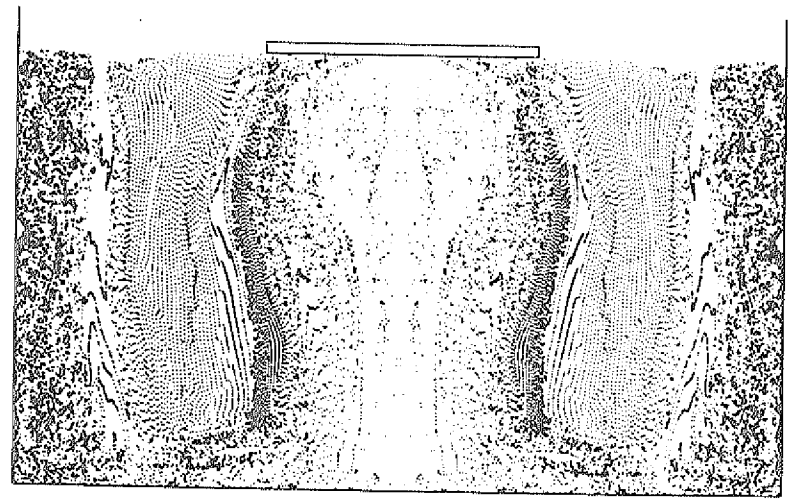

208.598

Fig.2

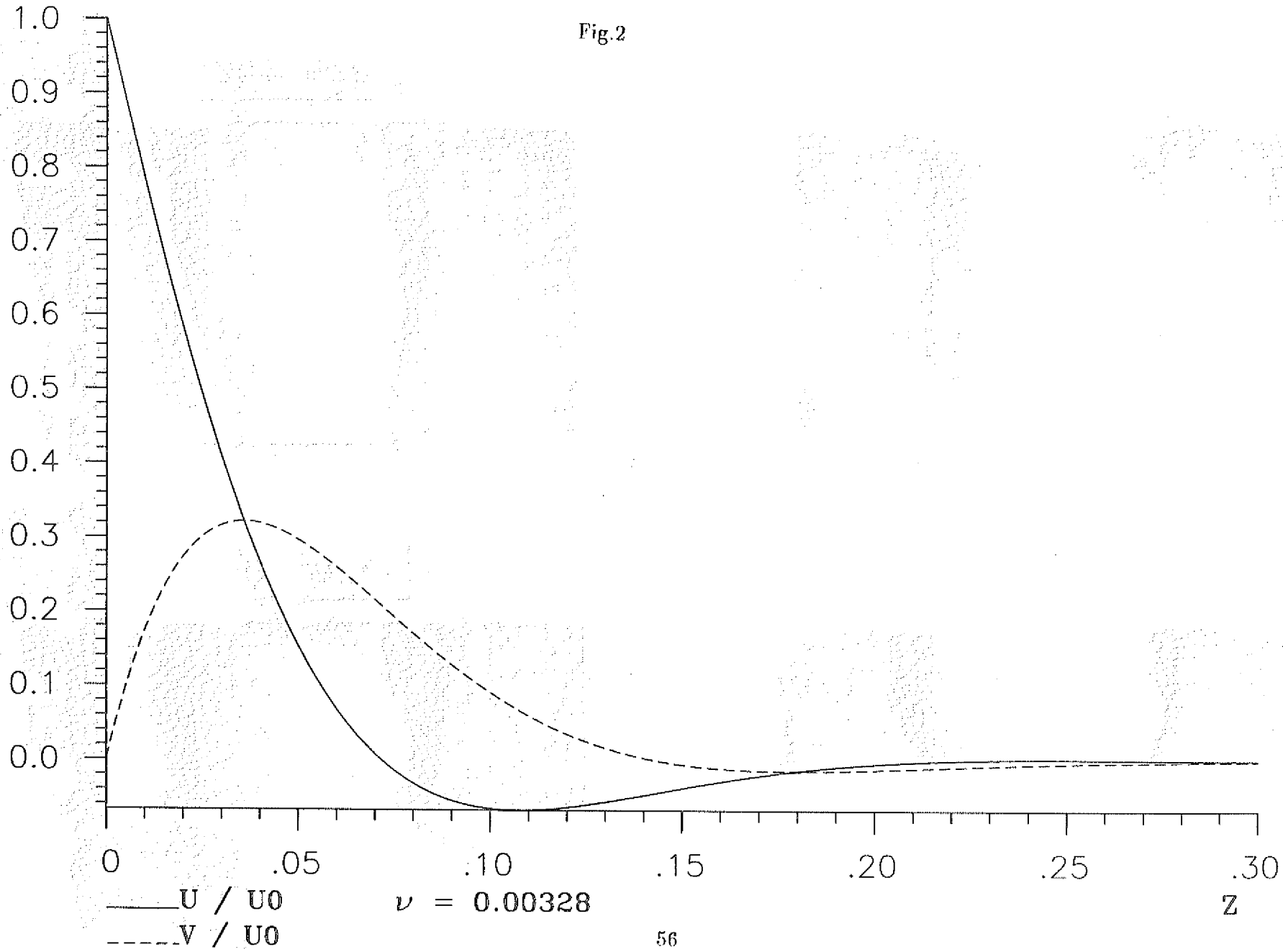

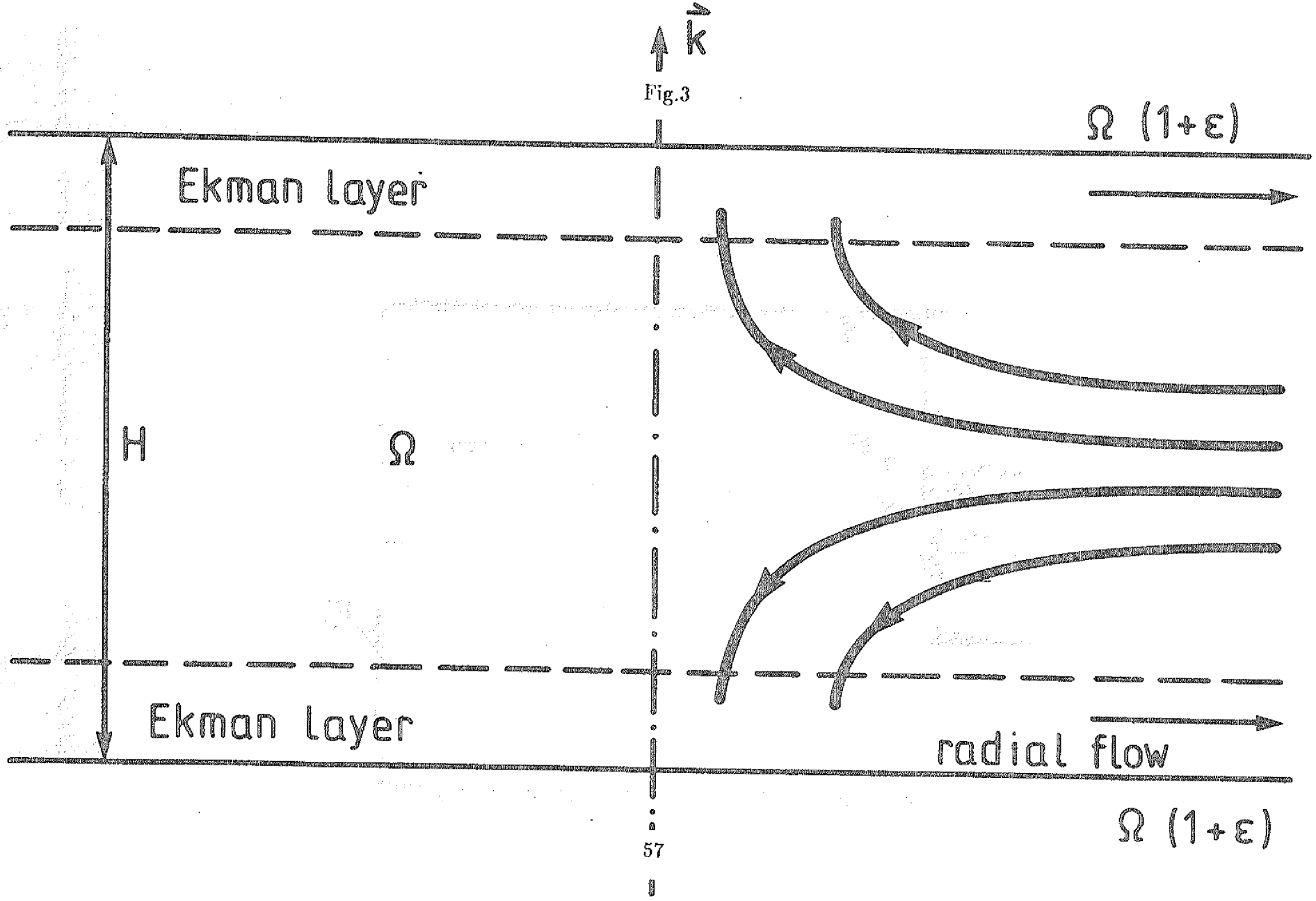

Fig.3

Fig.4

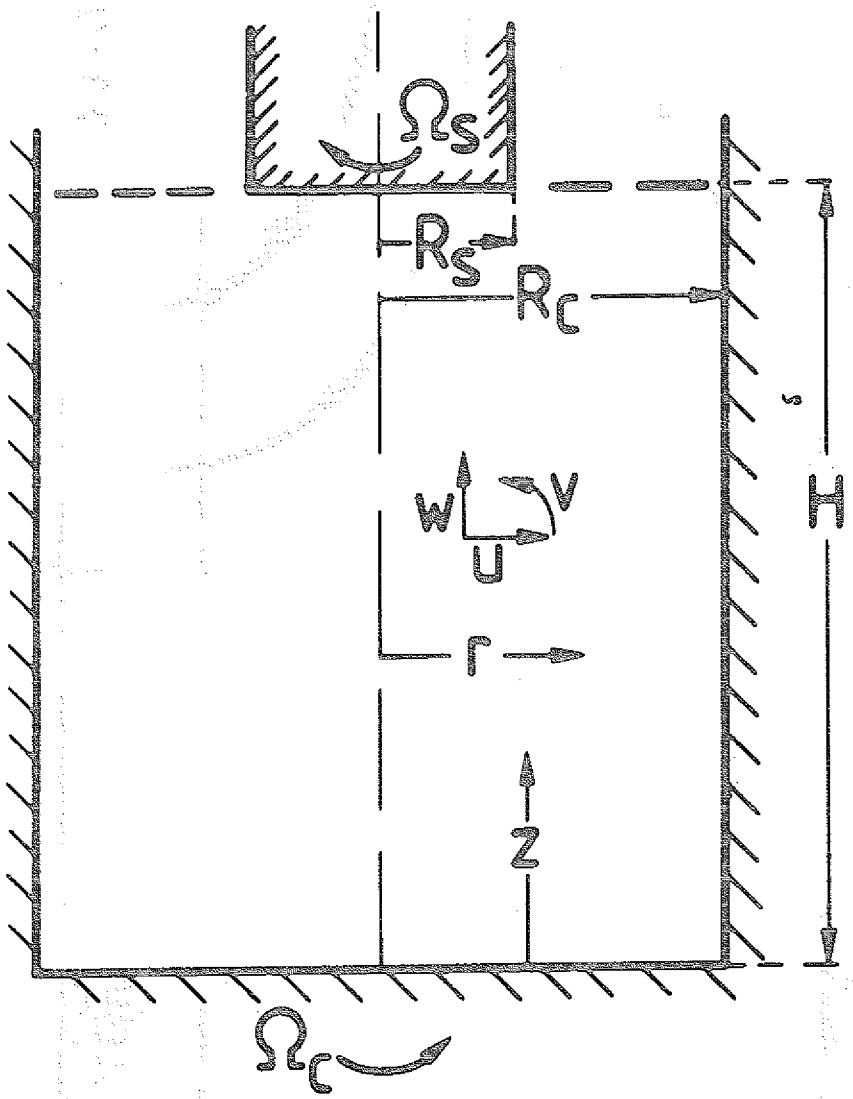

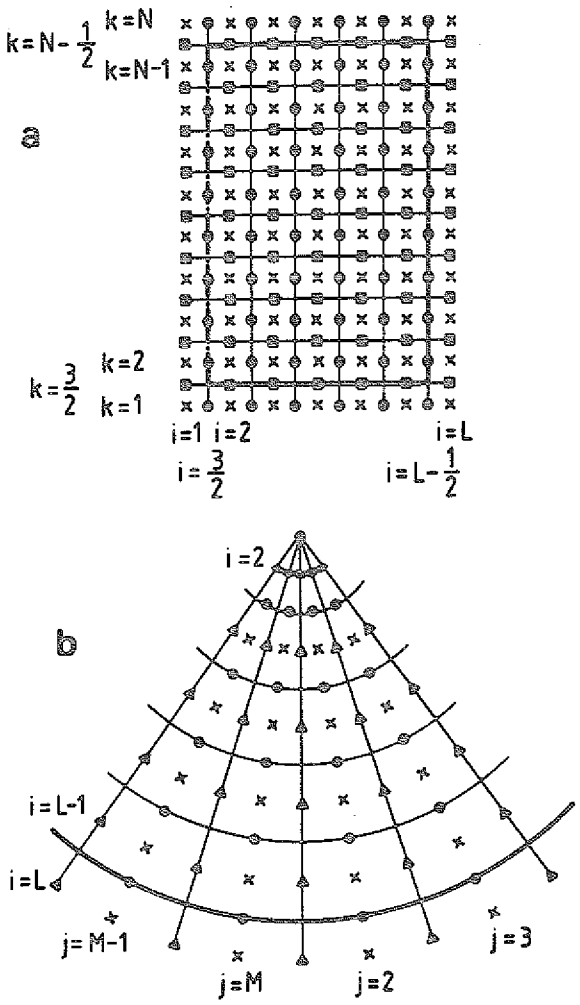

Fig. 14 Computational mesh in a vertical and horizontal cross-section: (×) pressure and temperature; (▲) azimuthal velocity points; (●) radial velocity points; (■) vertical velocity points. The broken line indicates the symmetry axis of the geometrical configuration; the heavy lines denote crucible walls and the free surface, respectively.

Fig.6a

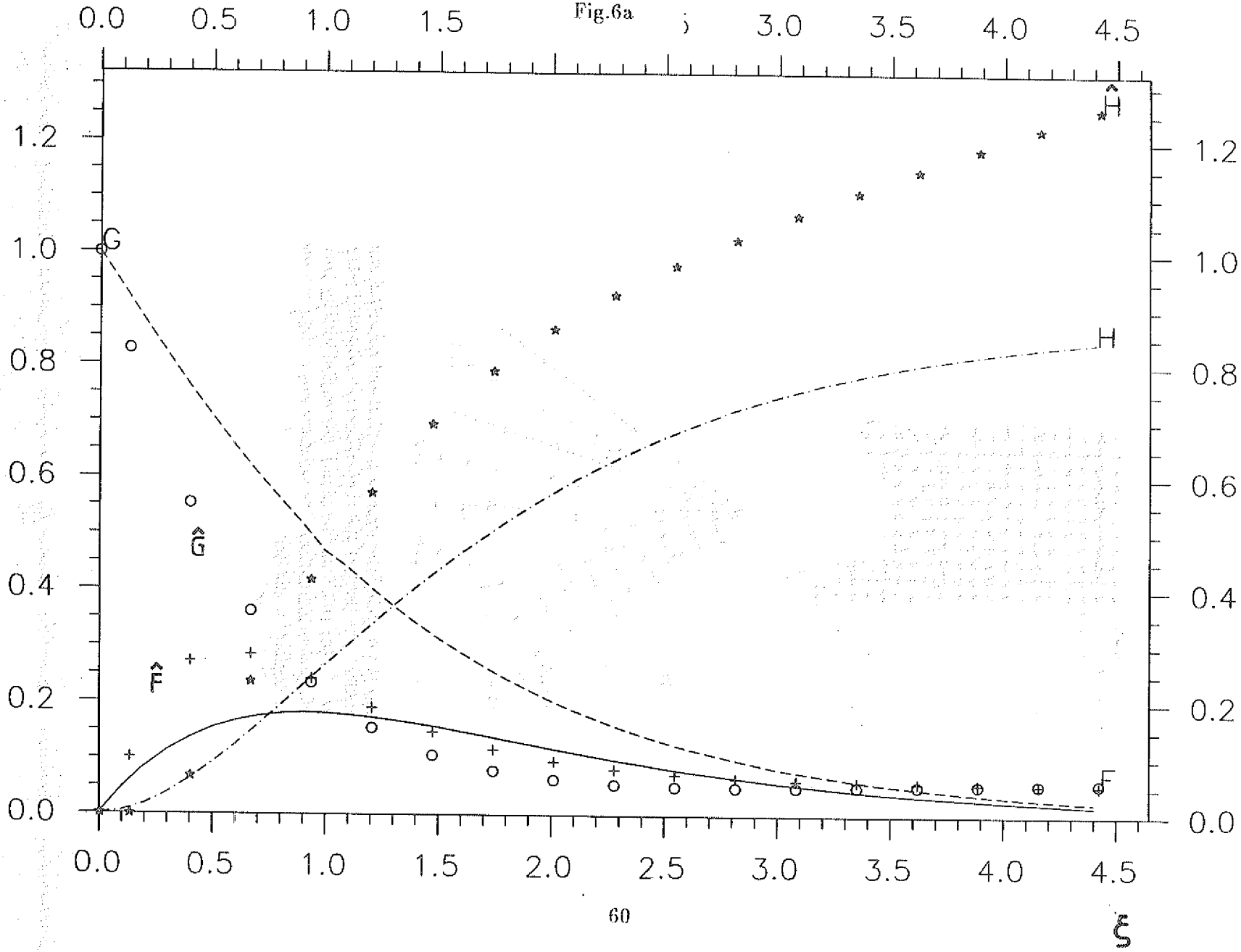

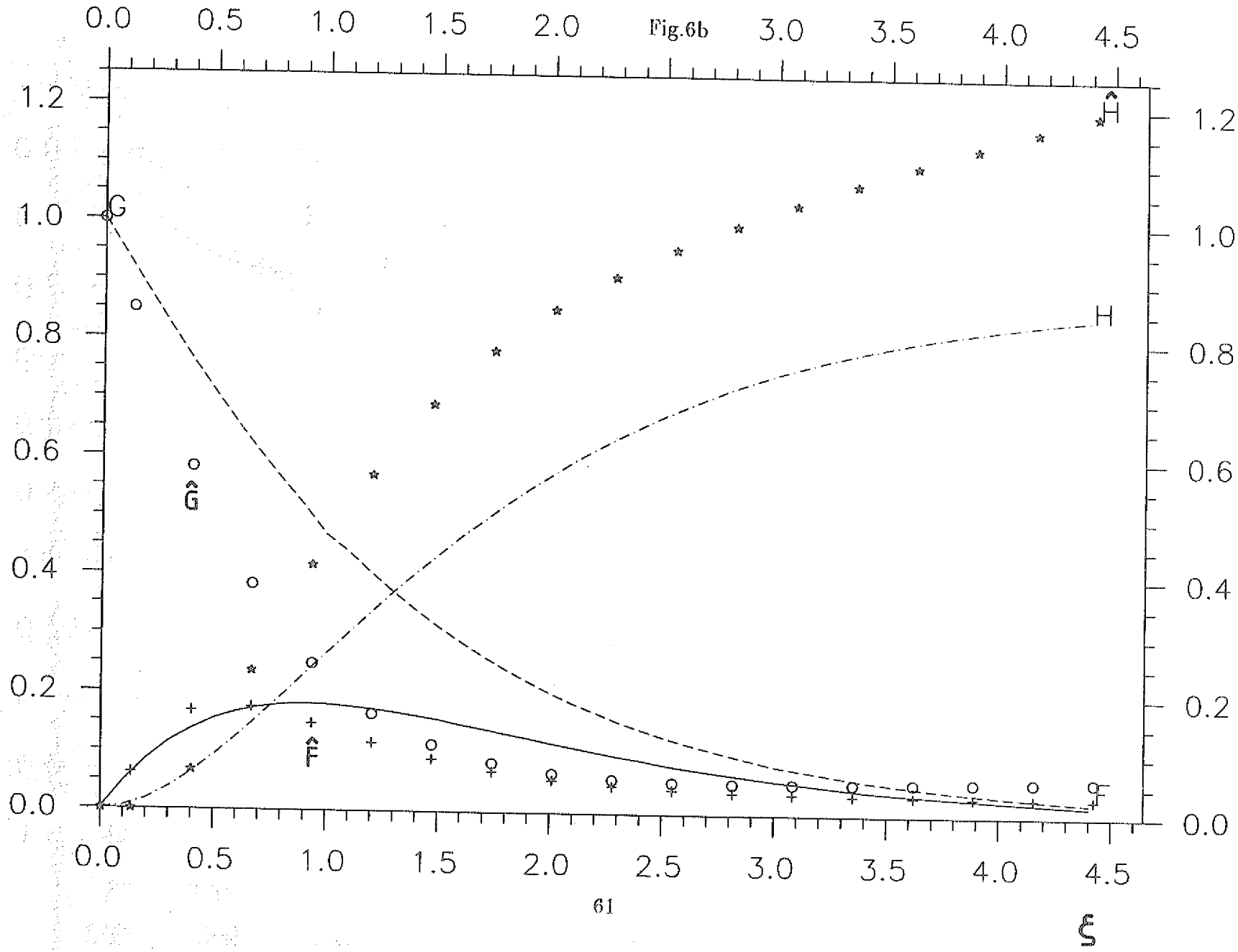

Fig.6b

Fig.6c

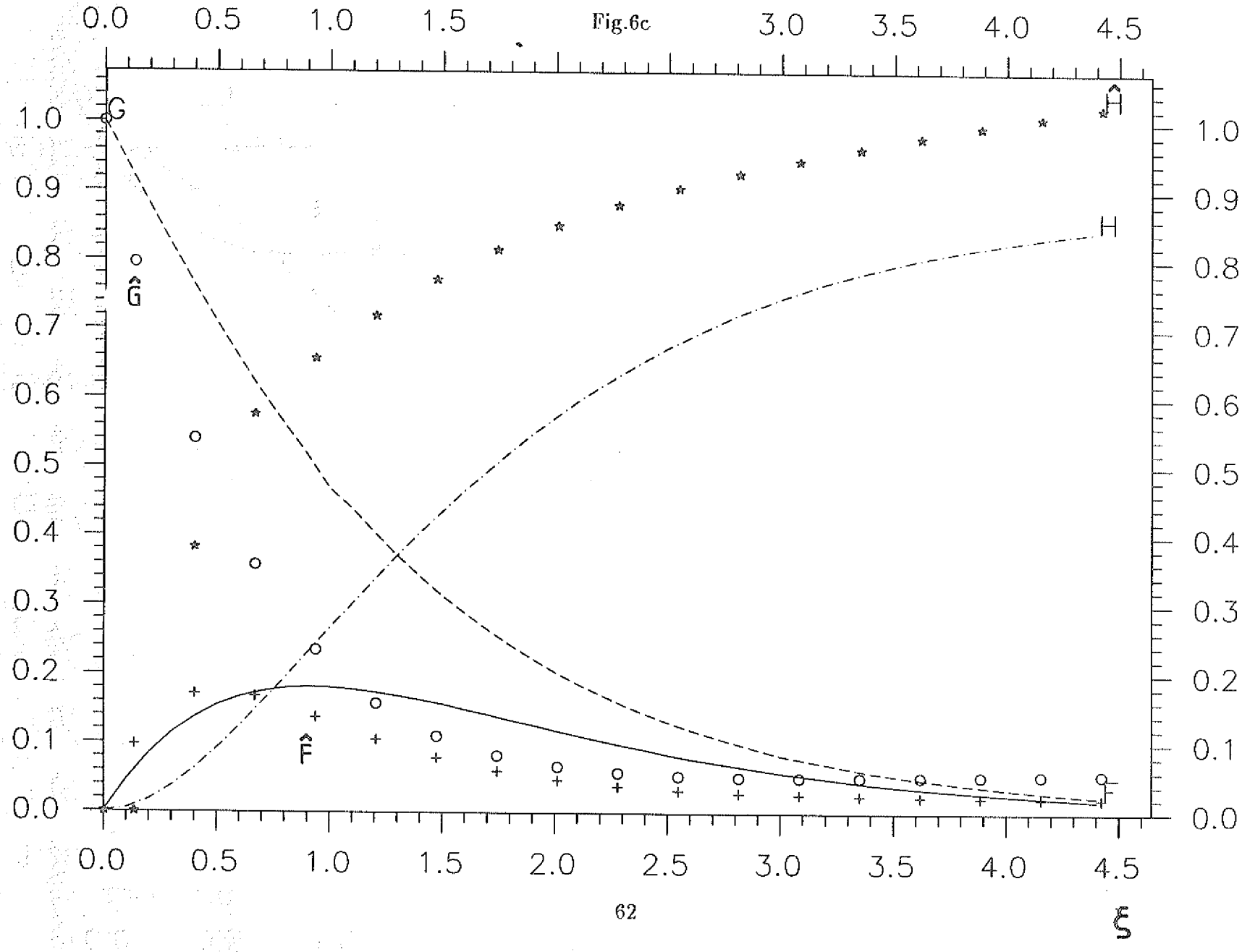

Fig.7a

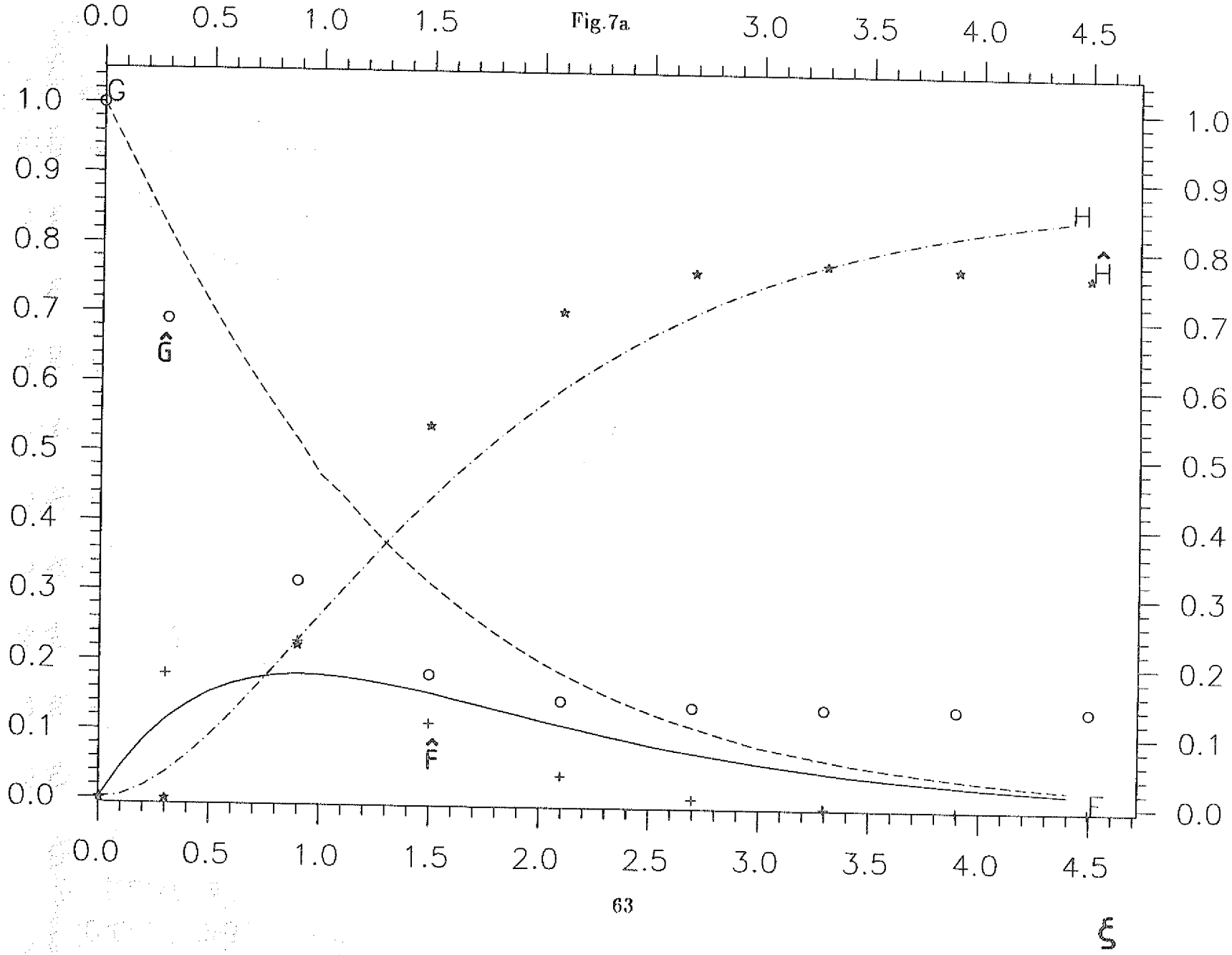

Fig.7b

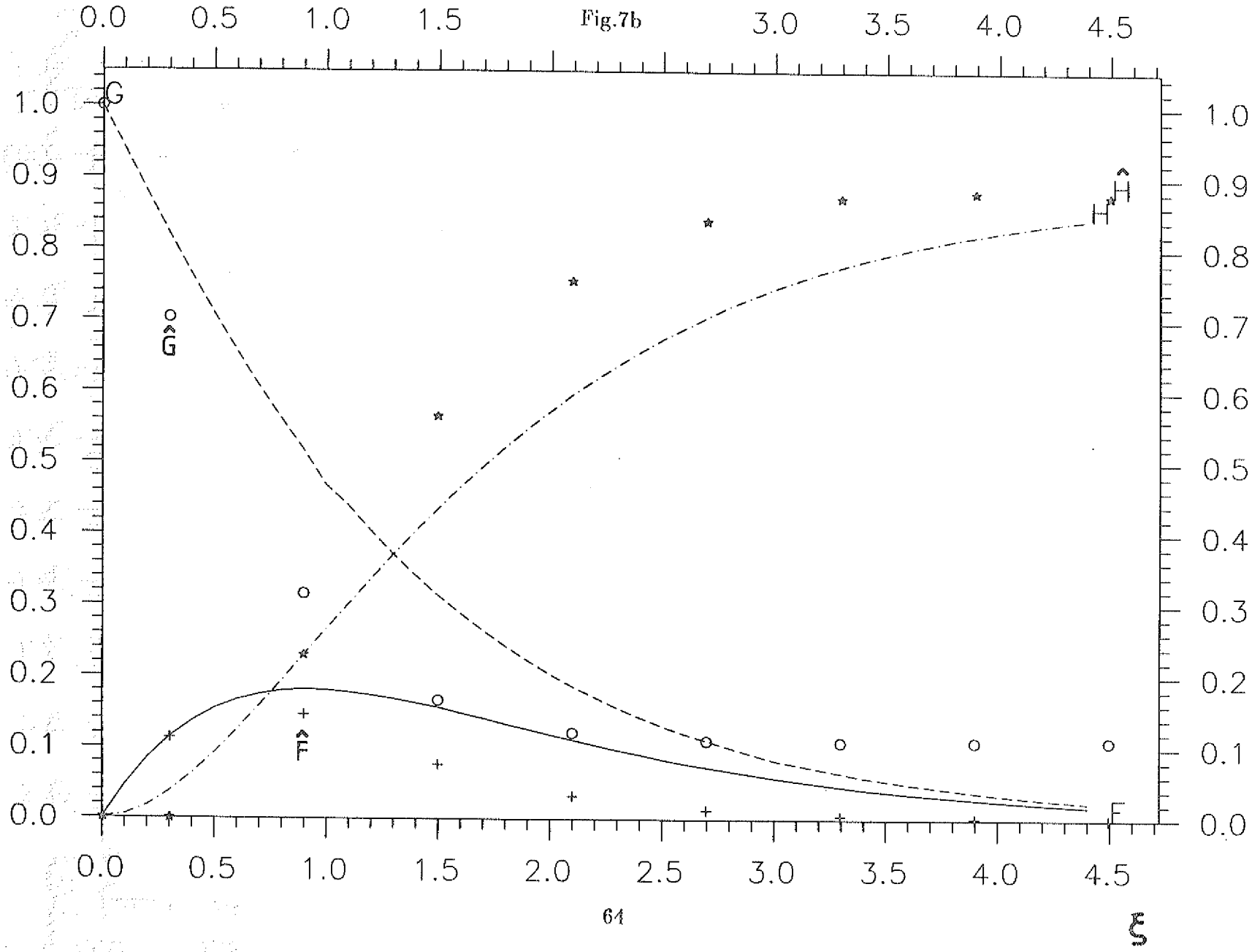

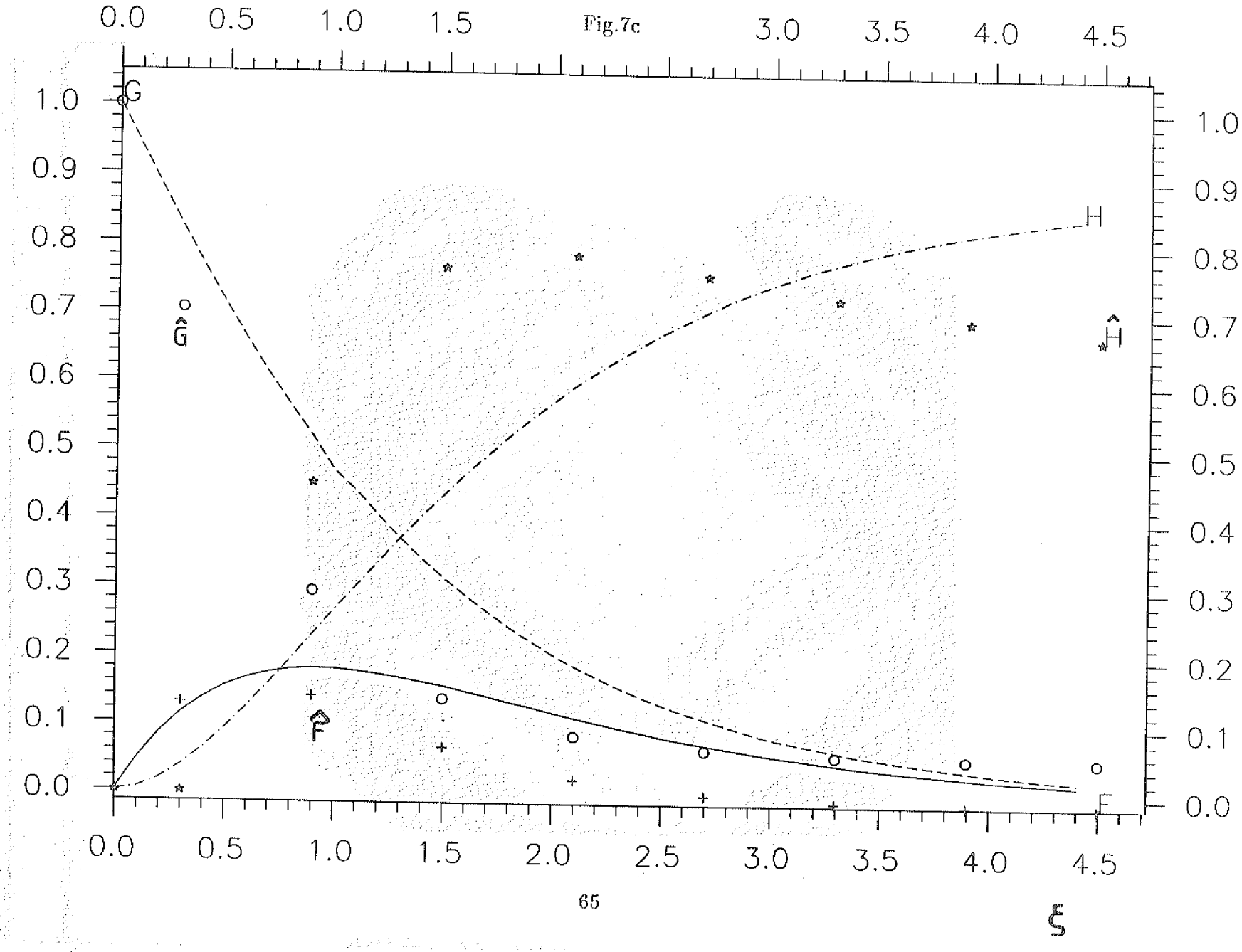

Fig.7c

STREAMLINES at t= 2061.50 s

Fig.8b

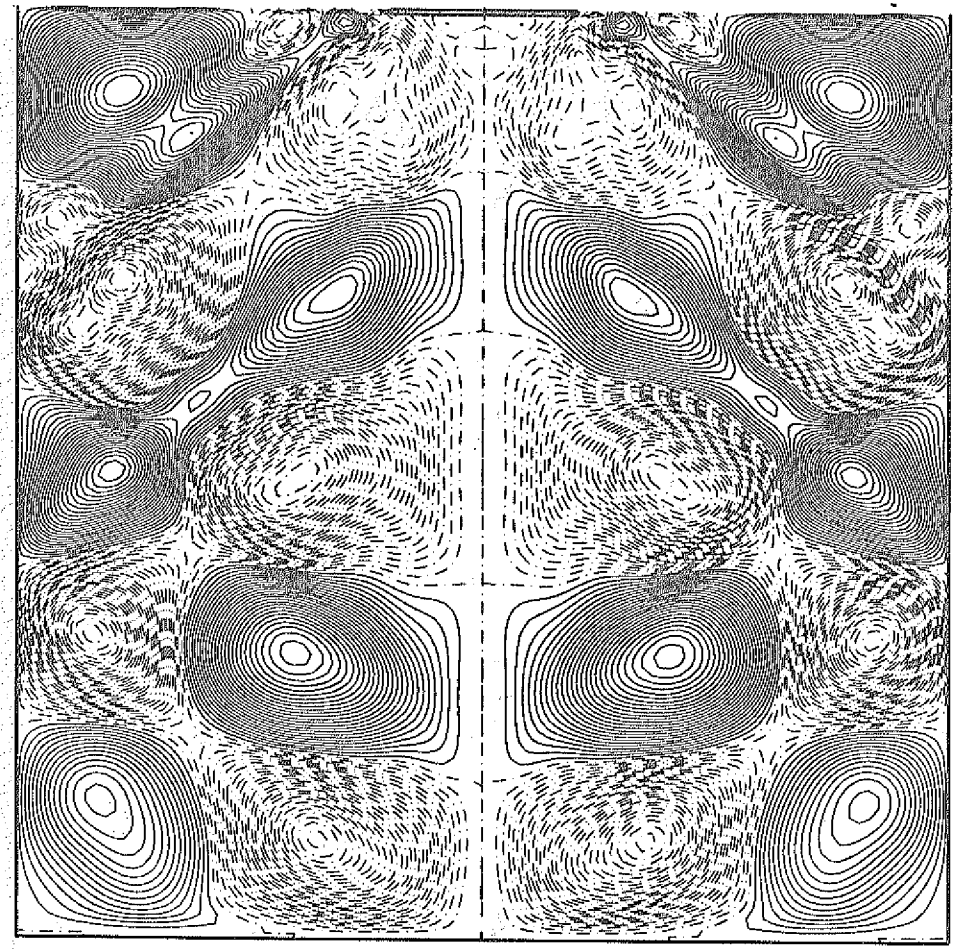

STREAMLINES at t= 2061.75 s

Fig.8c

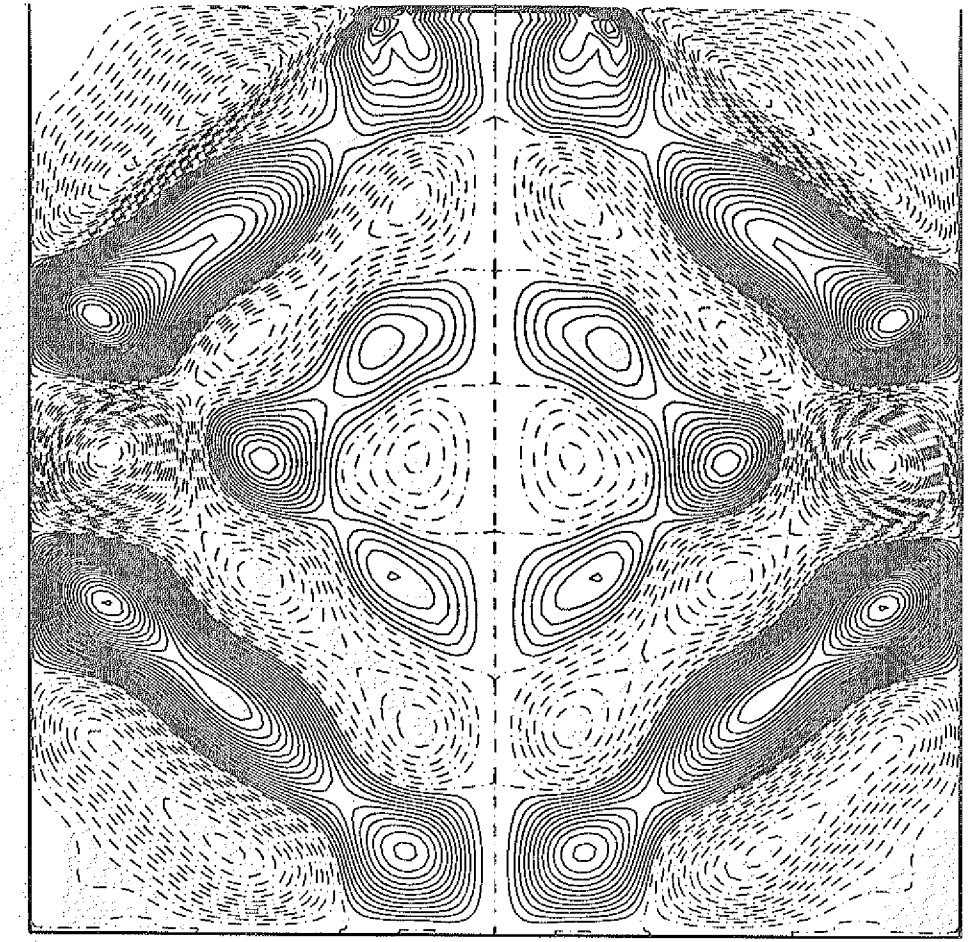

STREAMLINES at t= 2062.00 s

Fig.8d

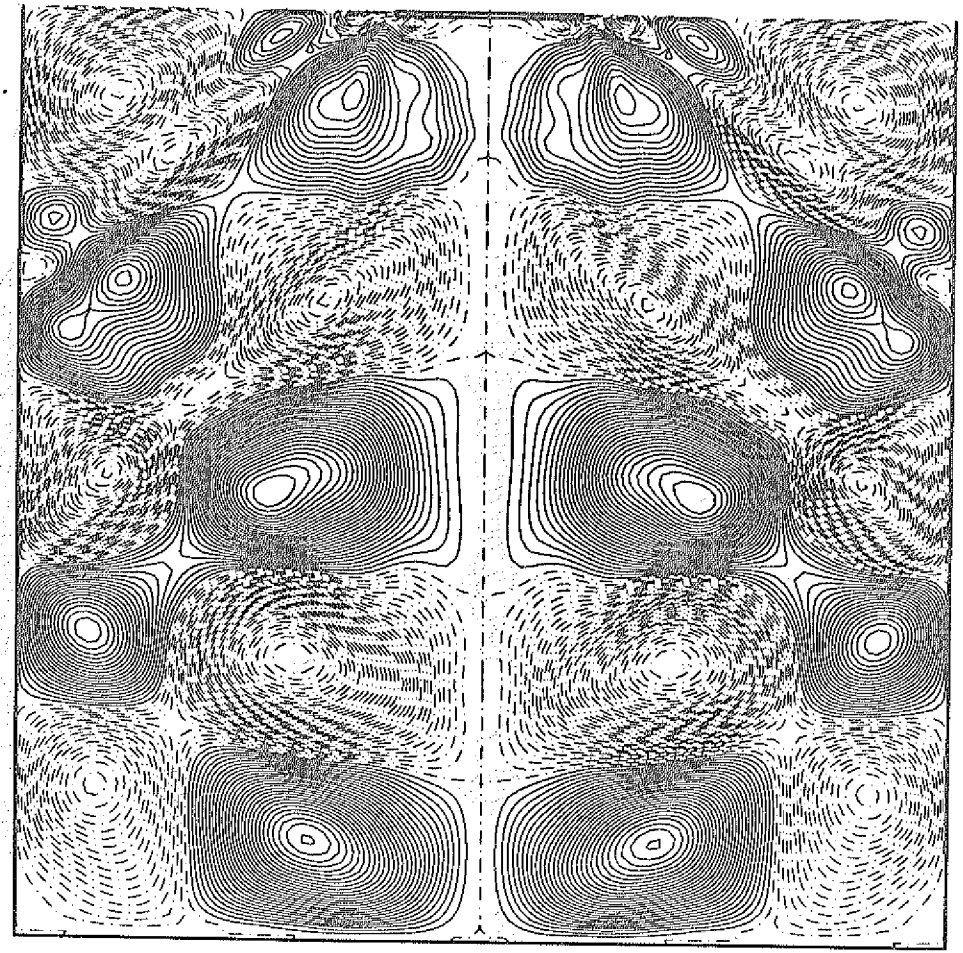

Fig.10c $t=$ $288.5\ s$

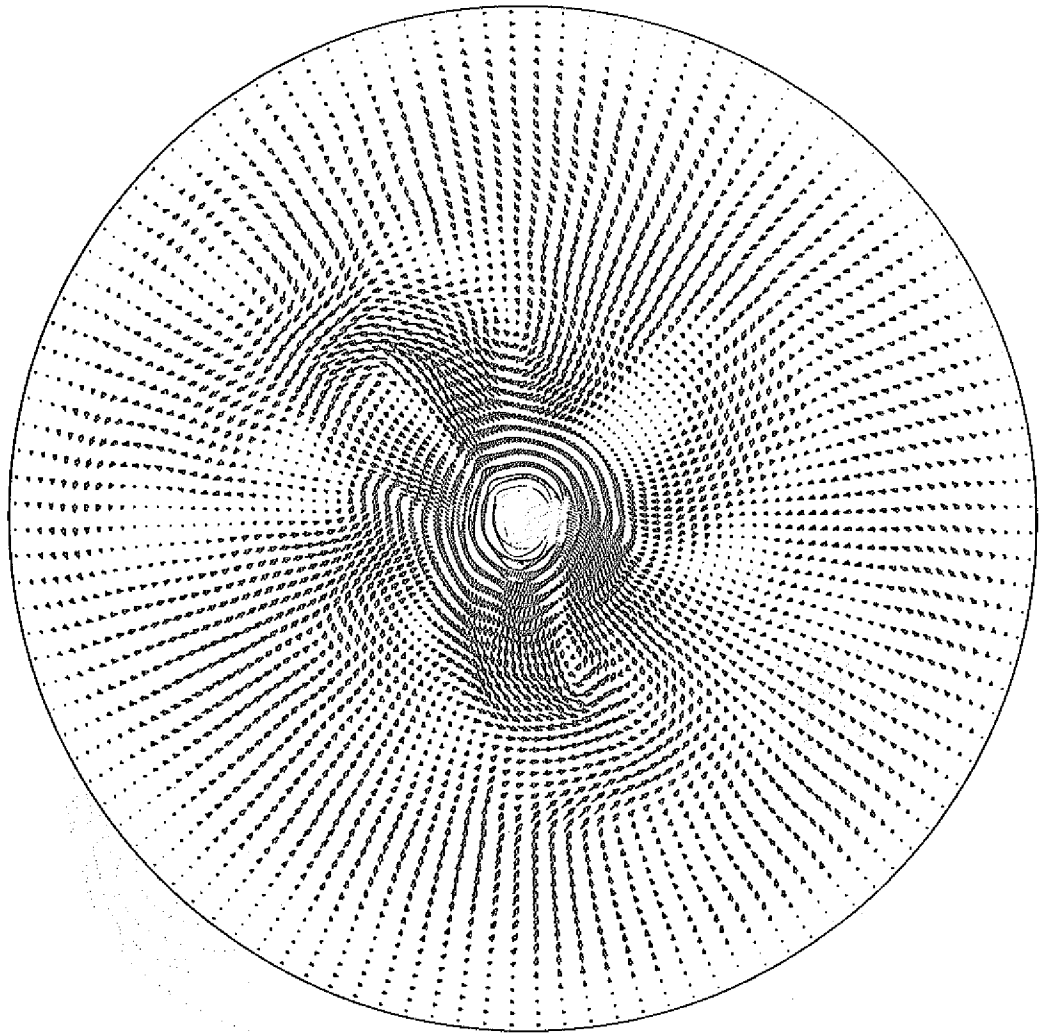

Fig.10d

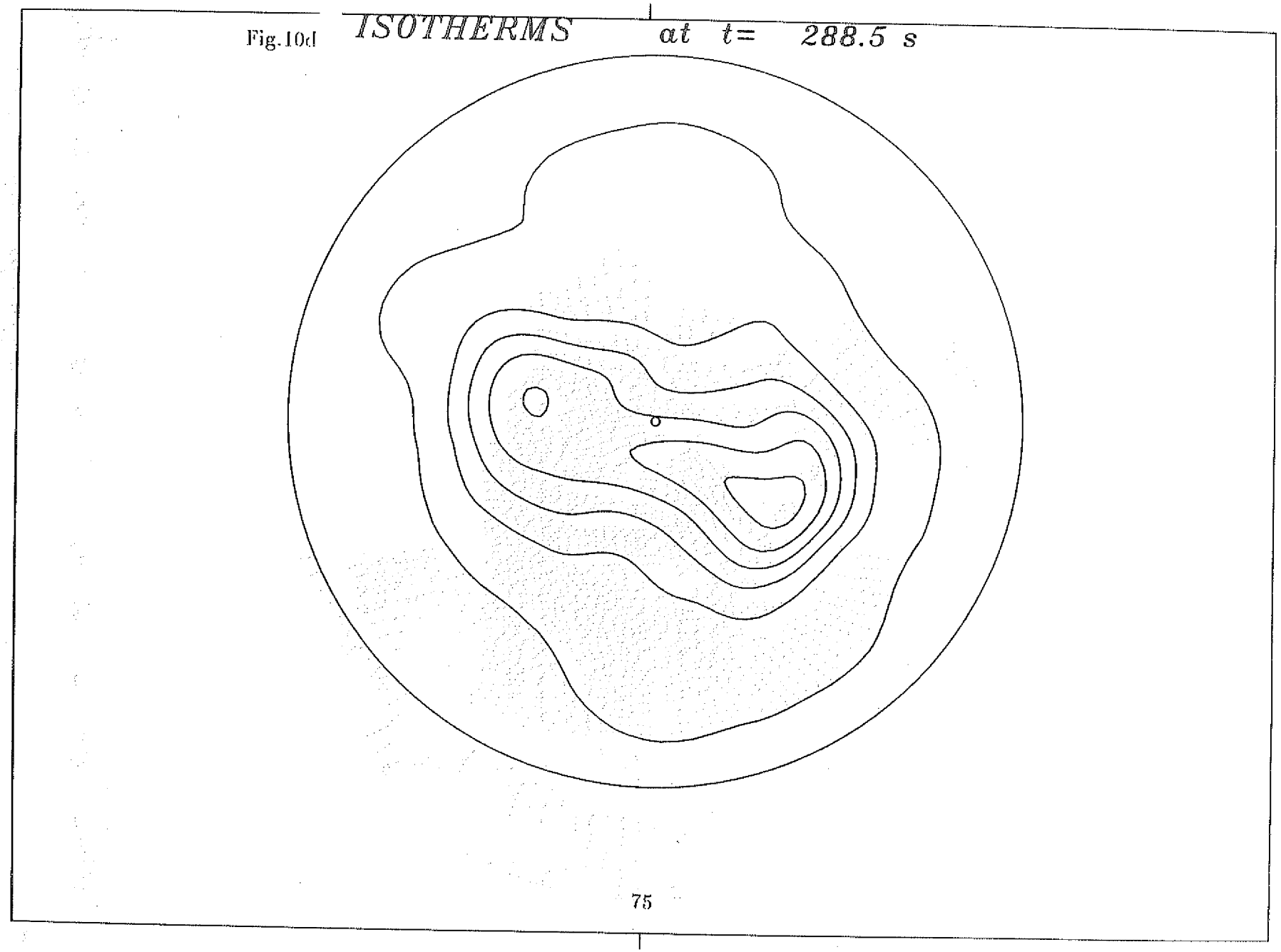

Fig.10e $t = 288.5\ s$

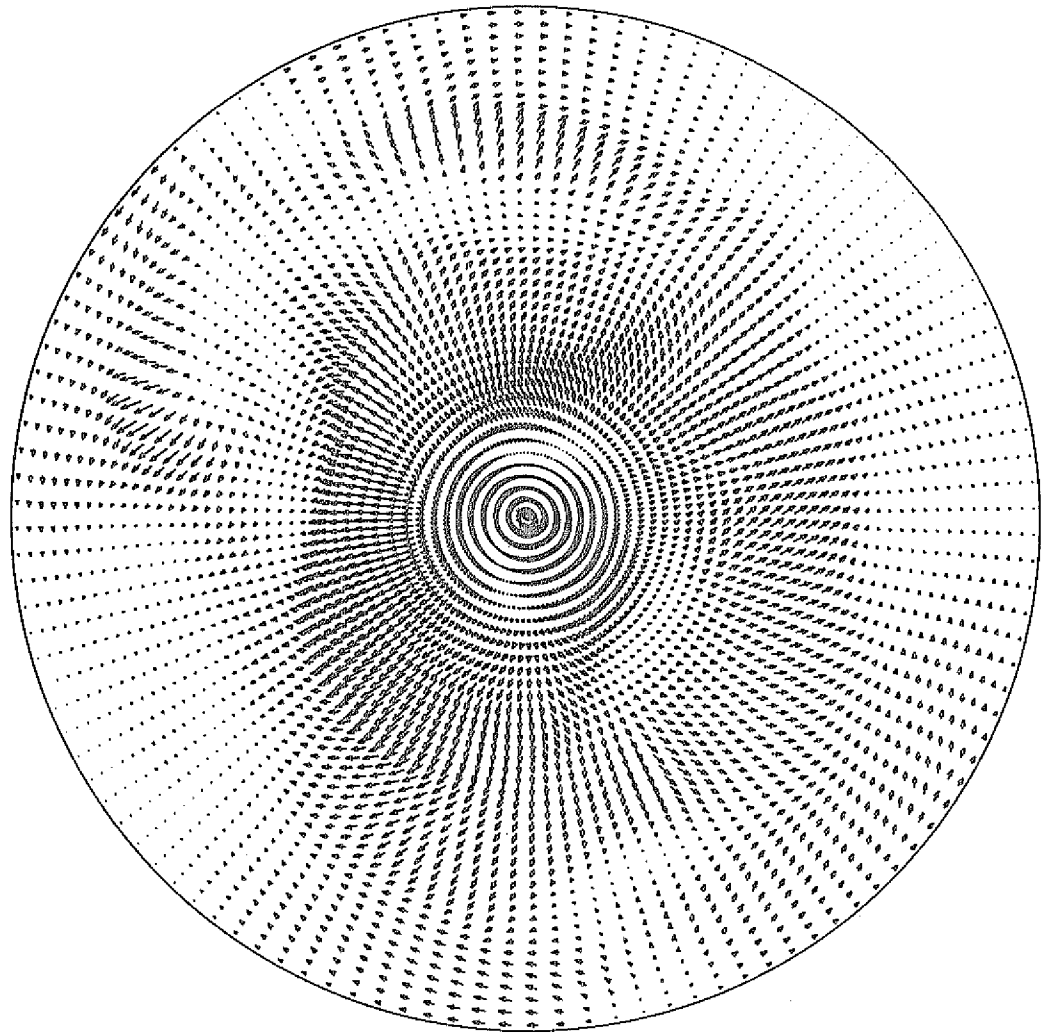

Fig.10f

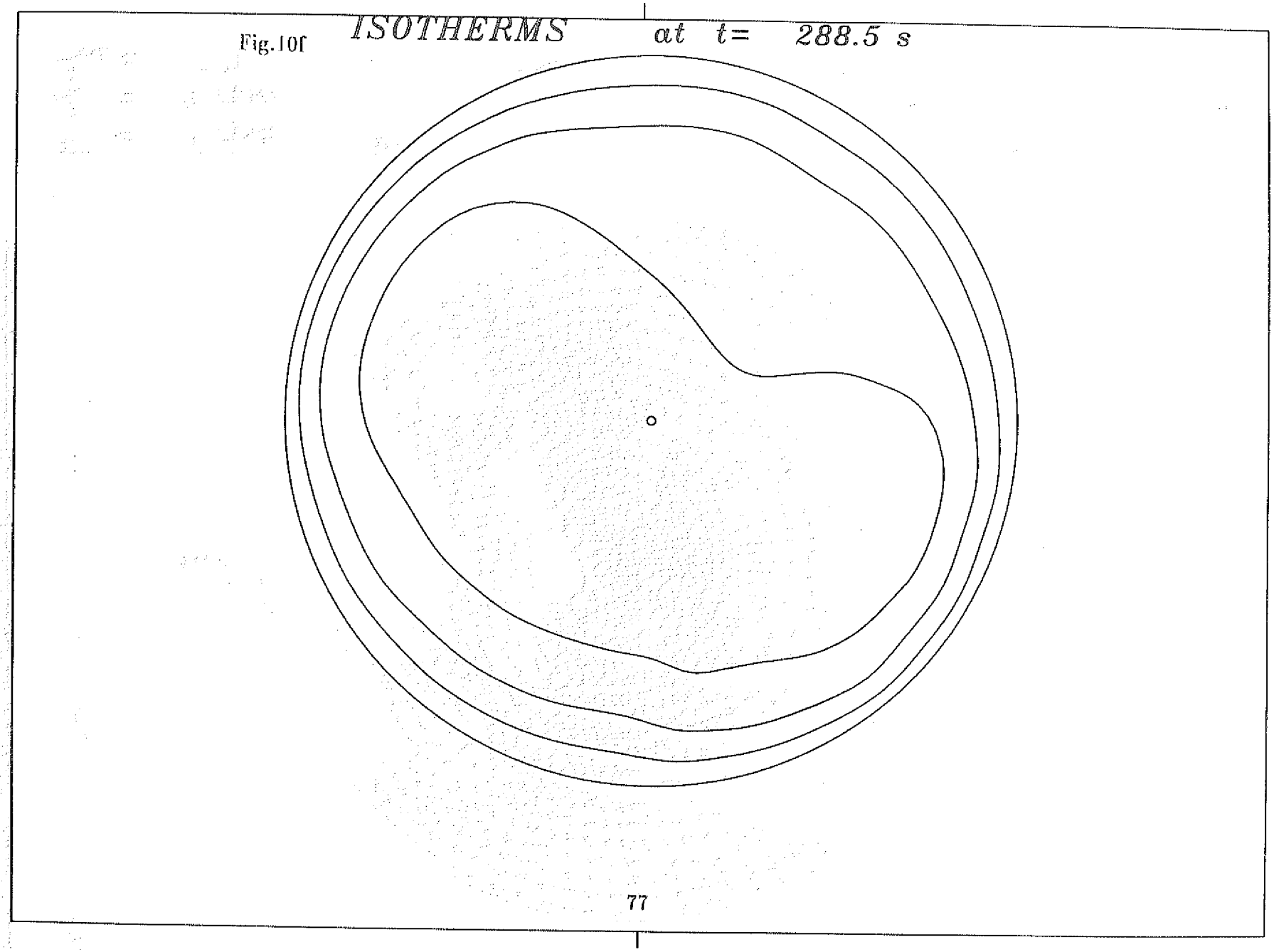

Fig.11a

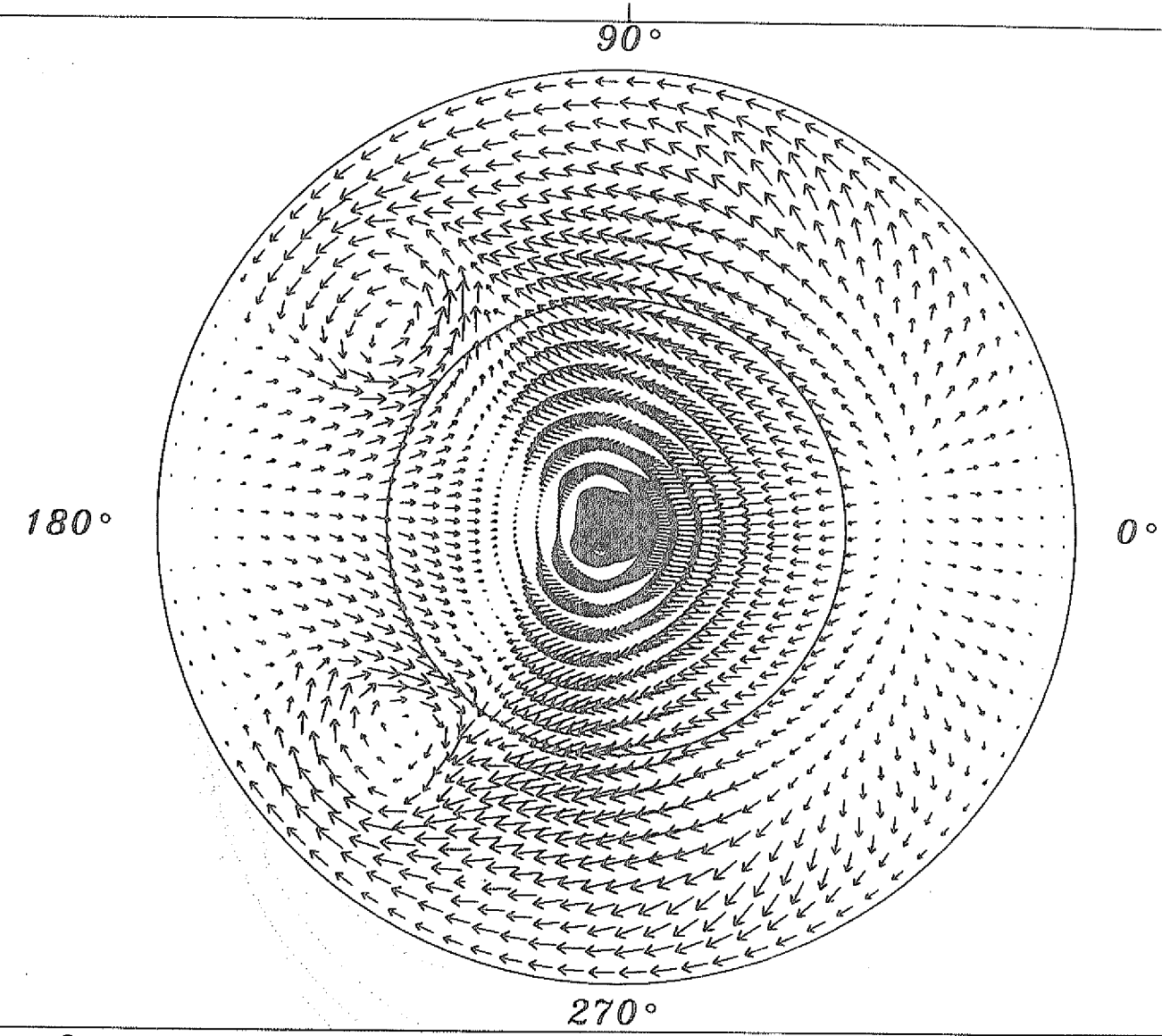

Ω_T	= 0 rpm	DPHI =	4.0 °	V_{max}	= 9.7E−01	RX	= 3.00 cm
Ω_C	= 0 rpm	DZ	= 0.15 cm	CUT	= 5.92 cm	CX	= 1.50 cm
T_{Bound}	= 5.0 °	ν	= 0.00328	t	= 290.0 s	HX	= 6.00 cm

Fig.11b

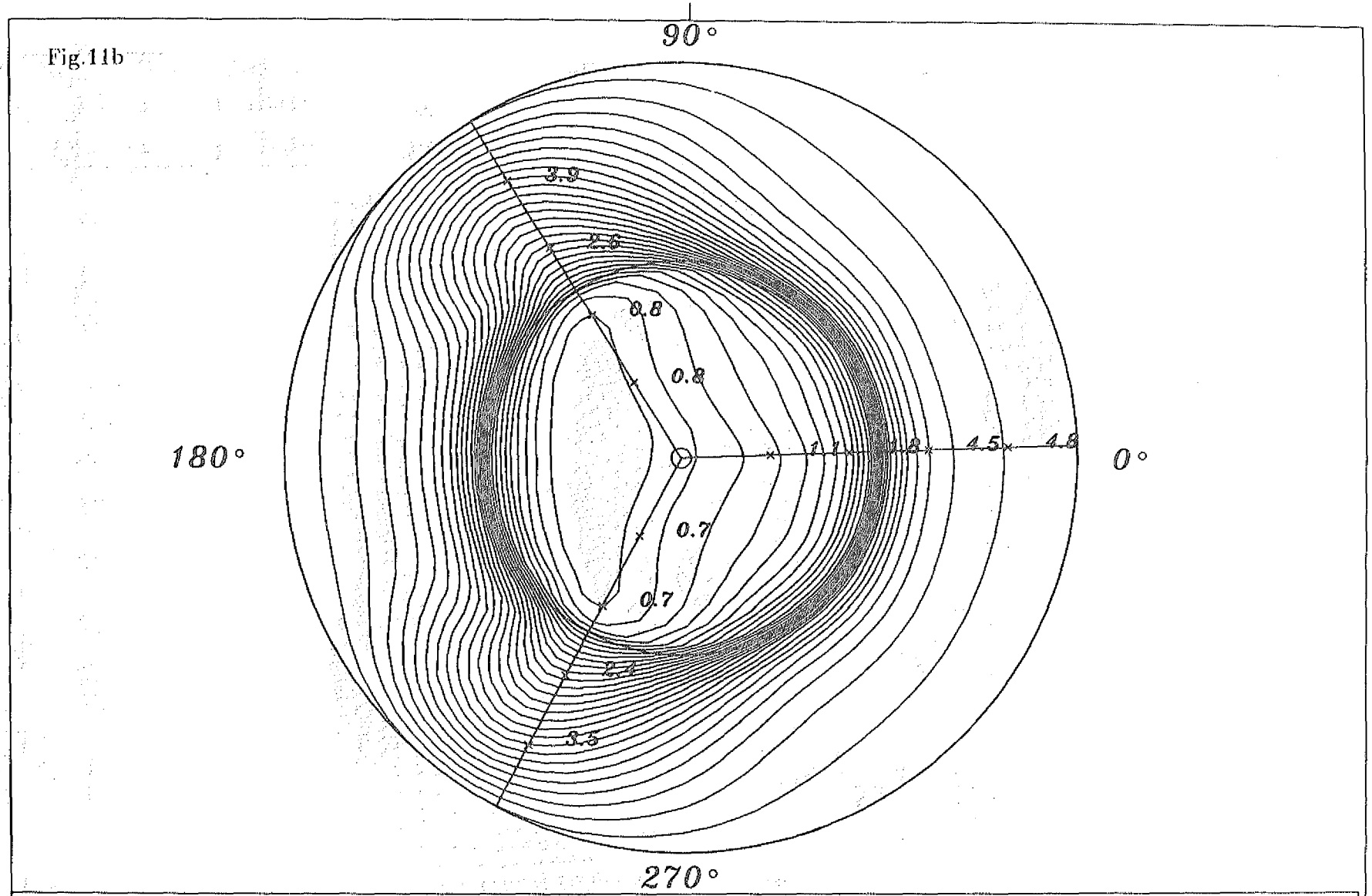

Ω_T	= 0 rpm	DPHI	= 4.0 °	V_{max}	= 9.7E−01	RX	= 3.00 cm
Ω_C	= 0 rpm	DZ	= 0.15 cm	CUT	= 5.92 cm	CX	= 1.50 cm
T_{Bound}	= 5.0 °	ν	= 0.00328	t	= 290.0 s	HX	= 6.00 cm

Fig.11c

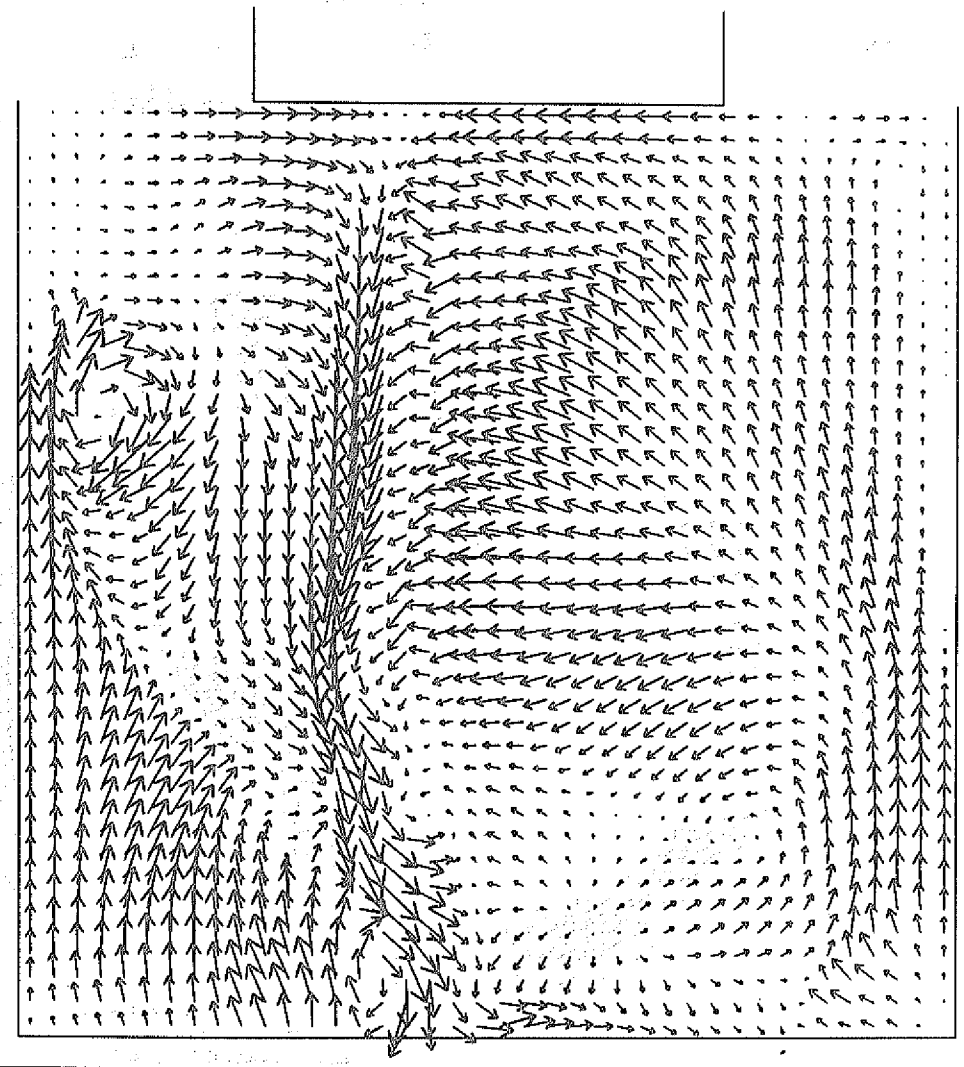

Ω_T	=	0 rpm	DR	=	0.15 cm	V_{max}	=	7.2E−01	RX	=	3.00 cm
Ω_C	=	0 rpm	DZ	=	0.15 cm	CUT	=	2.0 °	CX	=	1.50 cm
T_{Bound}	=	5.0 °	ν	=	0.00328	t	=	280.0 s	HX	=	6.00 cm

Fig.11d

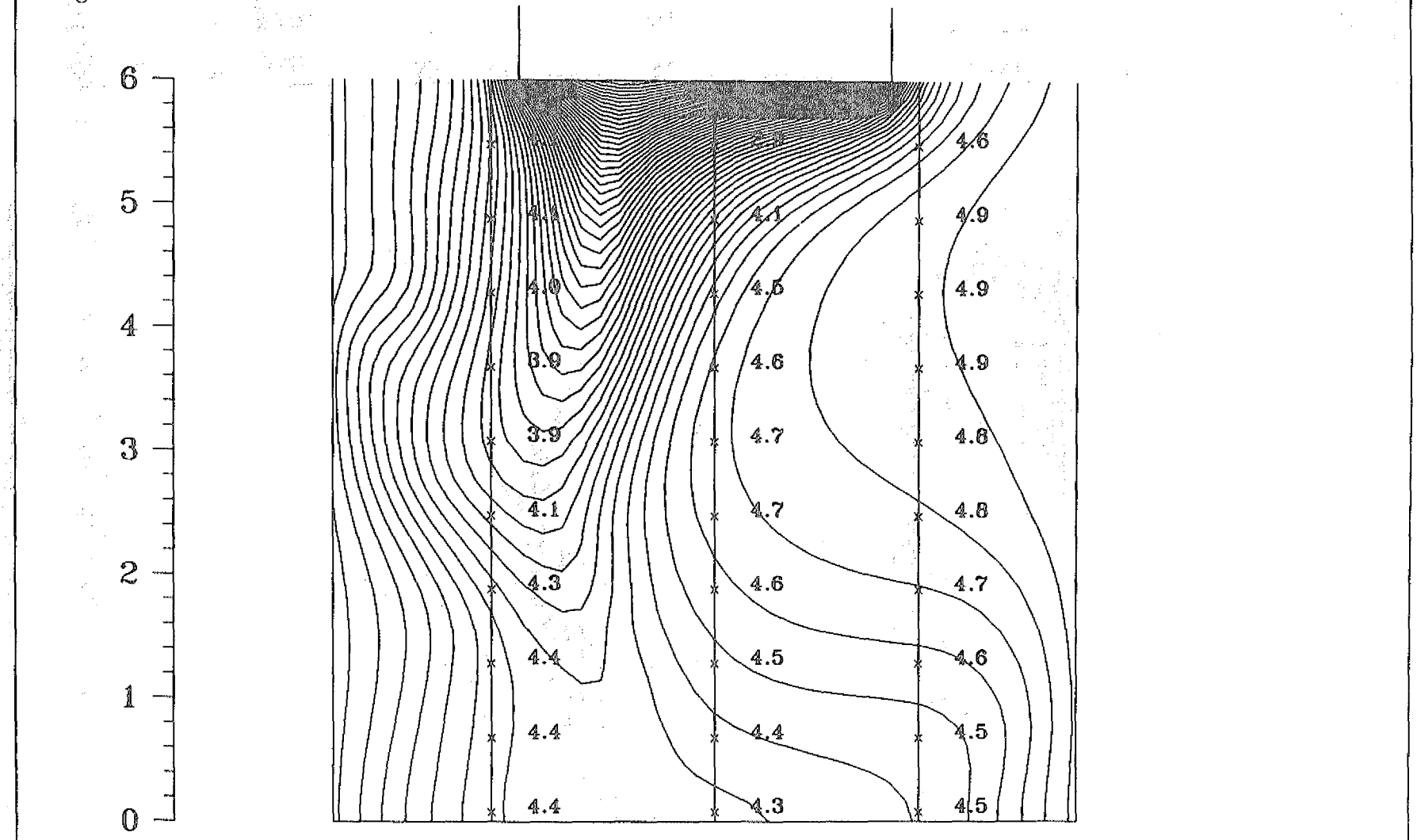

Ω_T = 0 rpm	DR = 0.15 cm	V_{max} = 7.2E−01	RX = 3.00 cm
Ω_C = 0 rpm	DZ = 0.15 cm	CUT = 2.0 °	CX = 1.50 cm
T_{Bound} = 5.0 °	ν = 0.00328	t = 280.0 s	HX = 6.00 cm

Fig.11c

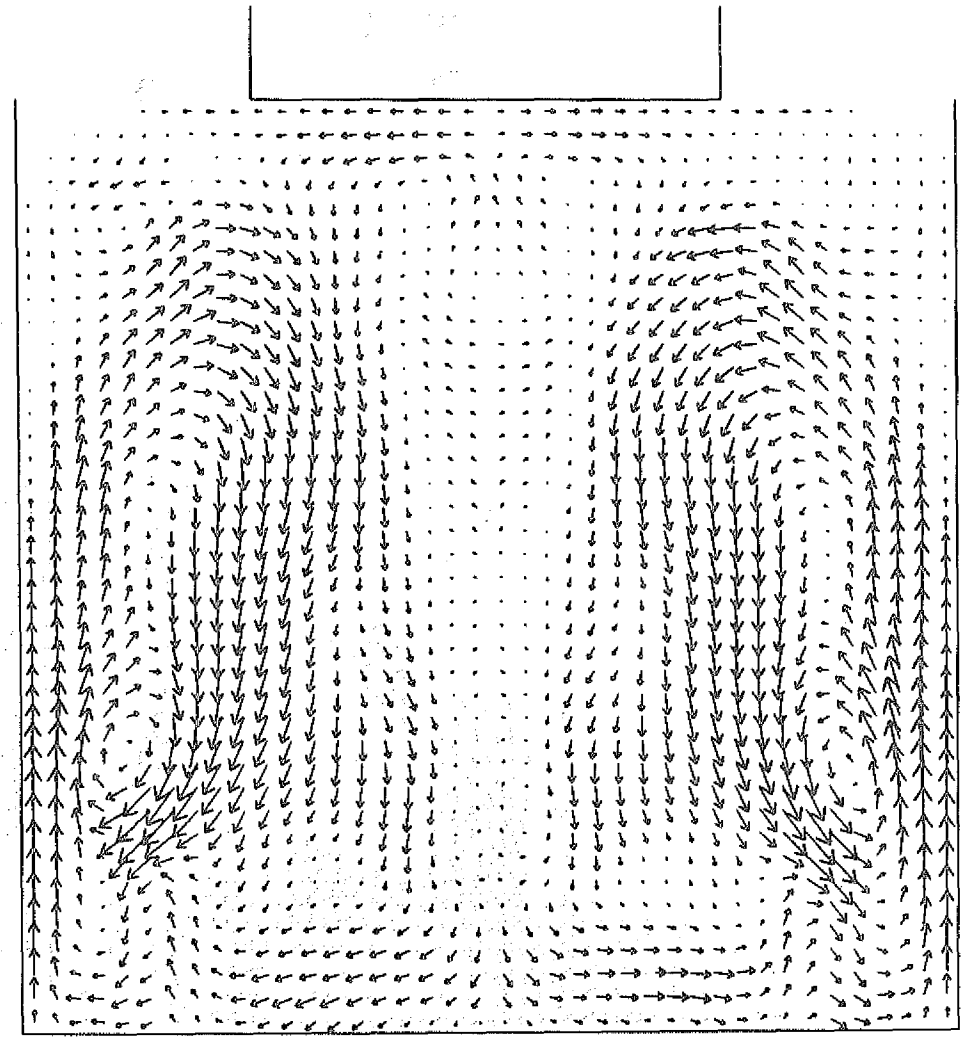

Ω_T	=	0 rpm	DR	=	0.15 cm	V_{max}	=	8.5E−01	RX	=	3.00 cm
Ω_C	=	0 rpm	DZ	=	0.15 cm	CUT	=	90.0 °	CX	=	1.50 cm
T_{Bound}	=	5.0 °	ν	=	0.00328	t	=	280.0 s	HX	=	6.00 cm

Fig.11f

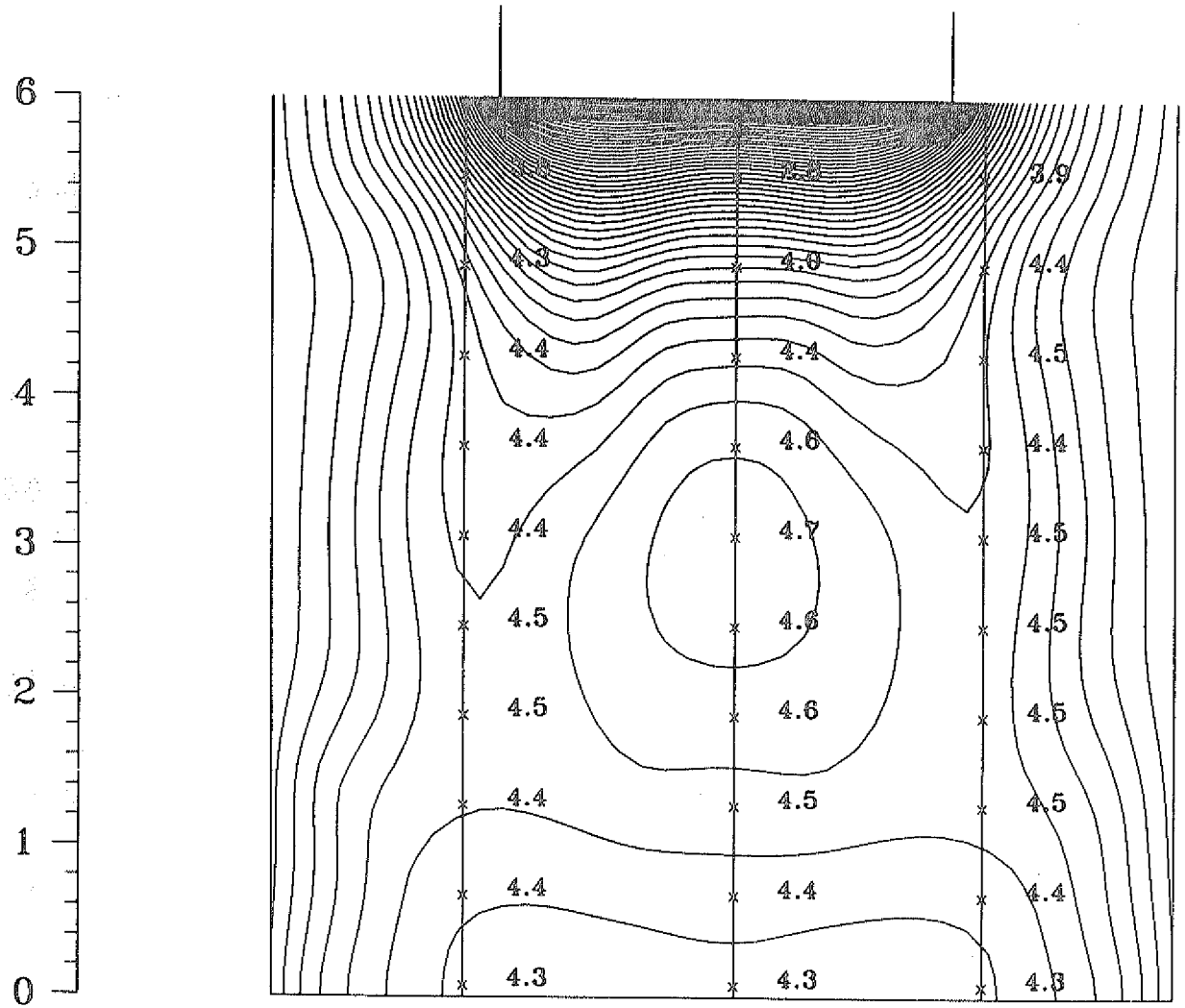

Ω_T	= 0 rpm	DR	= 0.15 cm	V_{max}	= 8.5E−01	RX	= 3.00 cm
Ω_C	= 0 rpm	DZ	= 0.15 cm	CUT	= 90.0 °	CX	= 1.50 cm
T_{Bound}	= 5.0 °	ν	= 0.00328	t	= 280.0 s	HX	= 6.00 cm

Fig.12a

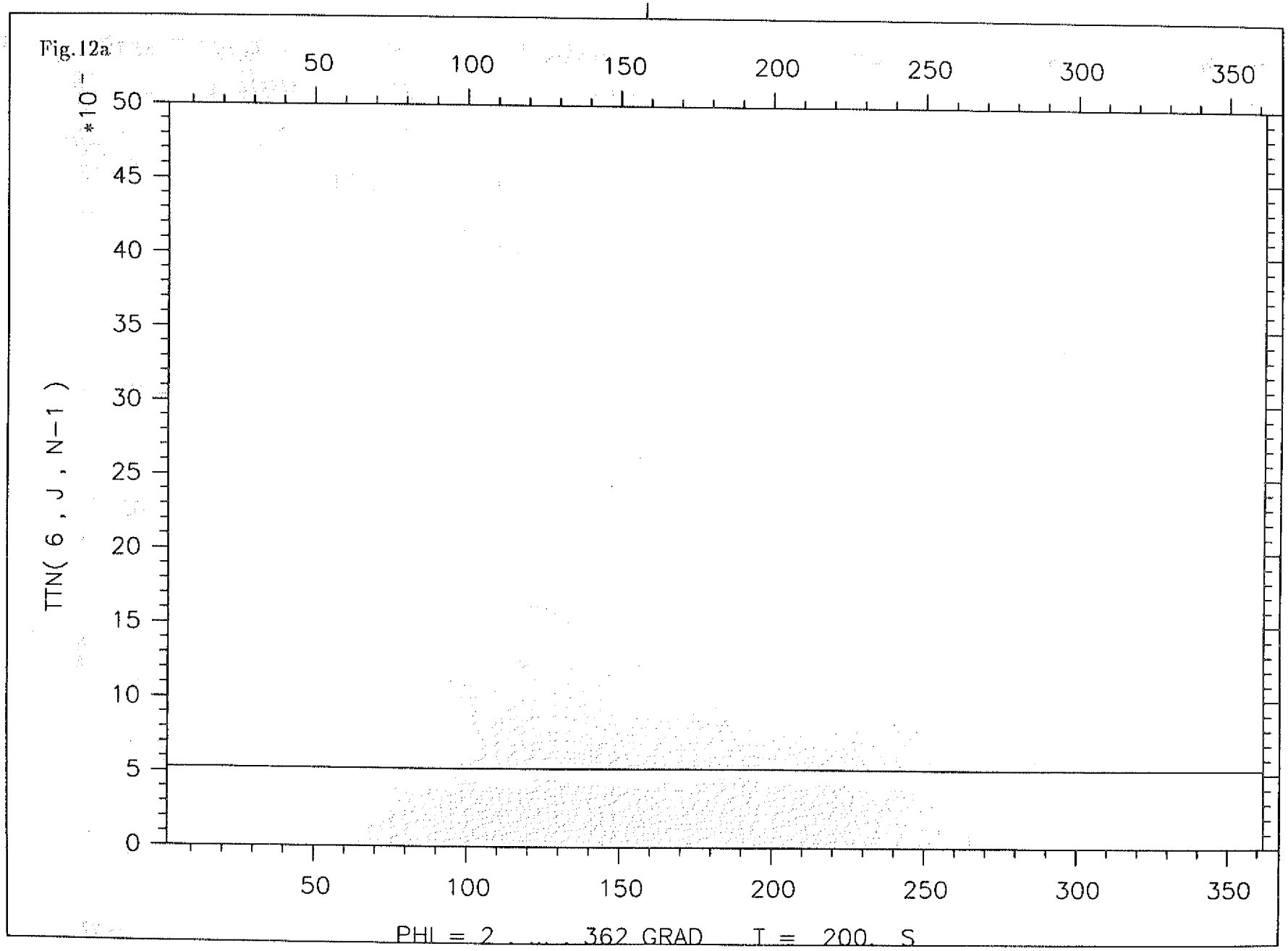
50
100
150
200
250
300
350
*10 -
50
45
40
35
30
25
20
15
10
5
0
TTN(6 , J , N-1)
50
100
150
200
250
300
350
PHI = 2 362 GRAD T = 200. S

Fig.12b

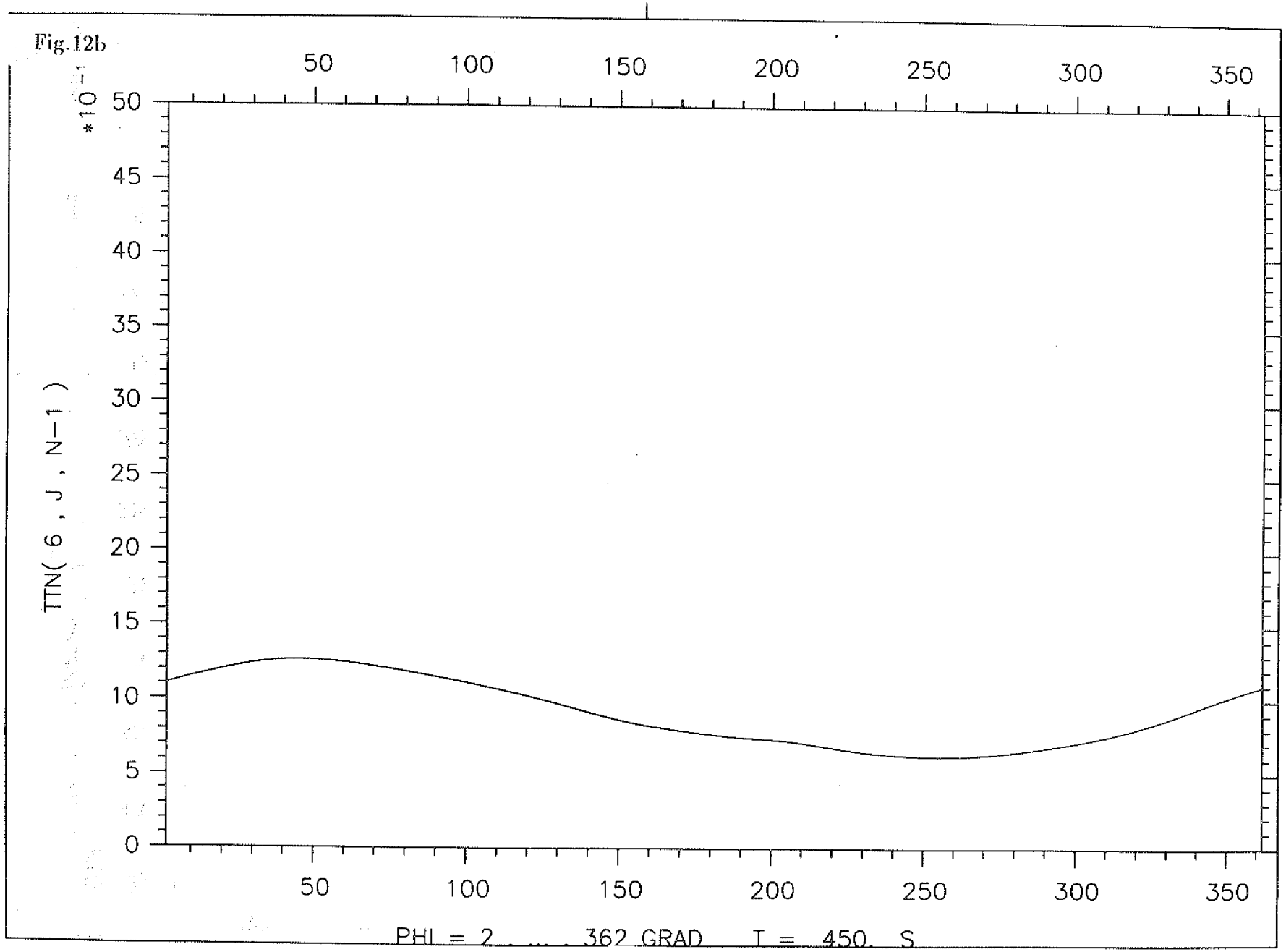
50
100
150
200
250
300
350
*10⁻¹
50
45
40
35
30
25
20
15
10
5
0
TTN(6 , J , N-1)
50
100
150
200
250
300
350
PHI = 2 . ... . 362 GRAD T = 450. S

Fig.13

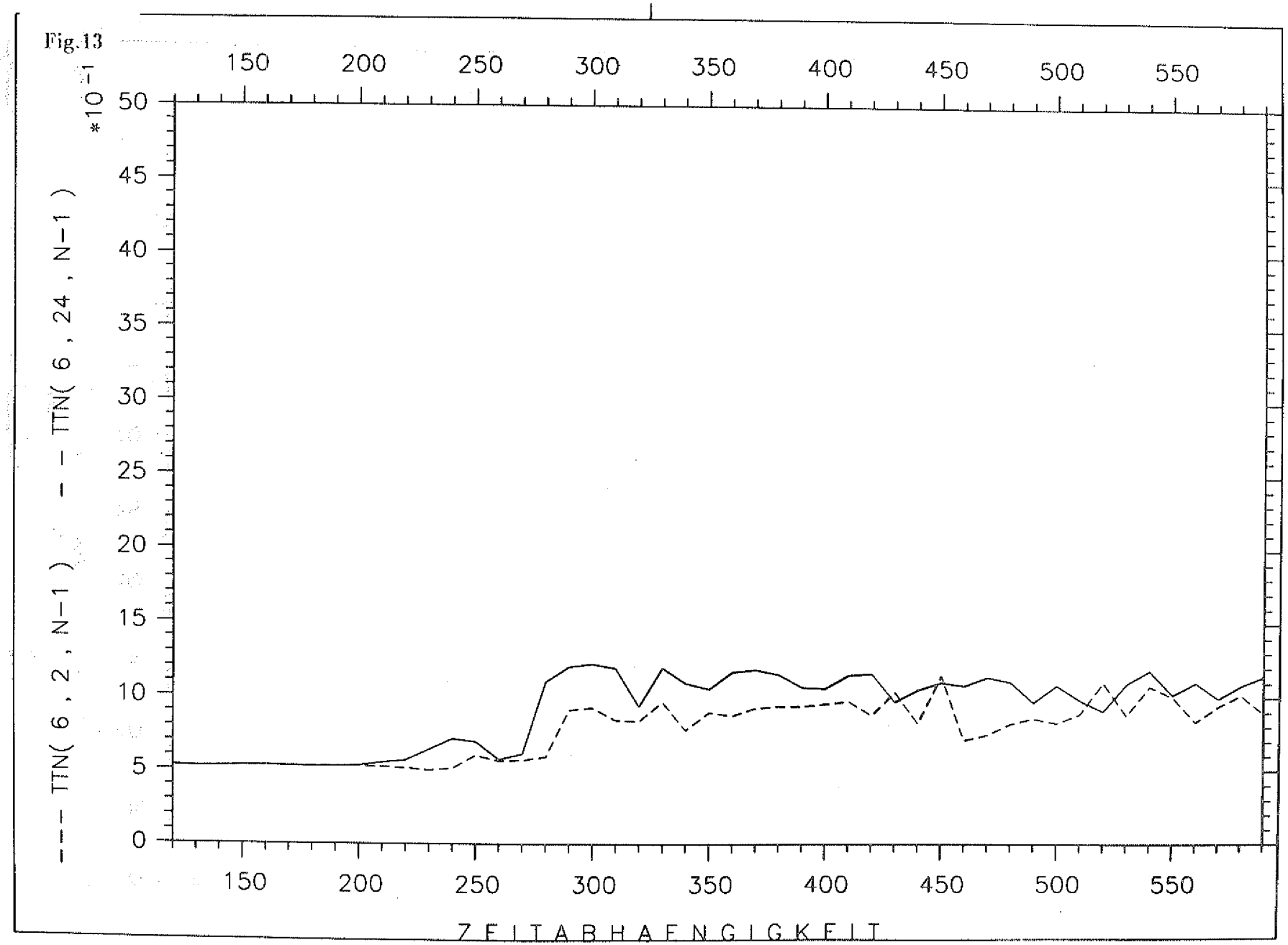
150
200
250
300
350
400
450
500
550
*10 -1
50
45
40
35
30
25
20
15
10
5
0
--- TTN(6 , 2 , N-1)
- - TTN(6 , 24 , N-1)
ZEITABHAENGIGKEIT

Fig.14a $t = 125.0\ s$

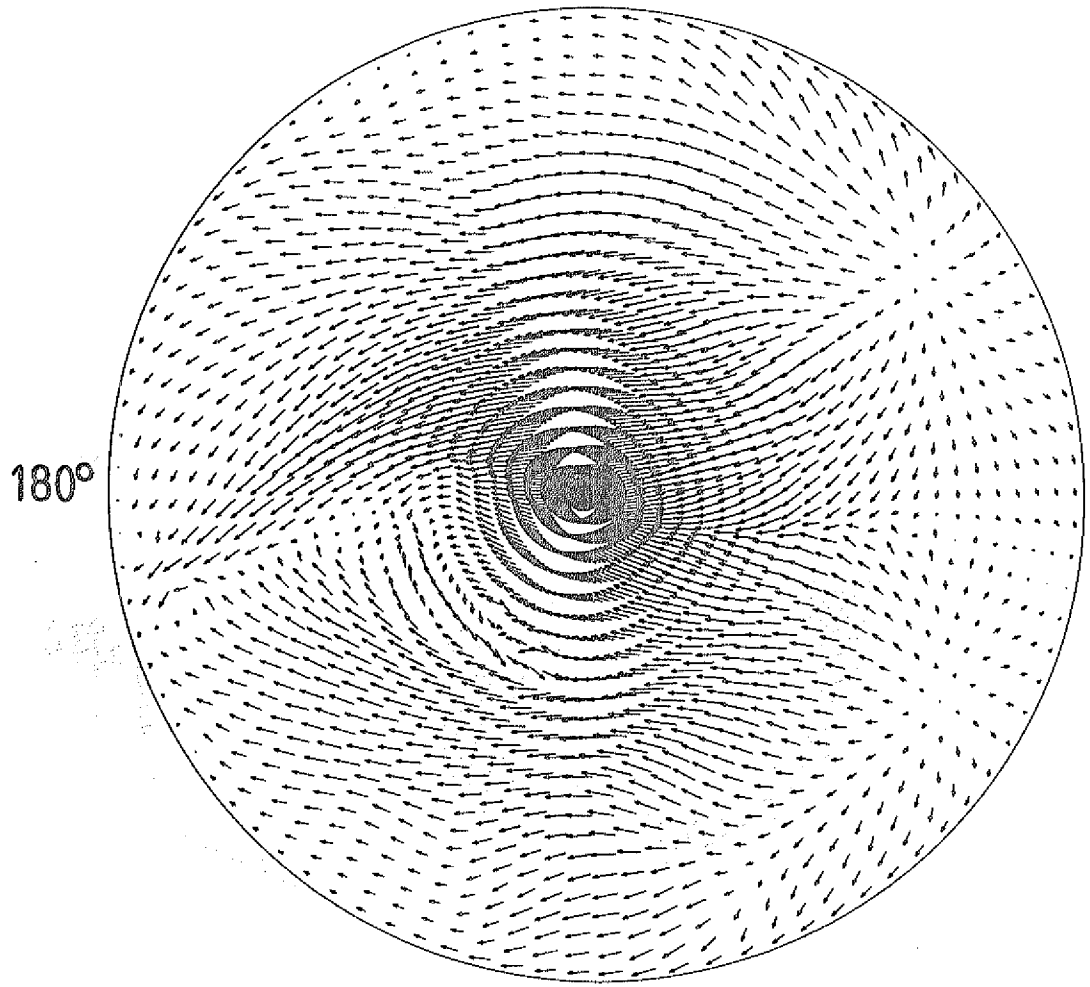

Fig.14b

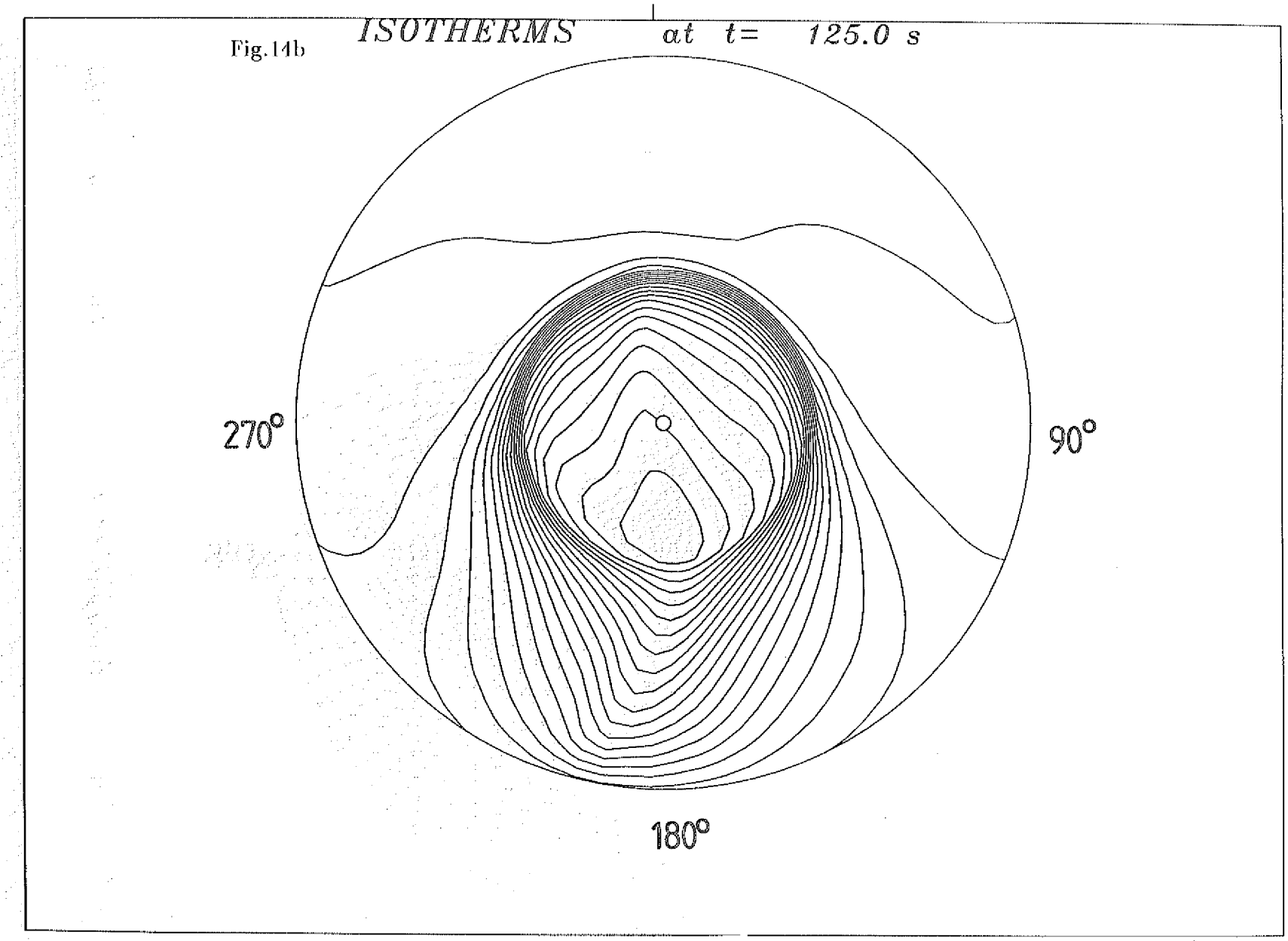

Fig.15a $t=$ 300.0 s

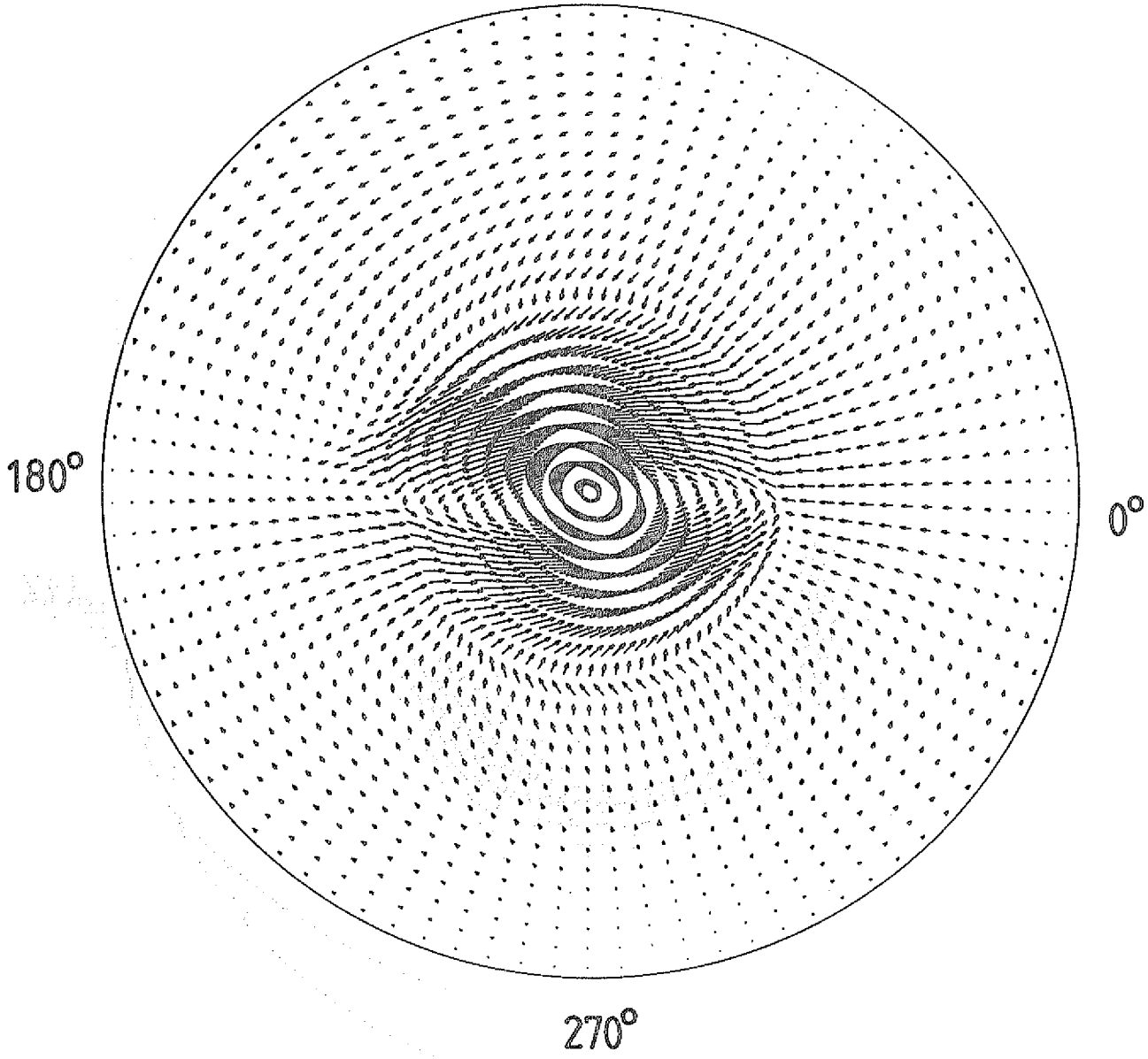

Fig.15b *ISOTHERMS* *at t= 300.0 s*

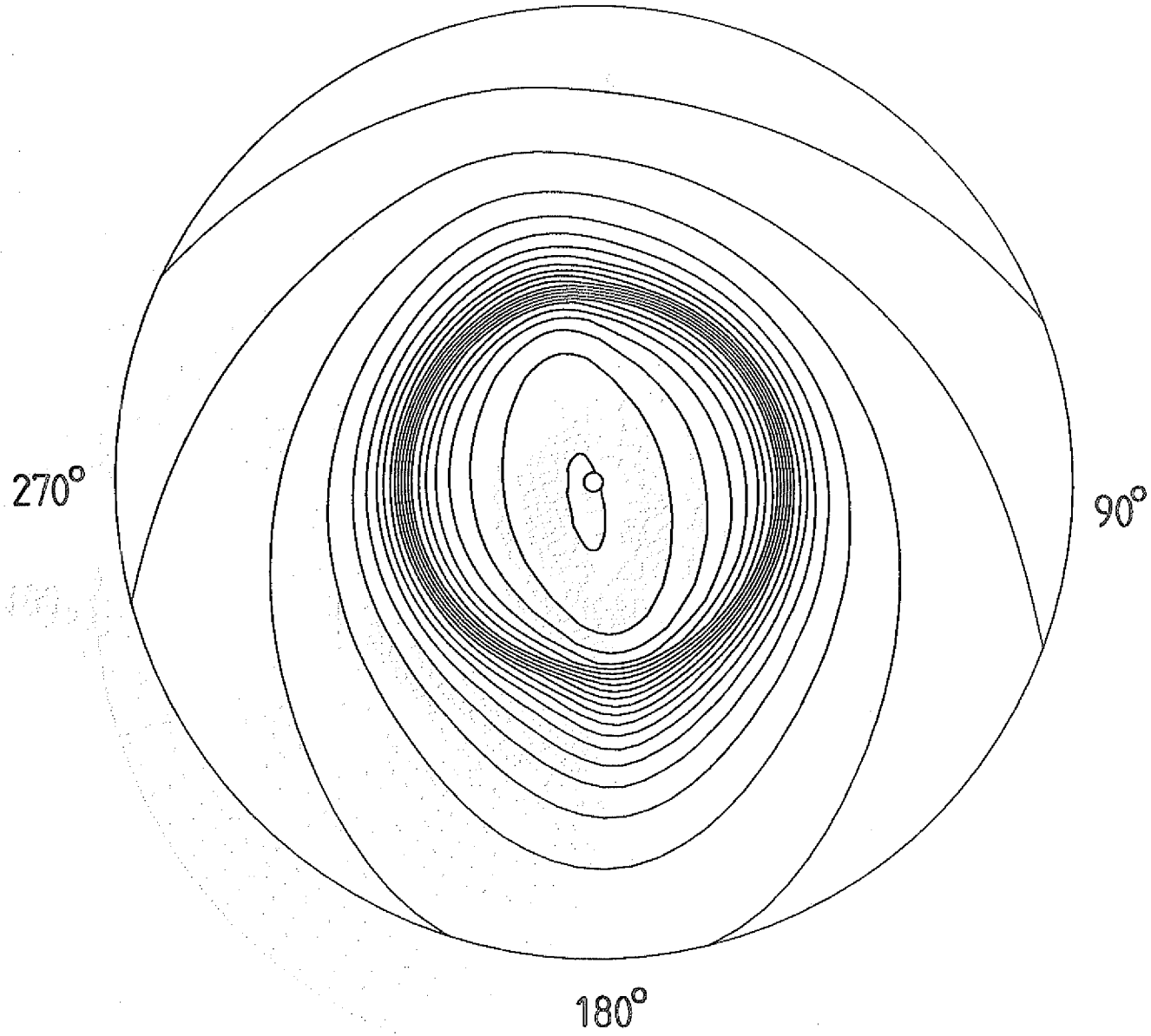

Fig.16a $t = 455.0\ s$

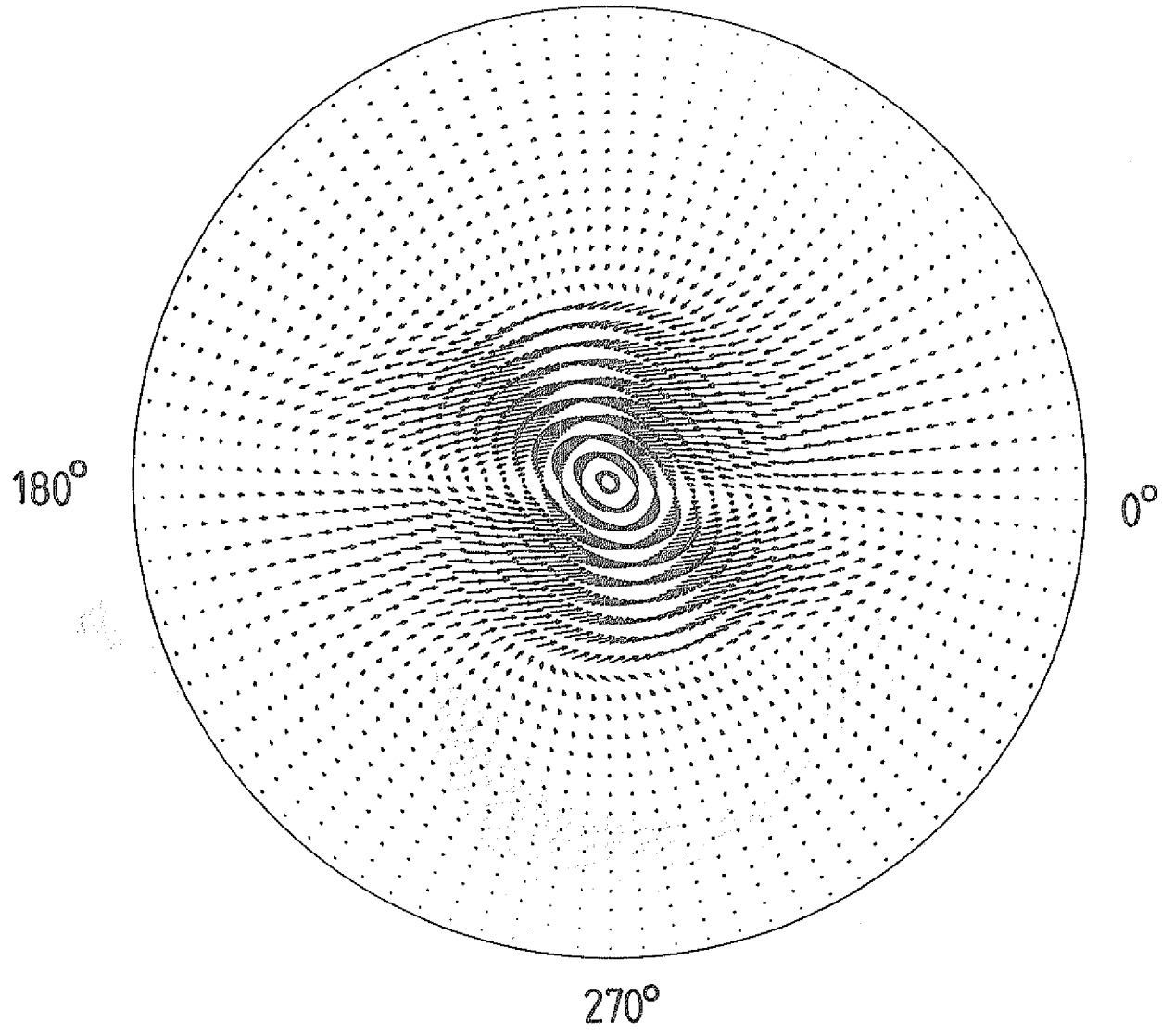

Fig.16b *ISOTHERMS* *at t= 455.0 s*

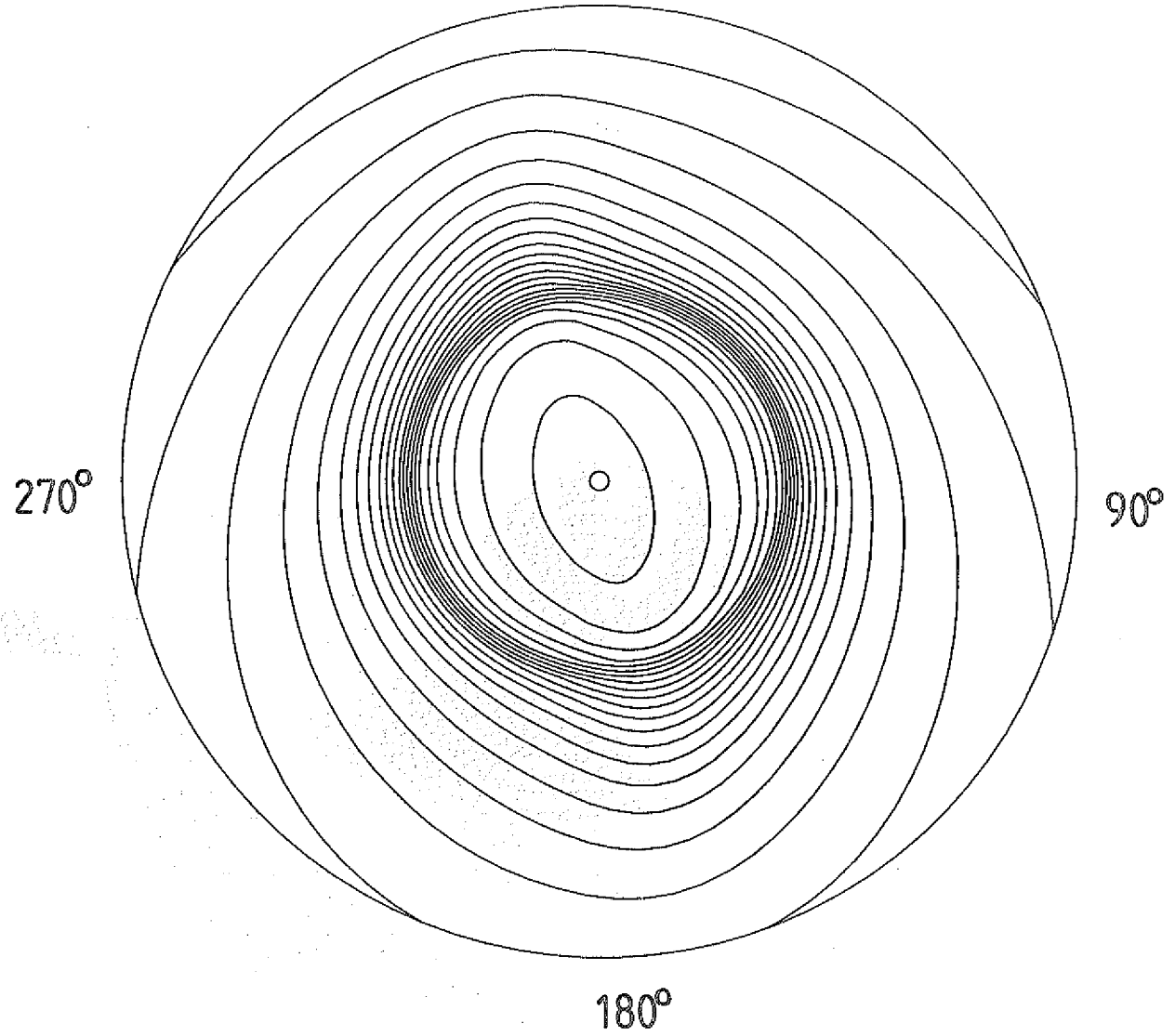

Fig.17a $at \quad t = \quad 305.0 \ s$

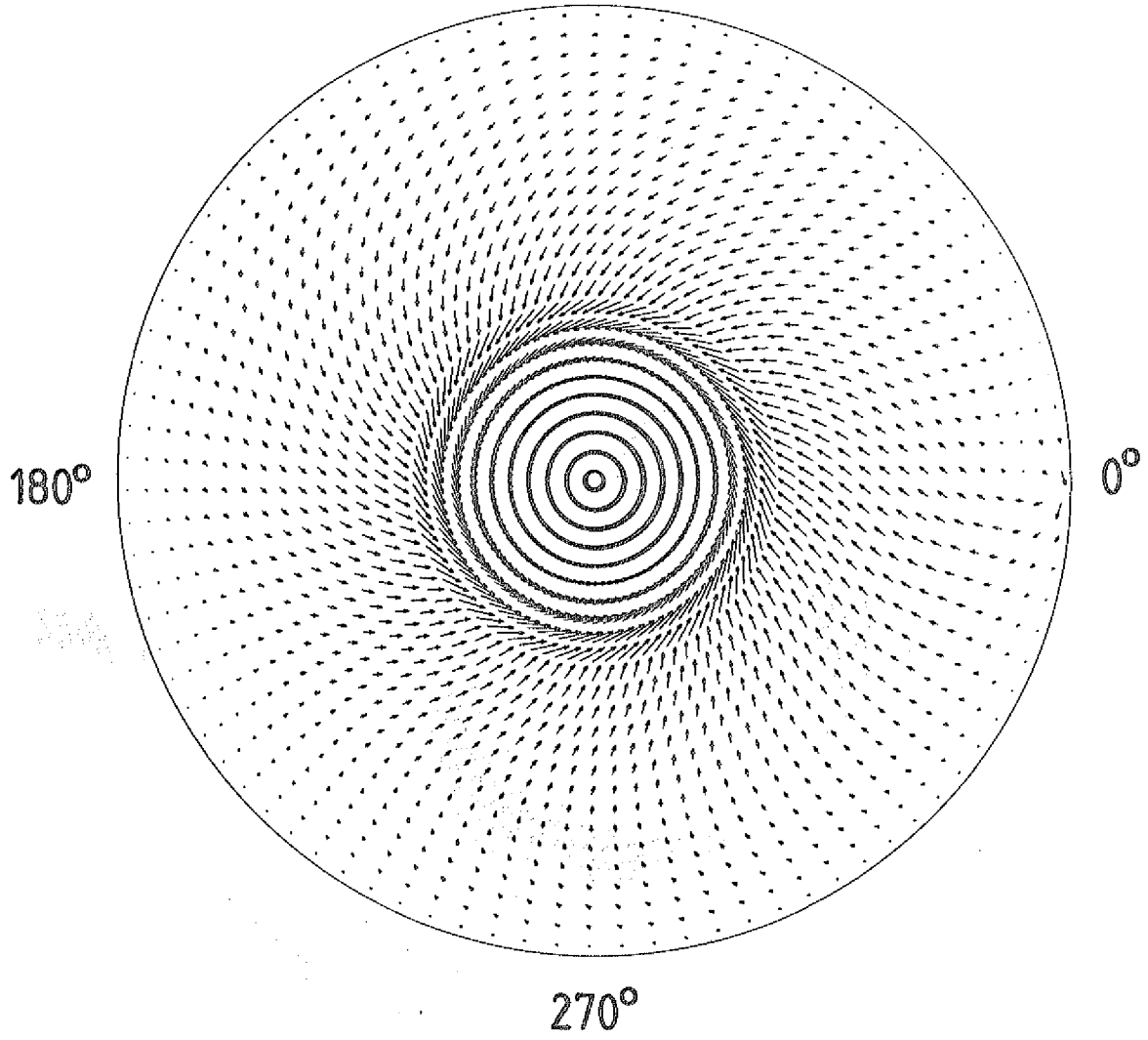

Fig.17b *ISOTHERMS* *at t= 305.0 s*

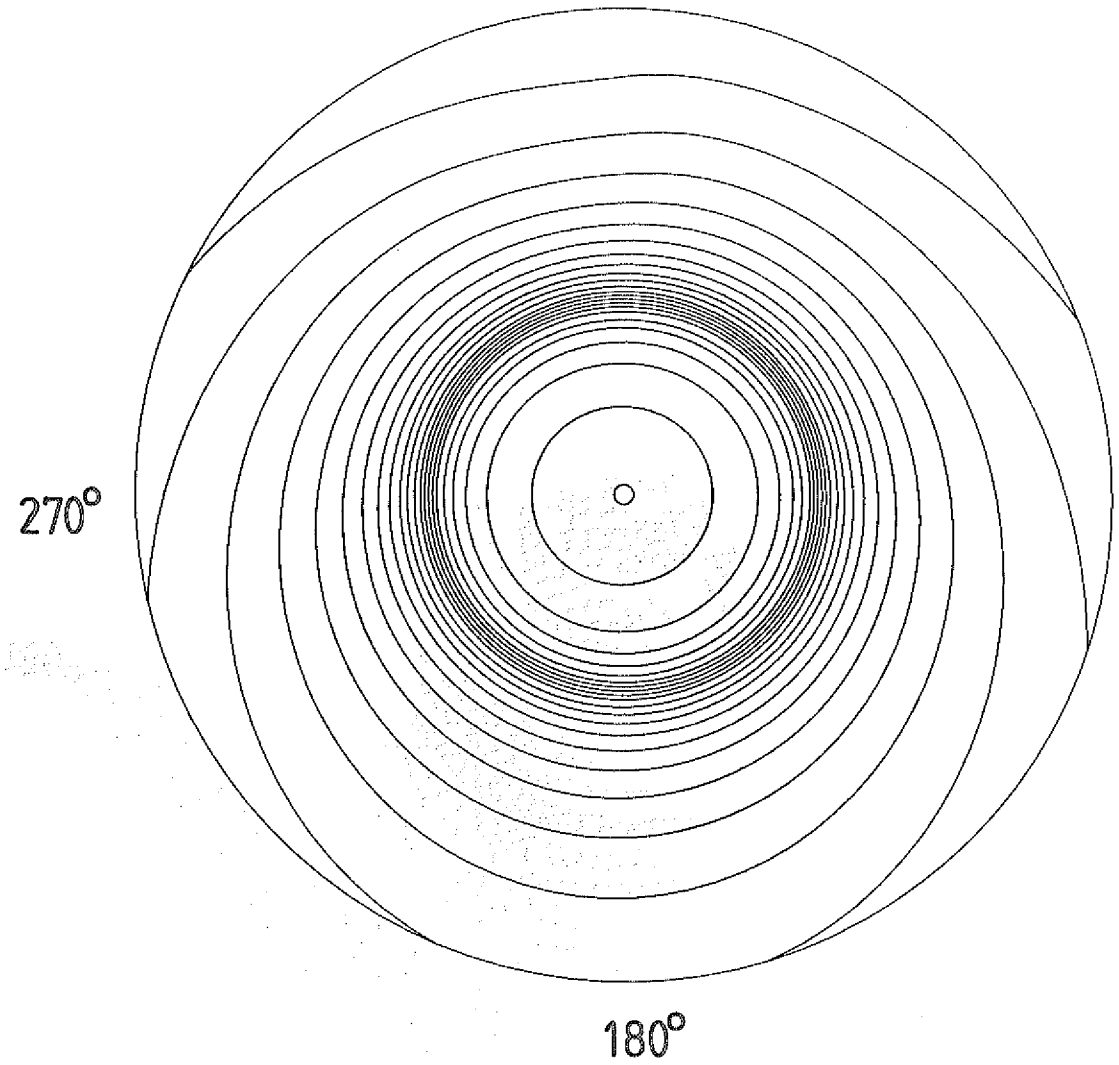

Fig.18a $at \quad t = \quad 480.0 \ s$

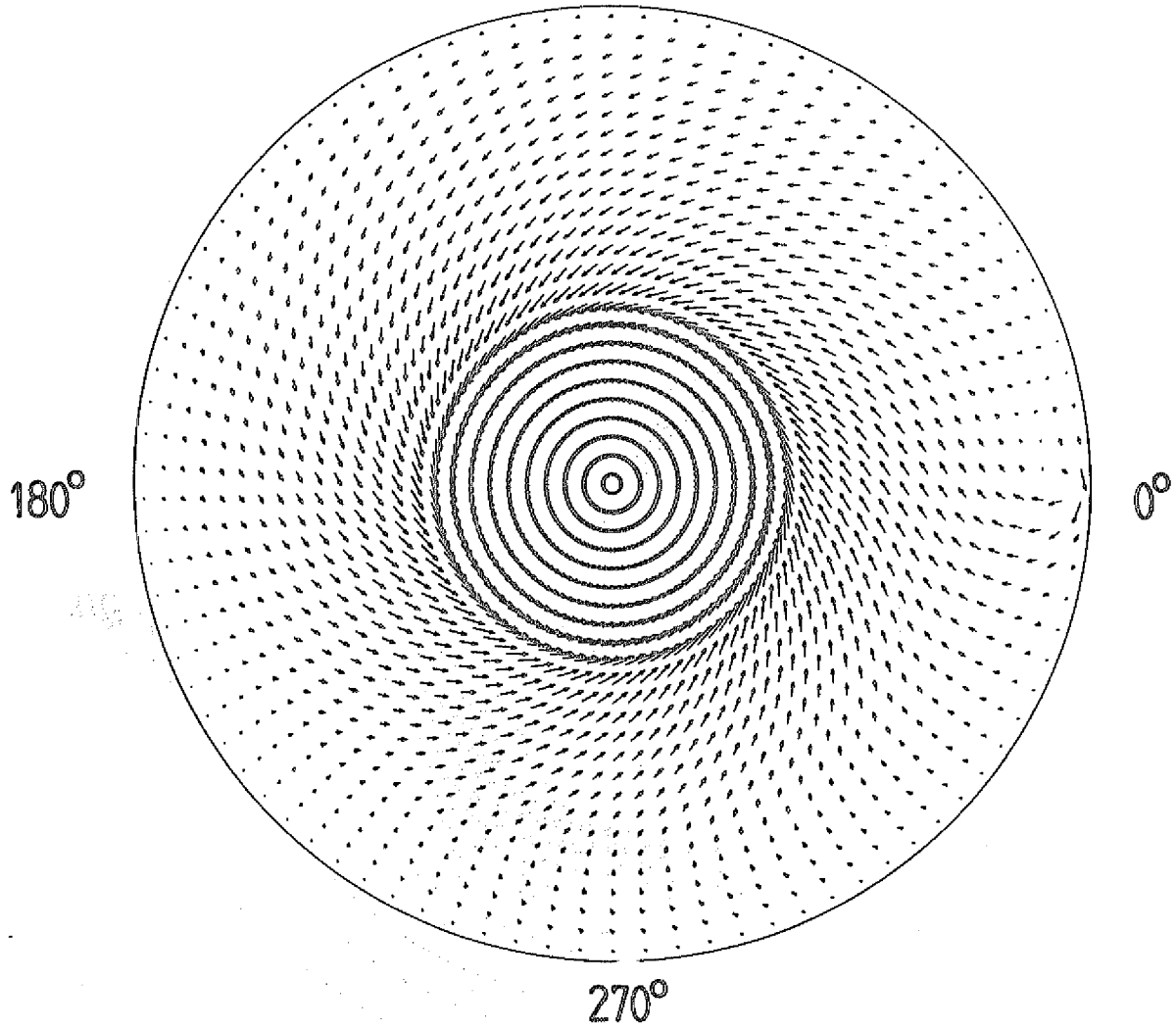

Fig.18b

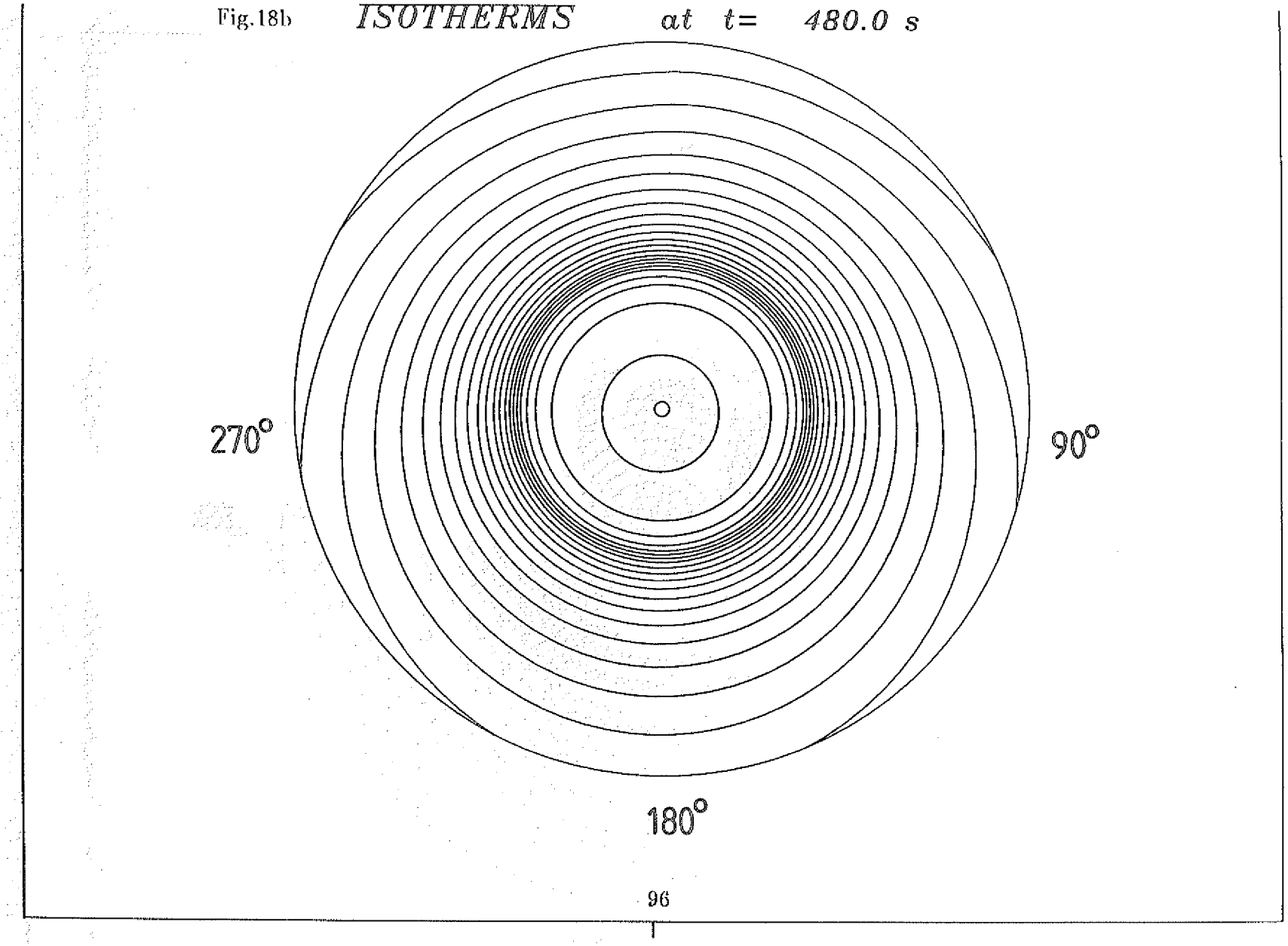

Fig.19a

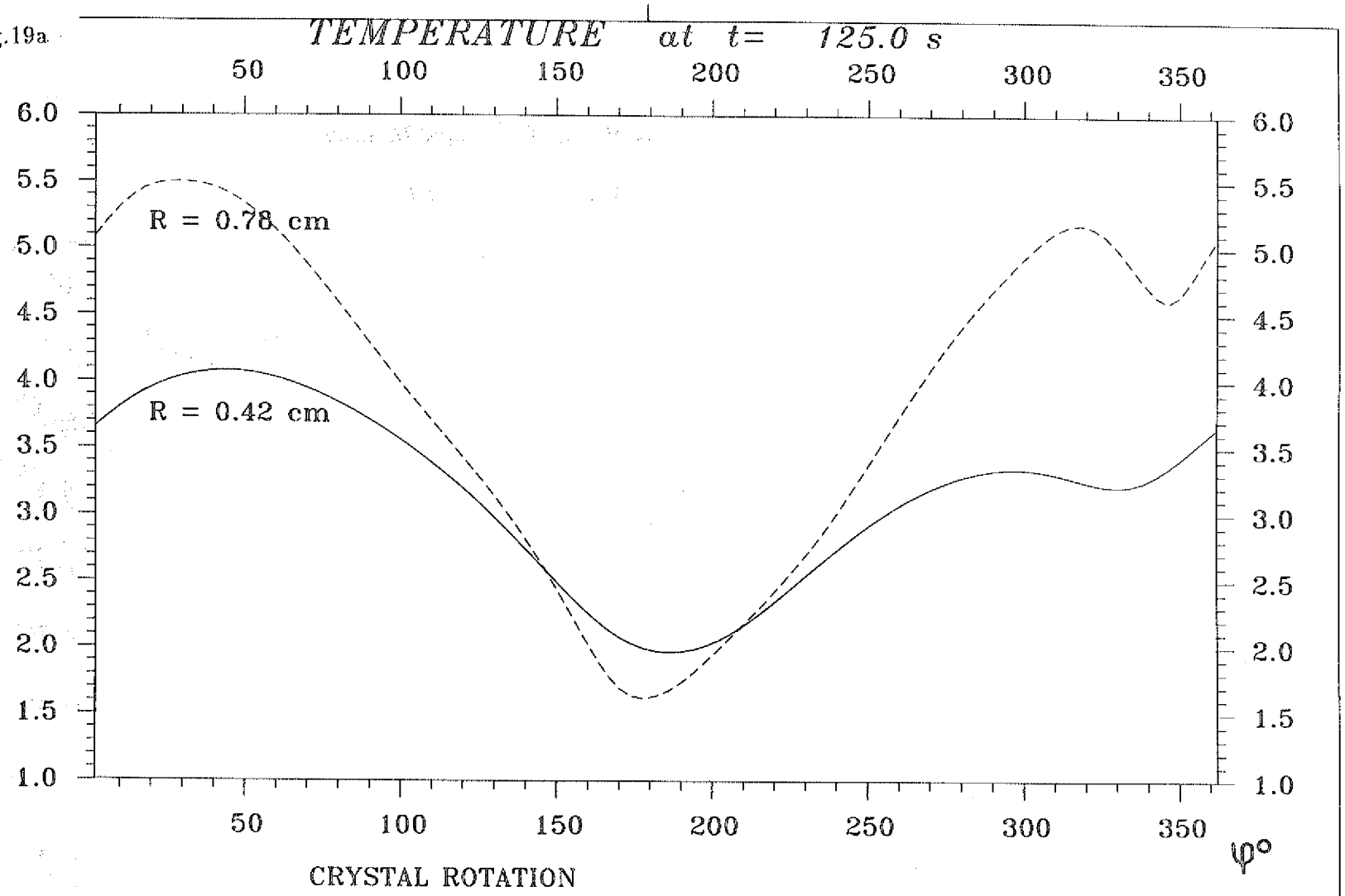

Fig.19b

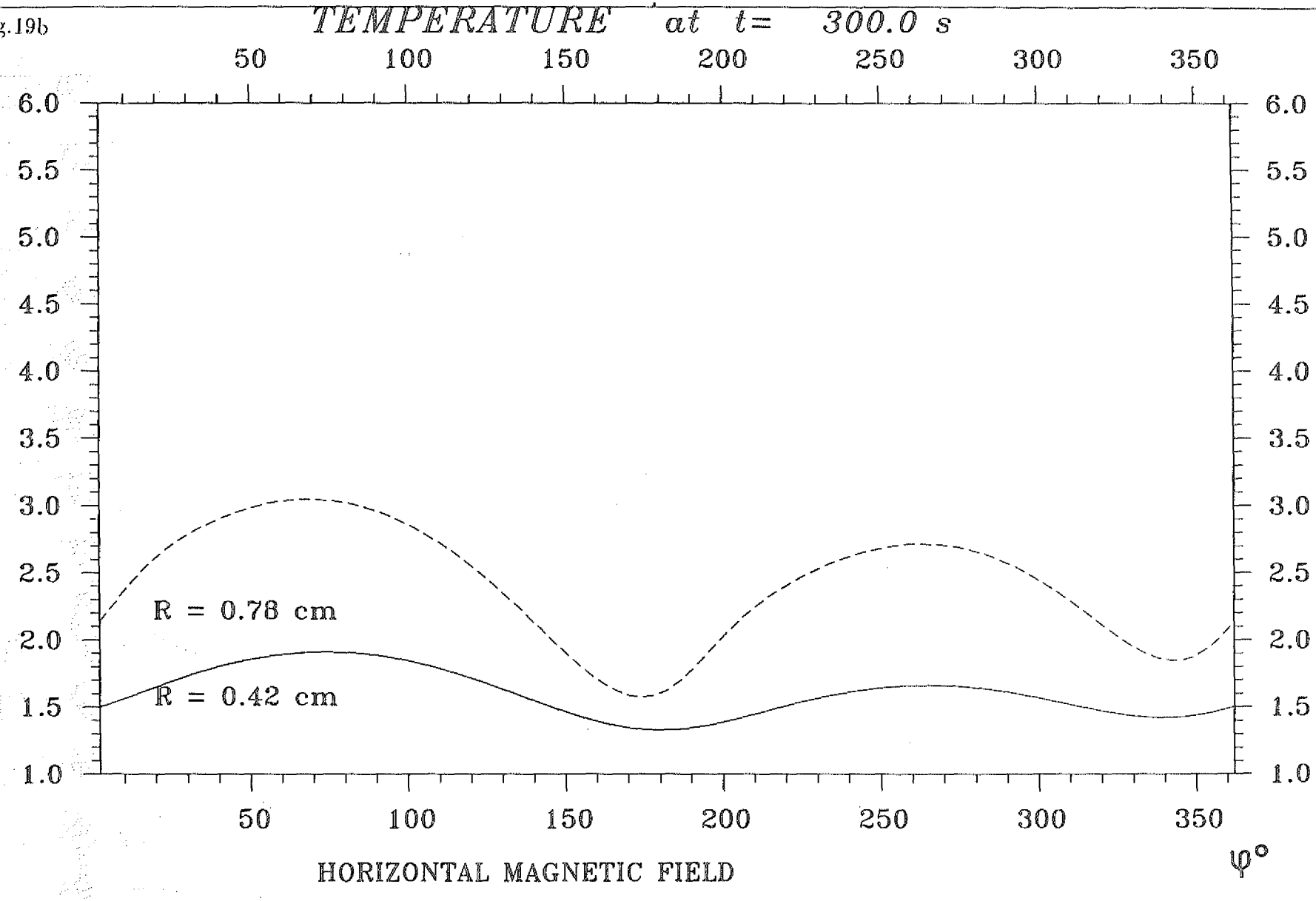
TEMPERATURE at t= 300.0 s
50
100
150
200
250
300
350
6.0
5.5
5.0
4.5
4.0
3.5
3.0
2.5
2.0
1.5
1.0
R = 0.78 cm
R = 0.42 cm
HORIZONTAL MAGNETIC FIELD
φ°

Fig.19c

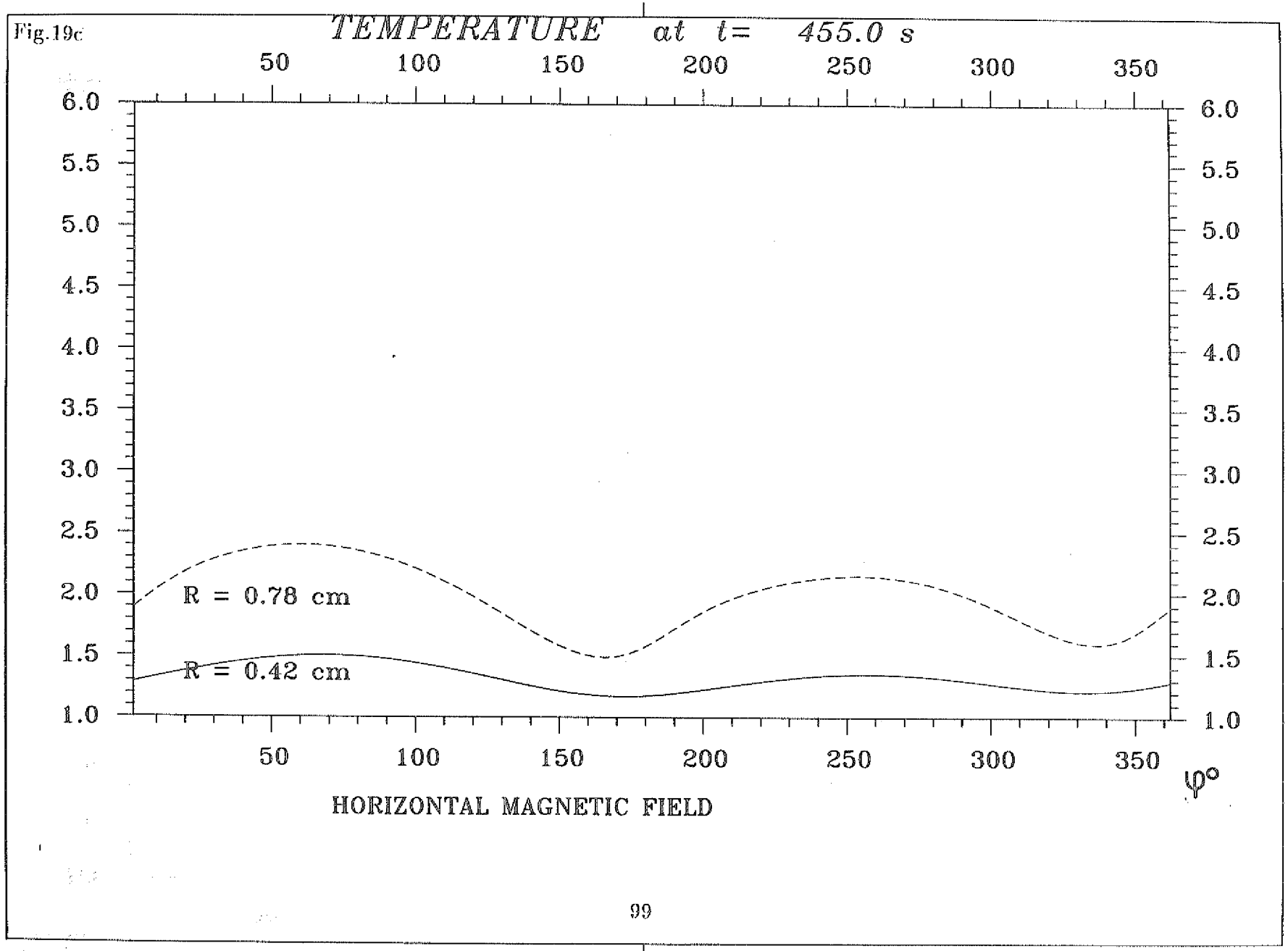
TEMPERATURE at t= 455.0 s
50
100
150
200
250
300
350
6.0
5.5
5.0
4.5
4.0
3.5
3.0
2.5
2.0
1.5
1.0
R = 0.78 cm
R = 0.42 cm
φ°
HORIZONTAL MAGNETIC FIELD

Fig. 19d

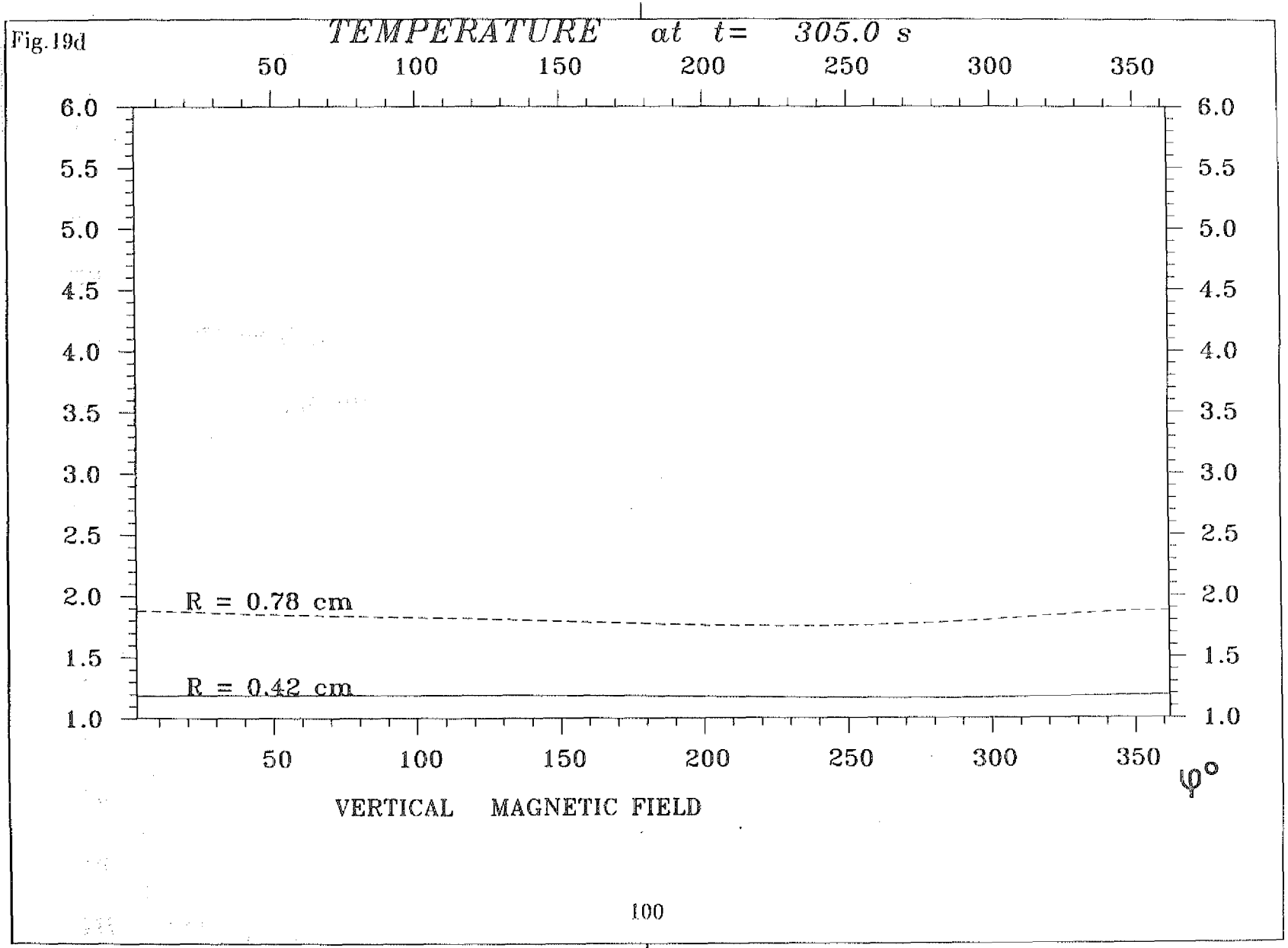
TEMPERATURE at t= 305.0 s
50
100
150
200
250
300
350
6.0
5.5
5.0
4.5
4.0
3.5
3.0
2.5
2.0
1.5
1.0
R = 0.78 cm
R = 0.42 cm
φ°
VERTICAL MAGNETIC FIELD

Fig.19c

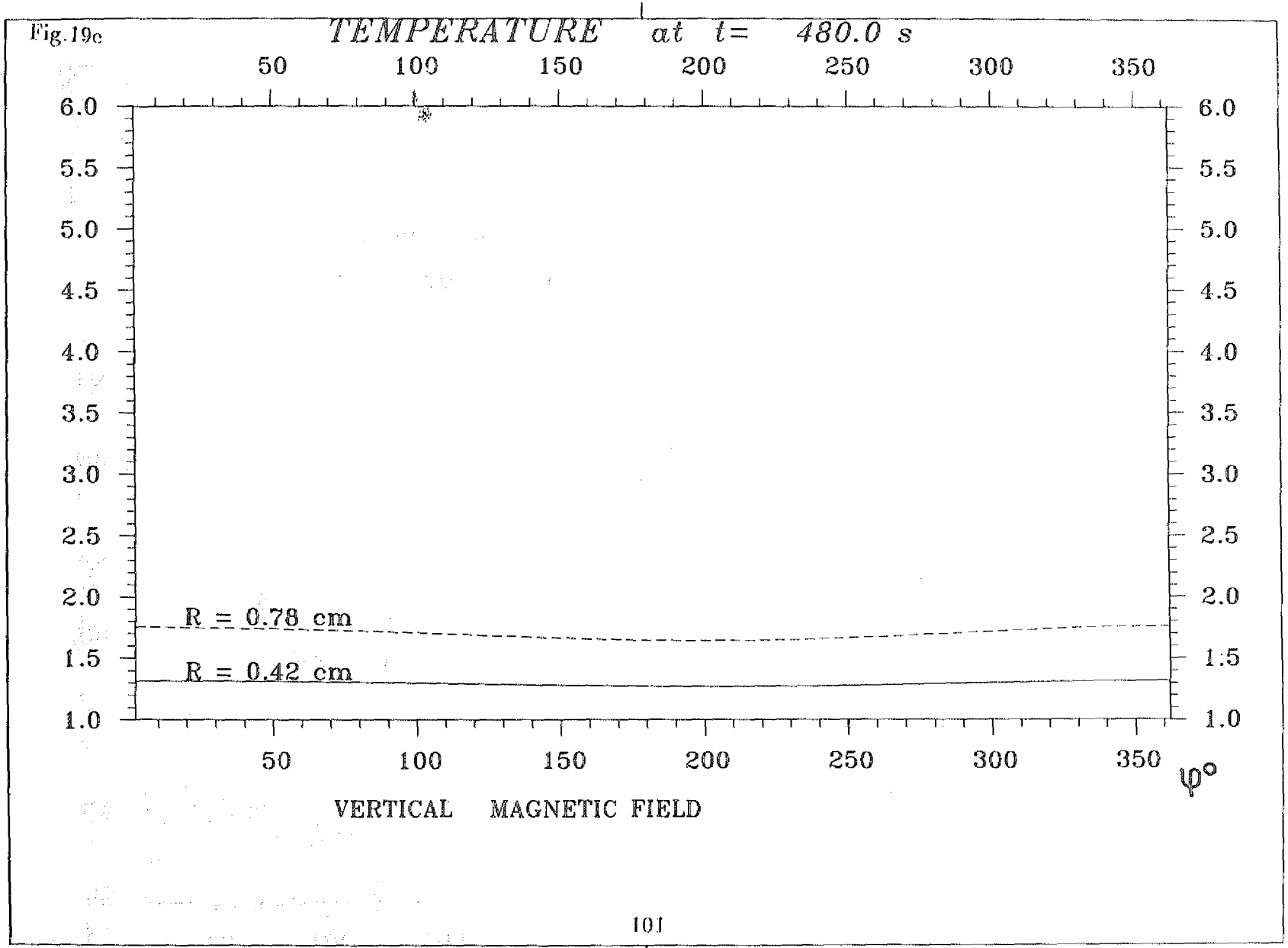
TEMPERATURE at t= 480.0 s
50
100
150
200
250
300
350
6.0
5.5
5.0
4.5
4.0
3.5
3.0
2.5
2.0
1.5
1.0
R = 0.78 cm
R = 0.42 cm
φ°
VERTICAL MAGNETIC FIELD

Fig.20a

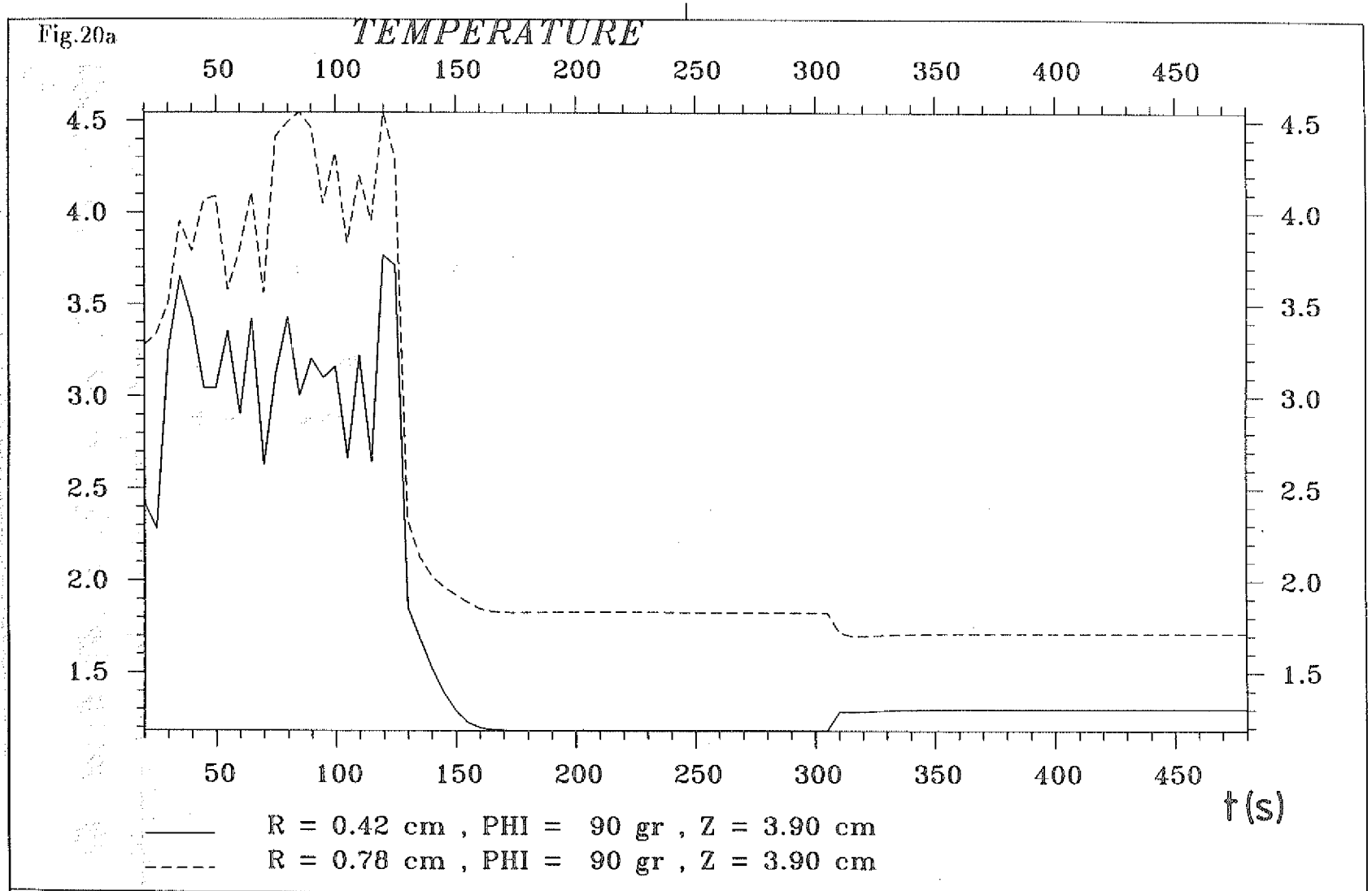
TEMPERATURE
50
100
150
200
250
300
350
400
450
4.5
4.0
3.5
3.0
2.5
2.0
1.5
t (s)
R = 0.42 cm , PHI = 90 gr , Z = 3.90 cm
R = 0.78 cm , PHI = 90 gr , Z = 3.90 cm

Fig.20b

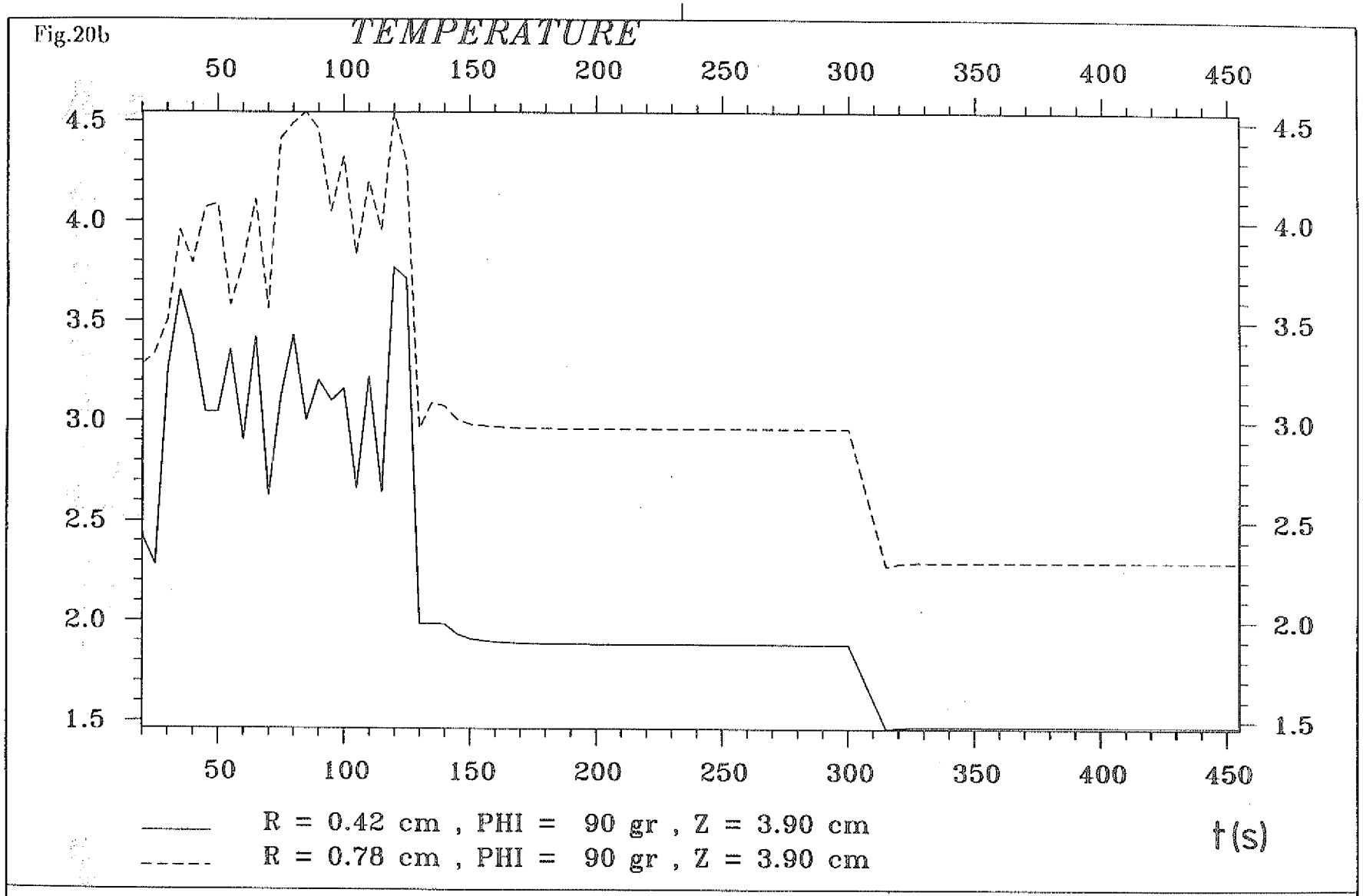
TEMPERATURE
50
100
150
200
250
300
350
400
450
4.5
4.0
3.5
3.0
2.5
2.0
1.5
R = 0.42 cm , PHI = 90 gr , Z = 3.90 cm
R = 0.78 cm , PHI = 90 gr , Z = 3.90 cm
t(s)

Fig.21a

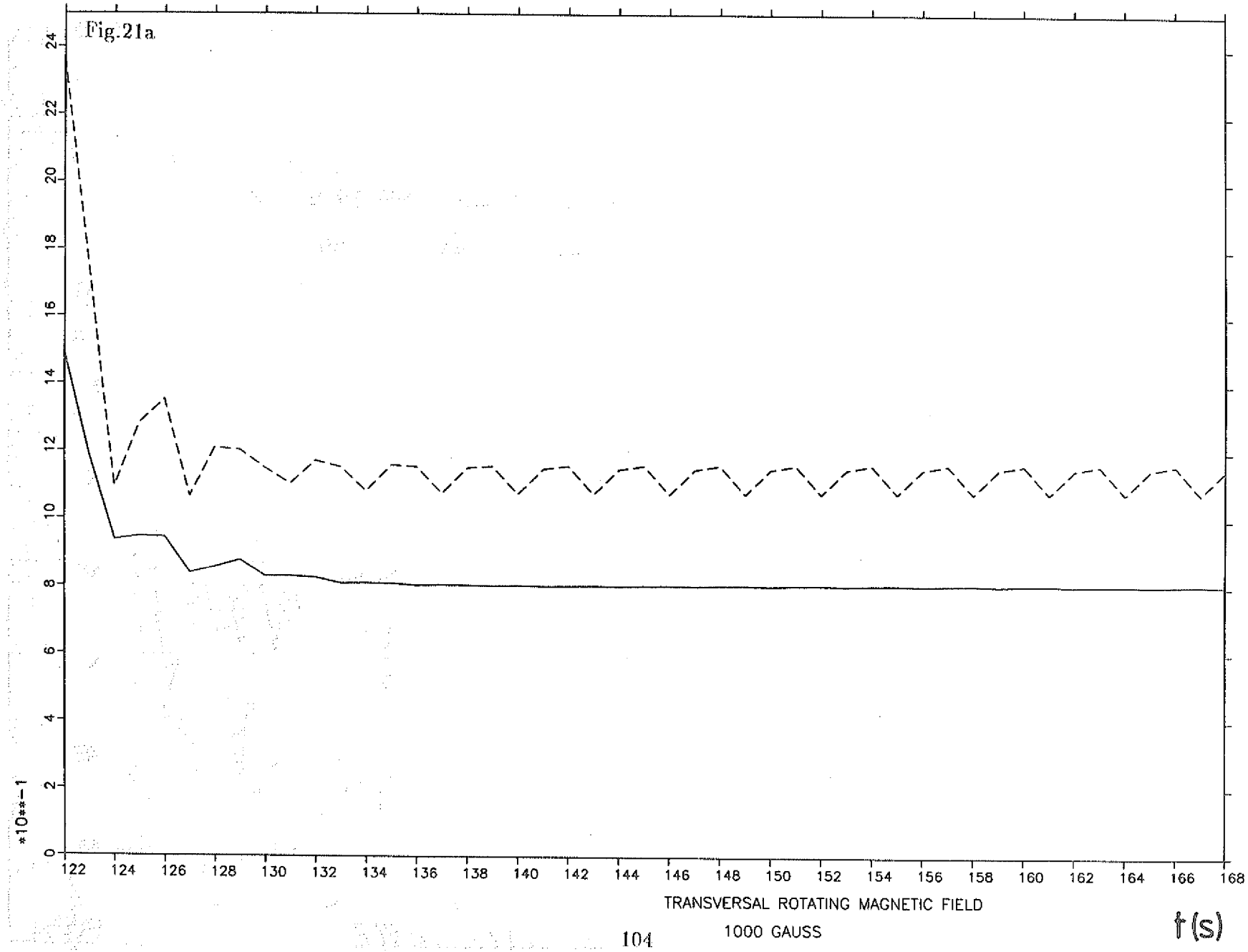
*10**-1
0
2
4
6
8
10
12
14
16
18
20
22
24
122
124
126
128
130
132
134
136
138
140
142
144
146
148
150
152
154
156
158
160
162
164
166
168
TRANSVERSAL ROTATING MAGNETIC FIELD
1000 GAUSS
f (s)

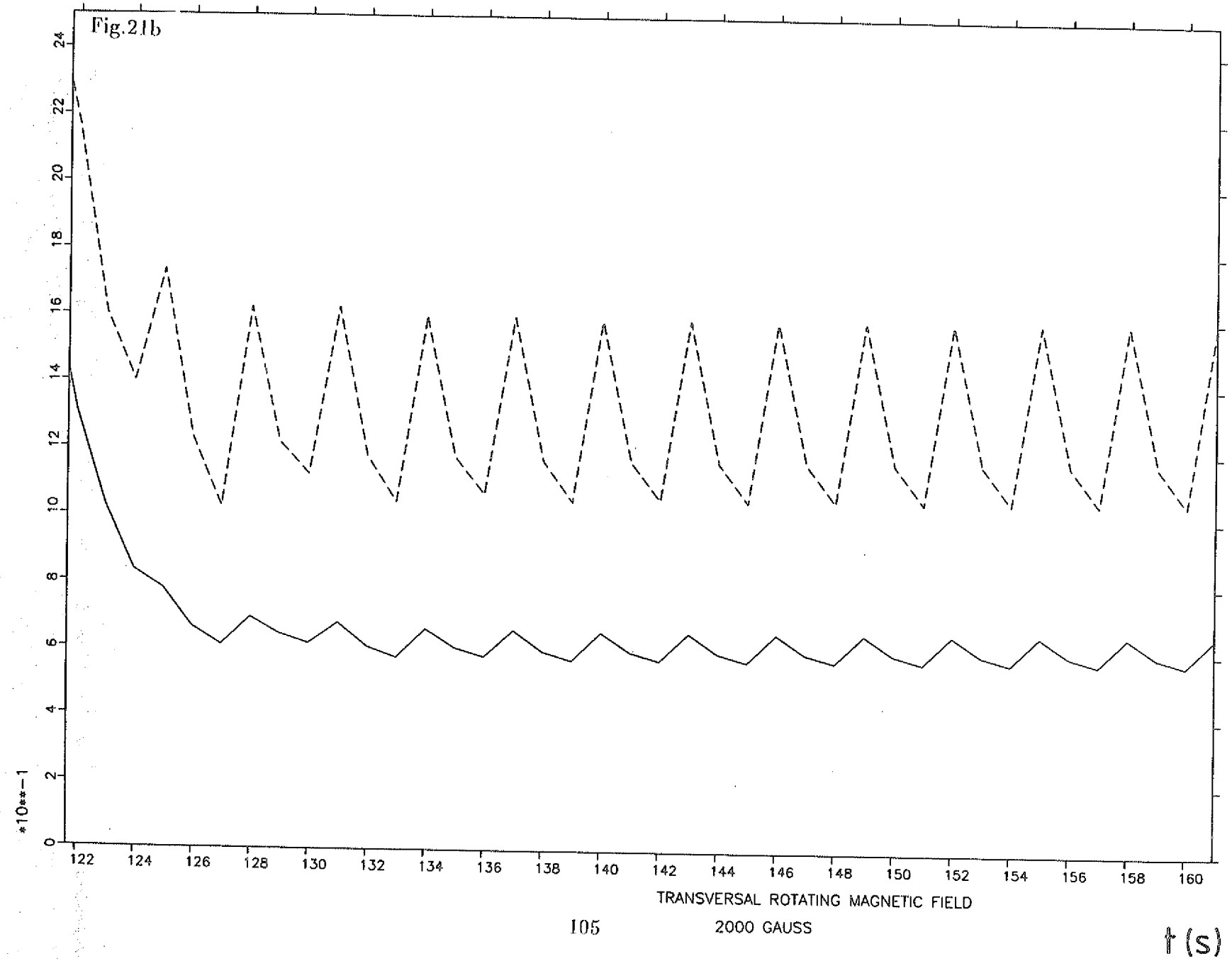
Fig.21b
*10**-1
0
2
4
6
8
10
12
14
16
18
20
22
24
122
124
126
128
130
132
134
136
138
140
142
144
146
148
150
152
154
156
158
160
TRANSVERSAL ROTATING MAGNETIC FIELD
2000 GAUSS
t (s)

FORSCHUNGSZENTRUM JÜLICH GmbH

KFA

Jül-2697
Decembre 1992
ISSN 0366-0885